



**HAL**  
open science

# Mechanical control on fluid-induced aseismic slip: insights from injection experiment modeling

Jinlin Jiang

► **To cite this version:**

Jinlin Jiang. Mechanical control on fluid-induced aseismic slip : insights from injection experiment modeling. Environmental Engineering. Université Paris sciences et lettres, 2023. English. NNT : 2023UPSLM056 . tel-04546788

**HAL Id: tel-04546788**

**<https://pastel.hal.science/tel-04546788>**

Submitted on 15 Apr 2024

**HAL** is a multi-disciplinary open access archive for the deposit and dissemination of scientific research documents, whether they are published or not. The documents may come from teaching and research institutions in France or abroad, or from public or private research centers.

L'archive ouverte pluridisciplinaire **HAL**, est destinée au dépôt et à la diffusion de documents scientifiques de niveau recherche, publiés ou non, émanant des établissements d'enseignement et de recherche français ou étrangers, des laboratoires publics ou privés.



**THÈSE DE DOCTORAT**  
**DE L'UNIVERSITÉ PSL**

Préparée à Mines Paris - PSL

**Mécanique du glissement aiséismique sous pression de fluide : modélisation d'expériences d'injection en laboratoire.**

**Mechanical control on fluid-induced aseismic slip: insights from injection experiment modeling.**

Soutenue par

**Jinlin JIANG**

Le 10 Avril 2023

Dirigée par

**Pierre DUBLANCHET**

**Dominique BRUEL**

École doctorale n° 398

**Géosciences, ressources  
naturelles et environnement**

Spécialité

**Géoscience et géoingénierie**

**Composition du jury :**

Mr. Alexandre SCHUBNEL Directeur de recherche, ENS, PSL/CNRS	<i>Président</i>
Mr. Robert C. VIESCA Associate professor, Tufts University	<i>Rapporteur</i>
Mme. Marie VIOLAY Associate professor, EPFL	<i>Rapporteur</i>
Mme. Mathilde ADELINET Maître de conférences, HDR, IFPEN	<i>Examineur</i>
Mr. Jean SCHMITTBUHL Directeur de recherche, EOST/CNRS	<i>Examineur</i>
Mr. Pierre DUBLANCHET Chargé de recherche, HDR, MINES	<i>Directeur de thèse</i>
Mr. Dominique BRUEL Maître de recherche, MINES	<i>Examineur</i>



**Thèse de doctorat de l'université PSL  
préparée à MINES ParisTech**

**Mécanique du glissement  
asismique sous pression de  
fluide: modélisation  
d'expériences d'injection en  
laboratoire**

Jinlin JIANG

13 06 2023

École doctorale n°398  
Géosciences, ressources naturelles et environnement

Spécialité  
Géosciences et géoingénierie



# Résumé

La géothermie profonde pourrait être amenée à jouer un rôle important dans le développement des énergies renouvelables. Cependant, les expérimentations récentes ont montré que cette technique d'exploitation peut également déstabiliser des failles par pressurisation de fluide, et déclencher des séismes à l'origine de dommages importants aux infrastructures. Ce processus implique généralement des glissement lents, dits asismiques car non radiatifs, sur les failles. Afin de pouvoir développer une exploitation sûre et efficace de l'énergie géothermique, il est donc indispensable de mieux comprendre les mécanismes liés à la réactivation de faille par des fluides. Cette thèse de doctorat est une étude numérique dont l'objectif est de modéliser des expériences d'injection de fluide en laboratoire déclenchant des fronts de glissement asismique. Ces expériences ont été menées dans un échantillon de roche chargé en presse tri-axiale.

Le système expérimental est modélisé en 3D en utilisant une approche éléments finis (FEM), permettant de prendre en compte la géométrie réelle de l'échantillon, du contact (fracture) et les contraintes expérimentales appliquées. Le contact est contrôlé par une loi de frottement affaiblissante. Afin de simuler l'effet d'une injection de fluide dans la fracture, ce modèle est couplé à un modèle de diffusion. Le modèle numérique couplé est dans un premier temps comparé à une solution théorique permettant d'établir la résolution nécessaire à mettre en oeuvre. Puis le modèle est calibré sur un jeu de données expérimentales, permettant de mettre en lumière l'importance de la rigidité effective du système expérimental dans la réactivation du glissement. Ces premières étapes de validation sont suivies par une étude paramétrique visant à quantifier le rôle des propriétés hydromécanique, des propriétés de frottement, de l'état de contrainte initial, et du scénario d'injection sur la dynamique du glissement sismique. Les résultats obtenus indiquent que l'état de contrainte initial sur la faille joue un rôle prépondérant sur la vitesse de propagation du front de glissement asismique et sur le glissement maximal observé. Un état

de contrainte proche du seuil de rupture favorise des propagations rapides et un glissement important. Dans une moindre mesure, la vitesse d'injection, la diffusivité hydraulique et le niveau de frottement résiduel influencent également la vitesse de propagation du front de glissement asismique et l'amplitude du glissement final, en accord avec les prédictions de la mécanique de la fracturation élastique linéaire. Enfin, les résultats obtenus au cours de cette exploration paramétrique indiquent que le glissement maximal obtenu varie comme la racine carrée du volume injecté, fournissant un nouvel éclairage sur les lois d'échelle empiriques reliant moment asismique et volume de fluide injecté. Le travail présenté dans cette thèse a permis en outre de développer et de tester des outils de modélisation d'expériences en presse triaxiale, ouvrant la voie à de nouvelles perspectives d'interprétation de ces expériences.

**Mots clés:** Injection de fluide, Glissement asismique, Vitesse de rupture, Moment asismique, Volume injecté, Presse tri-axiale, Frottement, État de contrainte

# Abstract

The extraction of deep geothermal heat is an important source of renewable energy. However, it can also induce reactivation of slip on preexisting crustal faults, which can lead to seismic events and damage to infrastructure. A possible conceptual model for the triggering of induced earthquakes assumes that fluid injection induces propagating slow aseismic slip that in turn redistributes stresses causing asperities to fail as earthquakes. Therefore, understanding the mechanics of fluid-induced aseismic slip is crucial for the safe and efficient extraction of geothermal energy. This Ph.D. thesis presents a numerical modeling study of fluid-induced fault slip reactivation and rupture propagation.

A 3D FEM model of an injection experiment performed under tri-axial loading conditions at the laboratory centimetric scale is developed. The saw-cut rock sample is represented as a slip-weakening frictional interface embedded in a cylindrical purely elastic medium, loaded by axial and confining stress. The injection is modeled as a pore pressure change within the fault, precomputed with a diffusion solver, and the slip history on the fault is obtained through a FEM approach. We chose an effective stiffness for the simulated rock sample by calibrating our model on a typical injection experiment. Then, we used the model to conduct a parametric study on the mechanic control of fluid-induced aseismic slip.

We study the impact of injection rate, hydraulic diffusivity, stress state and frictional properties on the propagation speed and the maximum magnitude of aseismic slip events generated in our model. We show that the propagation of simulated aseismic slip front is consistent with predictions based on linear elastic fracture mechanics. Considering typical parameter ranges, stress and injection rate have a dominant effect on slip propagation, while frictional properties and fault's diffusivity play a secondary role. Initial stress close to failure and high injection rates both increase slip front speed and reduce the reactivation time of aseismic slip events.

Our simulations also lead to a maximum final slip scaling as the  $\sqrt{\Delta V}$  where  $\Delta V$  is the injected volume, which under an assumption of constant shear drop, leads to a maximum seismic moment scaling as  $\Delta V^{3/2}$ . This latter prediction is consistent with recent mechanical and theoretical studies on the aseismic slip. The original modeling approach presented here could also be used to strengthen the mechanical interpretation of laboratory experiments.

Overall, our study provides insights into the complex behavior of pre-existing fault reactivation induced by fluid injection and quantifies the importance of hydro-mechanical properties and injection scenarios on the dynamics of aseismic slip, suspected to trigger induced earthquakes. The findings of this study can thus inform on the development of strategies to mitigate the risk of induced earthquakes in geothermal energy production and fluid injection practices.

**Keywords:** Aseismic slip, Rupture Speed, Aseismic moment, Injected Volume, Tri-axial Cell, Friction, Stress

# Acknowledgements

I stand humbled on the shoulders of giants, awed by their intellect and generosity, and yet, I am not alone in this journey. I am surrounded by angels, guiding me with their wisdom and love.

To my esteemed supervisors, Prof. Pierre Dublanchet and Prof. Dominique Bruel, I offer my sincere gratitude for being my mentors, challengers, and friends. Your wisdom and experience have shaped me into the scholar I am today, and your support and encouragement have been instrumental in my study.

To the members of my thesis committee, Prof. Alexandre SCHUBNEL, Prof. Robert C. Viesca, Prof. Marie VIOLAY, Prof. Mathilde ADELINET, Prof. Jean SCHMITTBUHL, for their insightful feedback and constructive criticism, which have greatly improved the quality of my work.

To my brilliant colleagues and professors from MINES ParisTech, including Hao, Shuaitao, Christine, Léo, Rita, Milad, Tianyou, Théo, Inès, Ali, Yuke, Gianluca, Antoine, Ramon, Victor, Prof. Hervé Chauris, Prof. Alexandrine Gesret, Prof. Mark Noble, and Ms. Véronique Lachasse, I thank you for sharing your knowledge and insights with me, and for making my study journey more enjoyable and meaningful. Your friendship and camaraderie have been a constant source of joy and inspiration.

To my beloved family, who have been my rock and safe haven, I owe everything. Your love, patience, and understanding have given me the strength and courage to pursue my dreams, even when the road was rough. Your sacrifices and unwavering support have been the foundation of my success, and I will forever cherish your love.

To my dear friends I met in France, Yang Shen, Kang, Vivian, Zimin, Yang Song,

Shun, Tiantian, Dingan, Yuchen, Renjie, Xianchen, and Xingchen who have become my second family and my support system, I express my sincere gratitude. You have shown me the true meaning of friendship, and have made France feel like a second home. Thank you for the countless adventures, late nights, and memories that we have shared.

To my girlfriend, who has been my rock throughout this journey. Your unwavering love and support have kept me going through the toughest of times. Thank you for believing in me, for understanding my passions and dreams, and for standing by my side no matter what. I am grateful to you every day.

Last but not least I would also like to extend my gratitude to Prof. Martin Gális from Comenius University Bratislava for providing the seismic moment and injection volume data, and to Michelle Almakari from Ecole Normale Supérieure de Paris for sharing data and codes for solving the diffusion equation. I appreciate the insightful discussions with Prof. François X. Passelègue from CNRS and the valuable experimental data.

May this work be a tribute to all those who have contributed to my journey and a light to guide those who will embark on theirs.

<b>1</b>	<b>Introduction</b>	<b>1</b>
	Résumé . . . . .	2
	Summary . . . . .	2
1.1	Industrial fluid injection projects and induced seismicity . . . . .	3
1.1.1	Enhanced geothermal system (EGS) . . . . .	3
1.1.2	Waste water disposal . . . . .	6
1.1.3	Oil and gas excavation (Hydraulic fracturing) . . . . .	10
1.1.4	CO2 storage . . . . .	12
1.2	General observations . . . . .	13
1.2.1	Maximum magnitude vs injection volume . . . . .	13
1.2.2	Seismic migration speed . . . . .	15
1.2.3	Aseismic slip . . . . .	21
1.3	Simplified conceptual models of fluid-induced fault slip . . . . .	22
1.3.1	Pore pressure change . . . . .	22
1.3.2	Poro-elasticity . . . . .	24
1.3.3	Aseismic slip . . . . .	25
1.3.4	Fluid injection volume . . . . .	26
1.4	Experimental study of fluid induced fault reactivation . . . . .	26
1.4.1	In-situ experiments . . . . .	26
1.4.2	Laboratorial experiments . . . . .	28
1.5	Numerical modeling of fluid injection-induced fault reactivation . . . . .	28
1.6	Hydraulic fault's properties . . . . .	35
1.7	Objective of the research . . . . .	38
<b>2</b>	<b>Theoretical framework and numerical simulation approach</b>	<b>41</b>
	Résumé . . . . .	42
	Summary . . . . .	42
2.1	Experimental set-up . . . . .	42
2.2	Hydro-mechanical coupling . . . . .	44
2.2.1	Elasticity . . . . .	44
2.2.2	Friction mechanics of rock . . . . .	50
2.2.3	Fluid diffusion and permeability . . . . .	54
2.3	Mechanical problem . . . . .	55
2.3.1	Geometry and element mesh . . . . .	55
2.3.2	Loading progress . . . . .	56
2.3.3	Boundary conditions . . . . .	57
2.4	Solving fluid diffusion equation . . . . .	58
2.4.1	Constant permeability/diffusivity . . . . .	58

2.4.2	Non-constant permeability/diffusivity . . . . .	59
<b>3</b>	<b>Numerical model configuration and calibration</b>	<b>61</b>
	Résumé . . . . .	62
	Summary . . . . .	62
3.1	Theoretical benchmark for numerical/ hydro-mechanical model . . . . .	62
3.1.1	Geometry and model properties . . . . .	62
3.1.2	Loading and boundary conditions . . . . .	63
3.1.3	Numerical results comparison . . . . .	68
3.2	Experimental calibration for numerical/hydro-mechanical model . . . . .	69
3.2.1	Experiment assembling . . . . .	70
3.2.2	Parametric study of material property . . . . .	73
3.2.3	Nucleation length and fault stability . . . . .	76
3.2.4	Result comparison . . . . .	77
3.3	Conclusion . . . . .	78
<b>4</b>	<b>Effect of hydro-mechanical, injection and frictional parameters on the slip reactivation: Simulation and results</b>	<b>81</b>
	Résumé . . . . .	82
	Summary . . . . .	82
4.1	Introduction . . . . .	83
4.2	Numerical model . . . . .	86
4.2.1	Mechanical problem: geometry, loading process and boundary conditions . . . . .	86
4.2.2	Governing equations . . . . .	89
4.3	Effect of hydraulic parameters . . . . .	91
4.4	Effect of stress state . . . . .	99
4.4.1	Initial stress . . . . .	99
4.4.2	Confining stress . . . . .	102
4.5	Effect of frictional parameters . . . . .	104
4.6	Discussion . . . . .	106
4.6.1	Rupture propagation speed . . . . .	107
4.6.2	Maximum slip vs. Injection volume . . . . .	111
4.7	Conclusion . . . . .	117
<b>5</b>	<b>Conclusions and perspectives</b>	<b>119</b>
	Résumé . . . . .	120
	Summary . . . . .	120

5.1	General conclusions . . . . .	120
5.2	Perspectives . . . . .	123
5.2.1	Impact of evolving hydraulic diffusivity . . . . .	123
5.2.2	Advancing Understanding of Induced Seismicity . . . . .	123



# Chapter 1

## Introduction

Résumé . . . . .	2
Summary . . . . .	2
1.1 Industrial fluid injection projects and induced seismicity . . . . .	3
1.1.1 Enhanced geothermal system (EGS) . . . . .	3
1.1.2 Waste water disposal . . . . .	6
1.1.3 Oil and gas excavation (Hydraulic fracturing) . . . . .	10
1.1.4 CO2 storage . . . . .	12
1.2 General observations . . . . .	13
1.2.1 Maximum magnitude vs injection volume . . . . .	13
1.2.2 Seismic migration speed . . . . .	15
1.2.3 Aseismic slip . . . . .	21
1.3 Simplified conceptual models of fluid-induced fault slip . . . . .	22
1.3.1 Pore pressure change . . . . .	22
1.3.2 Poro-elasticity . . . . .	24
1.3.3 Aseismic slip . . . . .	25
1.3.4 Fluid injection volume . . . . .	26
1.4 Experimental study of fluid induced fault reactivation . . . . .	26
1.4.1 In-situ experiments . . . . .	26
1.4.2 Laboratorial experiments . . . . .	28
1.5 Numerical modeling of fluid injection-induced fault reactivation . . . . .	28
1.6 Hydraulic fault's properties . . . . .	35
1.7 Objective of the research . . . . .	38

## Résumé

L'introduction fournit un aperçu complet des recherches menées sur les projets d'injection de fluides industriels et leur impact sur la sismicité induite. Ce chapitre explore divers projets spécifiques, tels que les systèmes géothermiques améliorés, l'élimination des eaux usées, la fracturation hydraulique dans le contexte de l'extraction pétrolière et gazière, ainsi que le stockage du CO<sub>2</sub>. Des observations clés sont présentées, englobant la relation entre l'amplitude maximale et le volume d'injection, la vitesse de migration sismique et l'occurrence du glissement asismique.

De plus, le chapitre introduit des modèles conceptuels simplifiés qui éclairent les mécanismes sous-jacents au glissement de failles induit par les fluides. Ces modèles se concentrent sur des facteurs importants tels que les changements de pression interstitielle, la poro-élasticité, les phénomènes de glissement asismique et l'influence du volume d'injection de fluide. La discussion souligne l'importance des études expérimentales, mettant en évidence à la fois les expériences in situ et en laboratoire, pour acquérir une compréhension approfondie de la réactivation de failles induite par l'injection de fluides.

De plus, le chapitre souligne l'importance de la modélisation numérique en tant qu'outil précieux pour comprendre les dynamiques complexes impliquées dans les événements sismiques induits par l'injection de fluides. En utilisant des simulations numériques, les chercheurs peuvent efficacement étudier le comportement des failles hydrauliques et acquérir des connaissances sur leurs propriétés.

Dans l'ensemble, ce chapitre introductif fournit une base solide pour le projet de recherche en décrivant le contexte, en mettant en évidence des observations critiques et en soulignant l'utilisation d'approches expérimentales et numériques pour parvenir à une compréhension complète de la réactivation de failles induite par l'injection de fluides.

## Summary

The introduction provides a comprehensive overview of the research conducted on industrial fluid injection projects and their impact on induced seismicity. This chapter explores a range of specific projects, including enhanced geothermal systems, wastewater disposal, hydraulic fracturing in the context of oil and gas extraction, and the storage of CO<sub>2</sub>. Key observations are presented, encompassing the relationship between maximum magnitude and injection volume, seismic migration speed, and the occurrence of aseismic slip.

Moreover, the chapter introduces simplified conceptual models that elucidate the mechanisms underlying fluid-induced fault slip. These models focus on significant factors such as pore pressure changes, poro-elasticity, aseismic slip phenomena, and the influence of fluid injection volume. The discussion emphasizes the importance of experimental studies, highlighting both in-situ and laboratory experiments, in gaining a deeper understanding of fluid injection-induced fault reactivation.

Additionally, the chapter underscores the significance of numerical modeling as a valuable tool for comprehending the complex dynamics involved in fluid injection-induced seismic events. By utilizing numerical simulations, researchers can effectively investigate the behavior of hydraulic faults and gain insights into their properties.

Overall, this introductory chapter provides a solid foundation for the research project by outlining the context, highlighting critical observations, and emphasizing the utilization of experimental and numerical approaches to achieve a comprehensive understanding of fluid injection-induced fault reactivation.

## **1.1 Industrial fluid injection projects and induced seismicity**

In this section, we will examine several industrial contexts where fluid injection plays a crucial role, and where induced seismicity has either been observed or is anticipated to occur.

### **1.1.1 Enhanced geothermal system (EGS)**

Geothermal energy is clean low-emission energy with a high capacity factor, which is over 90% in some cases (Li *et al.*, 2015). By 2020, a total of 88 countries developed the use of thermal energy. The thermal energy consumption was 1,020,877 TJ/yr (283,580 GWh/yr), cutting down 78.1 million tonnes of carbon and 252.6 million tonnes of CO<sub>2</sub> greenhouse gas emissions (Lund and Toth, 2021). Enhanced geothermal systems (EGS) are different from traditional geothermal systems on the basis of the type of exploitation. In comparison with the conventional geothermal power systems, which have been developed over 100 years, the distinguishing features of EGS are taking advantage of a pre-existent system of cracks, improving the natural properties of this system by different processes and circulating fluid in the Hot Dry Rock (HDR). A number of important EGS sites are distributed all over the world in South Korea (Lee *et al.*, 2011), the United States (Pan *et al.*, 2019), the EU (Blöcher

*et al.*, 2018; Schellschmidt *et al.*, 2010; Wallroth *et al.*, 1999; Wyss and Rybach, 2010; Xie *et al.*, 2020) and Australia (Llanos *et al.*, 2015; Riffault *et al.*, 2018).

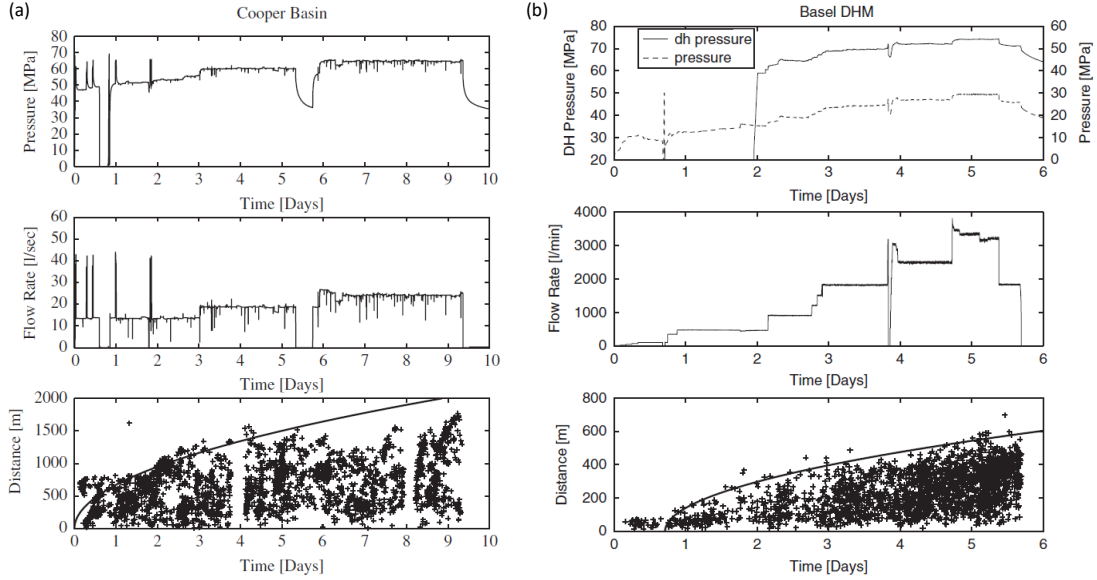


Figure 1.1: Fluid injection induced microseismicity at the geothermal borehole in (a) the Cooper Basin, Australia and (b) Basel, Switzerland. Two upper plots are injection pressure and flow rate with time. The bottom figures are  $r - t$  plots (distance versus time of microseismic events from the beginning of fluid injection) of fluid-injection-induced microseismicity. (Shapiro and Dinske, 2009; Shapiro, 2015)

In the process of EGS power generation, during the reservoir development, thanks to hydraulic treatments, and later during the operation of the reservoir, permeability enhancement and fluid injection have induced seismicity frequently, whose effect has been known over 40 years (Aki *et al.*, 1982) and observed in areas such as Basel and St. Gallen, Switzerland (Deichmann and Giardini, 2009; Diehl *et al.*, 2017; GoertzAllmann *et al.*, 2011; Mukuhira *et al.*, 2017), Soultz-sous-Forêt and Rittershoffen, France (Bourouis and Bernard, 2007; Lengliné *et al.*, 2017) and Pohang, South Korea (Grigoli *et al.*, 2018; Kim *et al.*, 2018). According to the studies (Benioff, 1964; Brace and Byerlee, 1966; Gibowicz, 2009; Lay and Wallace, 1995; Reid, 1910) on the source mechanism of seismicity, the general focal mechanism of the earthquake is a combination of a sudden displacement on a fault plane, a sudden change in shear modulus in the presence of axial strain and a sudden volume change. In this thesis, we mainly talk about the seismicity resulting from energy release caused by instant shearing

movement along a reactivated fault. On the basis of the slip rate of fault reactivation, the slip behavior can be distinguished into seismic events (or earthquakeS) and aseismic slips. When the slip velocity is fast, we call it an earthquake, while slow slip generates aseismic slip, respectively.

The EGS site in Soultz-sous-Forêts, France was developed as a scientific pilot site and is extensively documented (Genter *et al.*, 2010). During an injection experiment in 1993 (Cornet *et al.*, 1997), more than 20000 events were recorded around the injection well, with the largest magnitude of 1.9. Damages with centimetric displacements in the well were observed that did not scale with measured magnitudes. Cornet *et al.* (1997), Calò *et al.* (2011) and Lengliné *et al.* (2017) concluded from these discrepancies that the motion was aseismic. Another observation is common at EGS sites: seismicity is observed to be continued after fluid injection had ceased (Dorbath *et al.*, 2009), as well as the two-year delayed micro-seismicity recorded at Basel, Switzerland (Deichmann and Giardini, 2009; Mukuhira *et al.*, 2017). Figure 1.1 (a) and (b) show two cases of EGS with induced microseismicity in Cooper Basin, Australia and Basel, Switzerland (Shapiro, 2015).

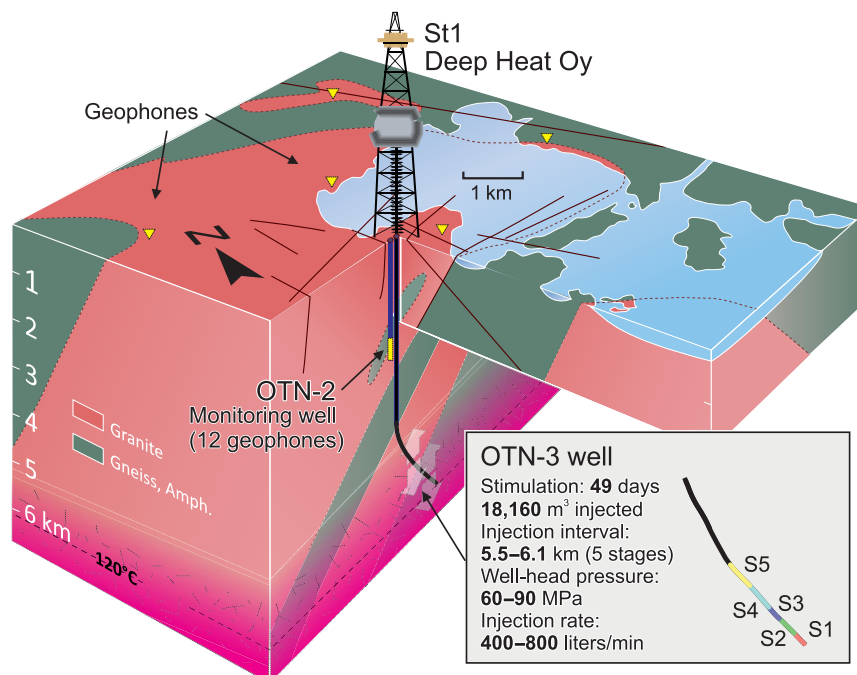


Figure 1.2: Schematic view of the world's deepest EGS project site, Helsinki, Finland. (Kwiatek *et al.*, 2019).

The world's deepest (6.4 km in depth, shown in Fig. 1.2) EGS project site was constructed near Helsinki, Finland. The stimulation and monitoring of seismicity was conducted by Kwiatek *et al.* (2019) through the usage of a traffic light system (TLS) and controlling the injection volumes and pressures. 43,883 microseismic events were observed, whose magnitude ranged between -0.6 and 2. Their approach found that the seismicity was dependent on the injection parameters, allowing them to limit the magnitude of induced earthquakes below 2. Such events below this threshold of magnitude are generally not perceptible by the population.

Apart from the micro-seismicity described above, the development stages of EGS systems can also lead to events of higher magnitude. One hundred ninety-five strong events induced by fluid injection into a poorly permeable rock basement in Basel, Switzerland, were recorded by SED (Swiss Seismological Service) from December 2, 2006, to November 30, 2007, whose largest moment magnitude reached  $M_W$  3 (Deichmann and Giardini, 2009). Three events with a magnitude over 3 occurred 1-2 months after bleed-off (Mukuhira *et al.*, 2017; Mukuhira *et al.*, 2008). Seismicity was observed outside the edge of the stimulated area during the shut-in period, with the largest events occurring. The Basel project was eventually canceled because it was rejected by the public in an urbanized setting, with some damage to buildings (Deichmann *et al.*, 2014; Häring *et al.*, 2008). Another important project to be recalled here that failed was in Pohang, South Korea. A high-magnitude earthquake was induced on an unanticipated deep fault whose moment magnitude ( $M_w$ ) of 5.5 was one of the largest and most destructive earthquakes in Korea since last century.

Early in the 1960s, Geysers in California started to provide geothermal power in the U.S. (Kagel *et al.*, 2005), which keeps continuing successfully today. It is at the same time the most prominent geothermal electric power generation plant in the world and one of the most tectonically active regions in California (Majer and Peterson, 2007). To maintain the balance of steam pressure in the Geysers system, wastewater or local rain and stream water are injected into it, with the regular occurrence of events with a magnitude above 3. The irruption of earthquakes was associated with the increase of fluid injection in the project. Majer and Peterson (2007) also revealed that seismicity near Geysers might be enhanced or reduced independently or together by different sets of processes, such as injecting or extracting fluid in the reservoir.

### 1.1.2 Waste water disposal

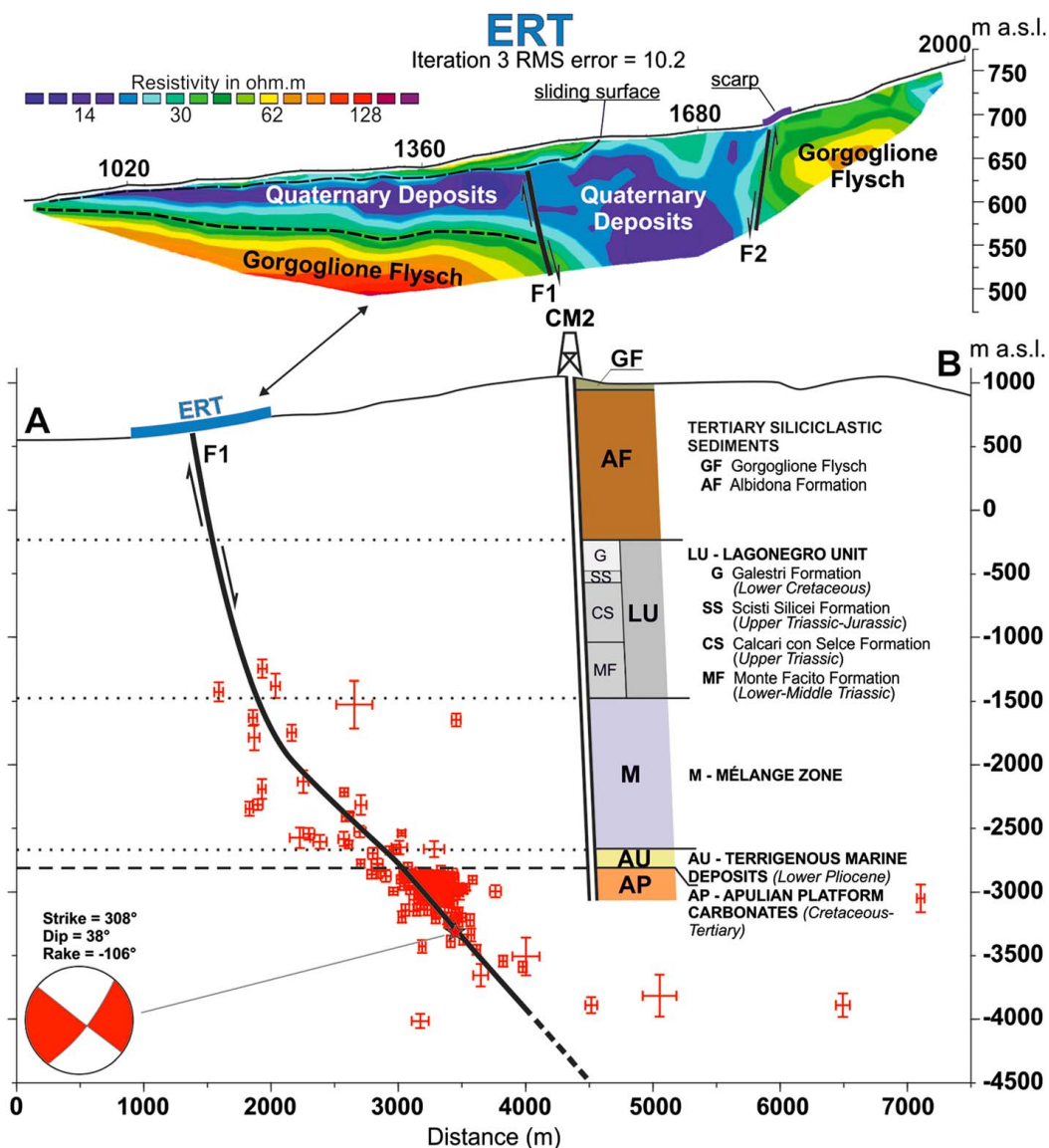


Figure 1.3: Cross-section of the microseismicity area in the High Agri Valley in southern Italy, showing the NE dipping normal fault (F1) revealed from the high-resolution relocation, the focal mechanism for the largest microseismic event ( $M_l=2.0$ ), CM2 injection well stratigraphic log (bottom figure) and electrical resistivity tomography (ERT, top figure). M a.s.l. in Y axis is meters of vertical distance above sea level. (Stabile *et al.*, 2014).

Since this century, the application of shale gas exploitation technology using

the hydraulic fracturing method has dramatically increased the production of oil and gas resources in the United States and changed the world energy market. The hydraulic fracturing method brings out millions of liters of wastewater, which is an enormous problem to deal with (Estrada and Bhamidimarri, 2016). The most widely accepted measures to dispose wastewater are deep-well injection and re-injecting for recycling. These wastewater disposal methods are related to the generation of seismic events around the injection well (Ellsworth, 2013). As far as inducing seismicity is concerned, injecting wastewater is riskier than hydraulic fracturing itself (Ellsworth, 2013). In some cases, it was observed that earthquakes continued, and the largest occurred after wastewater injection stopped (Horton, 2012; Kim, 2013; Nicholson *et al.*, 1988; Seeber *et al.*, 2004).

In the wastewater disposal program in the Val d'Agri in Italy, a cluster of 2000 low-magnitude microearthquakes was induced in 2006, whose magnitude ranged between -0.2 and 2.7 (Valoroso *et al.*, 2009). The microseismicity occurred to the south side of the basin, whose area was about 5 km wide and from 1 to 5 km depth. The relevance of the microseismic events and the nearby artificial lake Pertusillo's water level change was discovered by Valoroso *et al.* (2009), implying the induced seismicity. Further studies were carried out by Stabile *et al.* (2014) using a high-resolution relocation technique to analyze the space-time evolution of events and focal mechanisms (red cross in Fig. 1.3). An electrical resistivity tomography (ERT, also see in Fig. 1.3) was carried out to verify the fault scarp. Using those methods, a new fault F1 was traced from the surface to 4 km depth under sea level. The NE dipping fault (F1 in Fig. 1.3) was reactivated by the diffusion of pore pressure, which drives stresses to exceed the critical shear stress (Coulomb friction law Equation 1.5 described in session 1.3.1).

Except for the micro-events, large magnitude earthquakes have been triggered by fluid injection in wastewater disposal of the oil industry, such as the  $M_W$  5.7 earthquakes in November 2011 in Oklahoma, United States (Keranen *et al.*, 2013). Three events with  $M_W$  5.0, 5.7 and 5.0 were observed in the North American mid-continent near Prague, Oklahoma, United States (see event A, B and C in Fig. 1.4). Magnitude 5.7 was the largest earthquake ever recorded and was sensed by 17 states. Damage was caused, including 14 destroyed homes, other buildings and human injury. The 1993-2011 injection data of wells 1 and 2 in Fig. 1.4 are shown in Fig. 1.5 including the monthly injection rate, well-head pressure and cumulative volumes (Keranen *et al.*, 2013).

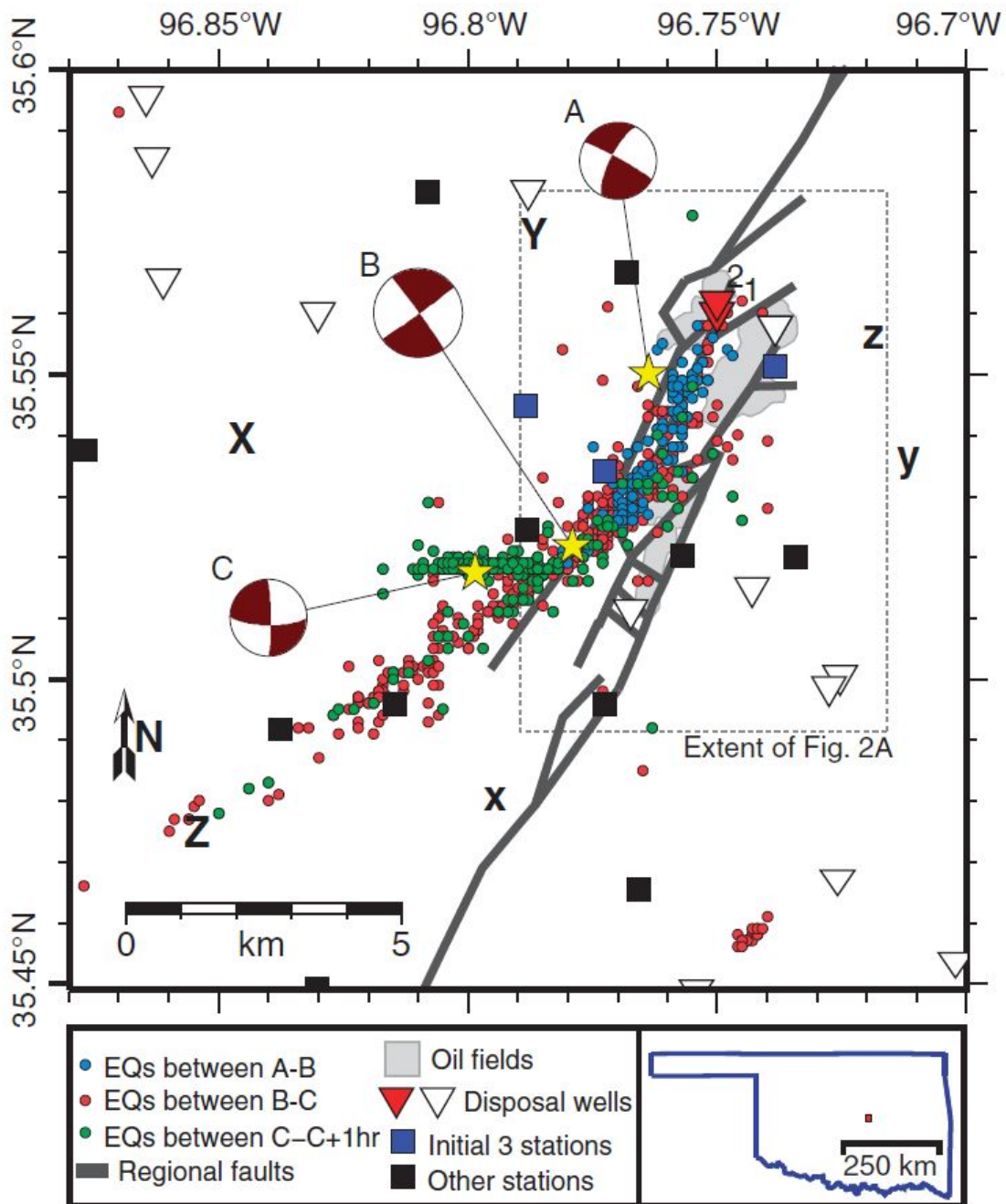


Figure 1.4: Seismicity, centroid moment tensor mechanisms, seismic stations, active disposal wells, and oil fields in central Oklahoma, United States. (Keranen *et al.*, 2013)

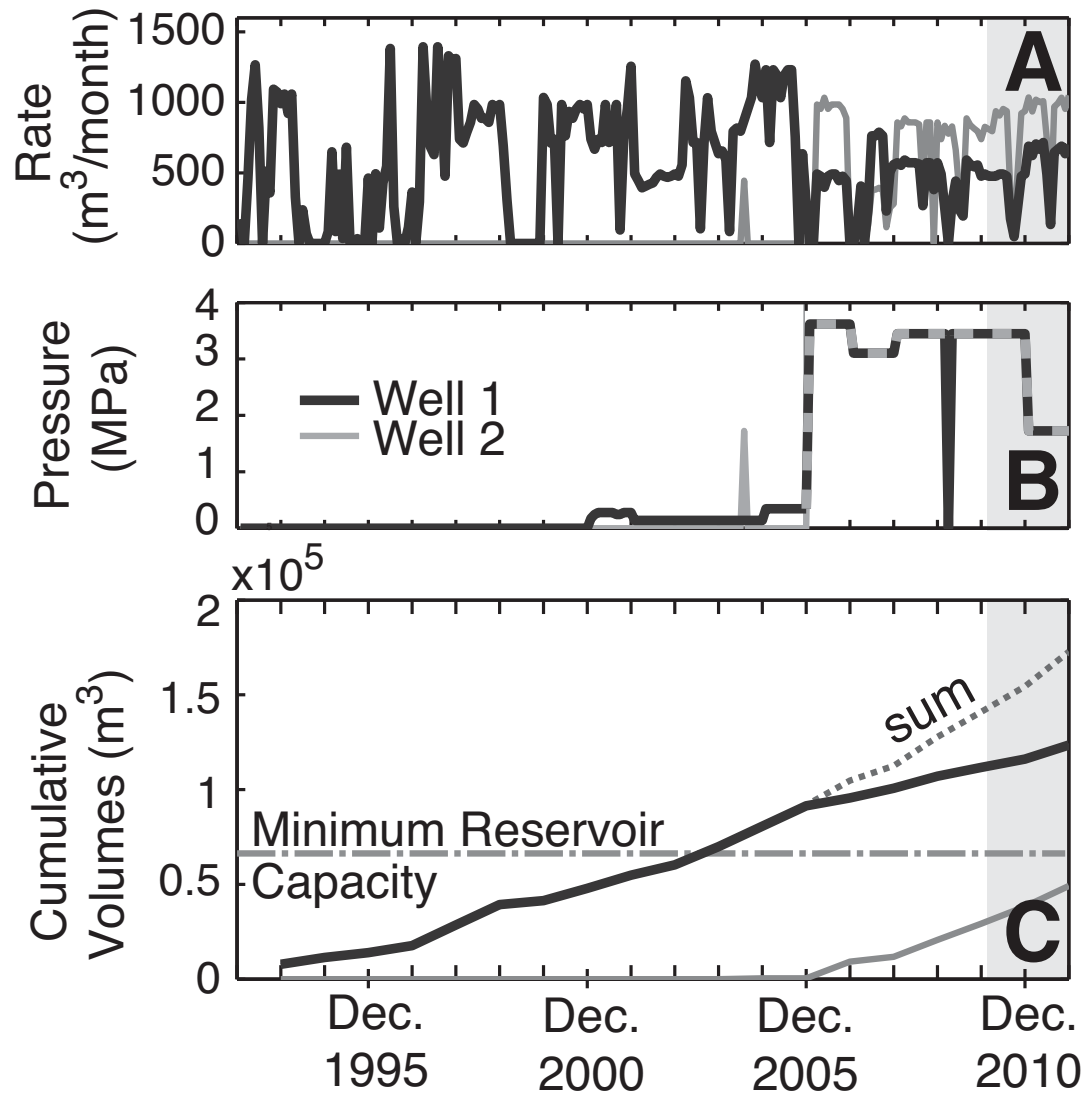


Figure 1.5: Injection data of wastewater disposal at the injection well 1 and 2 in Fig. 1.4 (Keranen *et al.*, 2013)  
 A: Monthly injection volumes. B: Well-head pressure. C: Cumulative injection volume. Fig. 1.4 (Keranen *et al.*, 2013)

### 1.1.3 Oil and gas excavation (Hydraulic fracturing)

Oil and gas production is applied by fluid fracturing to tight shale formations

(Ellsworth, 2013). Controlled fluid injection combined with proppants under pressure creates tensile fractures and increases permeability in rock formations, improving the output of oil and gas reservoirs. Through connecting hydraulic fractures with natural cracks in the reservoirs, the injection method is able to increase the permeability even hundreds of meters away from the injection well, particularly in some fractured zones or natural faults (Maxwell, 2014; Zoback, 2010). Widely in the U.S. and Canada, this fracturing technique along with transporting proppants into fractures are applied in more and more shale formations to extract natural gas and oil since the 1990s, resulting in a boom of energy production in the U.S. (Barati and Liang, 2014).

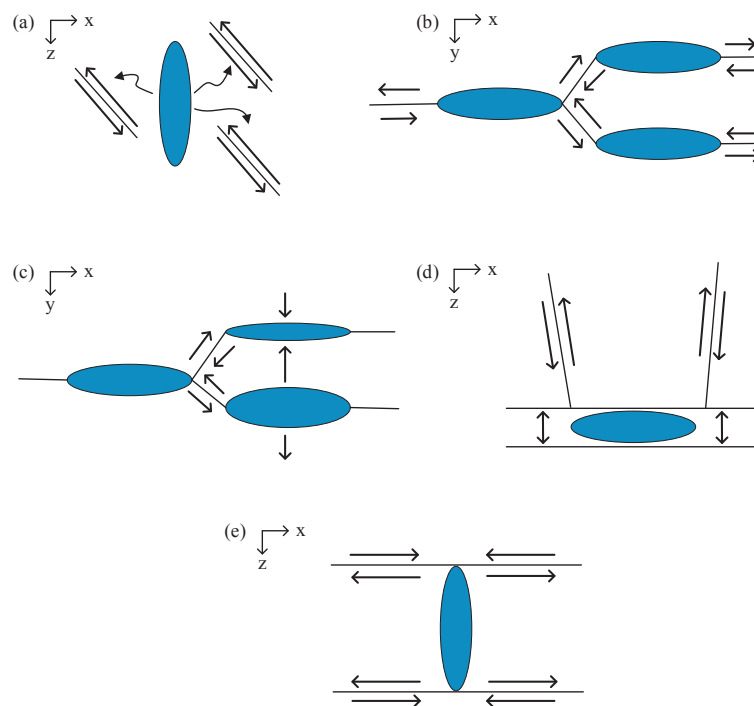


Figure 1.6: Interpretational models to characterize the focal mechanism of hydraulic fracturing induced microseismicity. (a) side view of the fluid diffusion model, the curved arrows represent pore pressure diffusion, (b) the plane view of the fracture loading model, (c) the plane view of the tensile failure model, (d) the side view of the vertical dip-slip model, (e) side view of bedding plane slip model. (Li *et al.*, 2019).

Oil and gas production can also lead to observed forms of earthquake clustering

(Maxwell, 2014). Induced seismicity, accompanying high-pressure fluid injection, are mainly micro-seismic events (moment magnitude  $M_w \leq 3$ ) (Eaton, 2018). Higher-magnitude seismicity happens when pre-existing faults are reactivated (Bao and Eaton, 2016; Clarke *et al.*, 2014), whose moment magnitude is larger than 3. Felt seismicity has been observed increasingly in the U.S. and Canada since this century, linked with wastewater disposal and hydraulic fracturing (Bao and Eaton, 2016; Elst *et al.*, 2013; Keranen *et al.*, 2014; Schultz *et al.*, 2017; Weingarten *et al.*, 2015). As a result, monitoring induced seismicity in gas and oil reservoirs is important in the perspective of mitigating the risk and loss caused by induced seismicity (Kao *et al.*, 2016; Kao *et al.*, 2018; Maxwell, 2014; Shapiro, 2008). Different models based on geology and geometry of micro-fractures (see Fig. 1.6) are proposed to interpret the induced seismicity, revealing the interaction between micro-seismicity and hydraulic fracturing (Li *et al.*, 2019), including fluid diffusion (Pearson, 1981; Shapiro *et al.*, 2006b), fracture loading (Rutledge *et al.*, 2004), tensile failure (Baig and Urbancic, 2010; Eaton *et al.*, 2014), vertical dip-slip (Eisner *et al.*, 2010) and bedding plane slip (Rutledge *et al.*, 2013; Staněk and Eisner, 2017).

#### 1.1.4 CO<sub>2</sub> storage

With the increasing industrial production and energy consumption, the emission of greenhouse gas such as carbon dioxide has caused environmental problems like global warming and more frequent extreme climate (MacDowell *et al.*, 2010). Since the late-1800s, the average temperature of the global air has increased 1°C owing to the higher concentrations of CO<sub>2</sub> in the atmosphere (Rohde and Hausfather, 2020). Global warming led to a 1.5 mm/yr increase in global-mean sea level over the twentieth century (Frederikse *et al.*, 2020). A significant method to reduce the carbon content in the atmosphere from power and industrial emission is Carbon Capture and Storage (CCS) (Brinckerhoff *et al.*, 2011). By 2050, CO<sub>2</sub> sequestration is expected to reduce 20% of carbon dioxide emission and to save 70% cost of reaching emission reduction target (DECC, 2012). Different storage strategies, including underground and oceanic geological storage, mineral carbonation, mined-out reservoir, and unmineable coal seams storage, have the advantage of large storage capacity, hundreds of years of long-term storage, low cost, and environmental influence (Aminu *et al.*, 2017; Yamasaki, 2003).

Fluid injection or extraction is implied by Carbon Capture and Storage (CCS) in depleted geological formations, which are likely to affect the pore pressure, permeability, and effective stress on the faults or reservoirs, resulting in fracture or fault

reactivation and leading to induced seismicity (Ellsworth, 2013; Grigoli *et al.*, 2017). In CO<sub>2</sub> injection projects, people have observed induced events (Goertz-Allmann *et al.*, 2017) while fortunately, no perceivable earthquake happened till now (Vilarrasa *et al.*, 2019a; White and Foxall, 2016). Induced micro-seismicity in subsurface reservoirs is commonly observed, such as projects at In Salah, Algeria (Stork *et al.*, 2015; Verdon *et al.*, 2015); Decatur, Illinois, USA (Bauer *et al.*, 2016; Kaven *et al.*, 2015); and Otway, Australia (Myer and Daley, 2011). Several reasons favor the low risk of induced seismicity of CCS projects. On the one hand, the depleted formations for CO<sub>2</sub> storage are generally not critically stressed, making the pressure increase by fluid injection lower than the limit of shear failure stress (Vilarrasa and Carrera, 2015). On the other hand, the easily controlled CO<sub>2</sub> pressure becomes constant and stable after a sharp increase of initial stress (Vilarrasa *et al.*, 2019b).

## 1.2 General observations

In the first section, we introduced industrial projects involved with fluid injection and fluid-injection-induced seismicity. To understand the nucleation of induced seismicity, much attention is paid to the features of induced seismicity. In this section, we aim to expose the main features of induced seismicity, derived from the observations of location and magnitudes, and eventually injected volumes and pressures.

### 1.2.1 Maximum magnitude vs injection volume

The definition of the moment magnitude  $M_w$  is the magnitude scale for ranking earthquakes by size (Bormann, 2002), which was defined by Hanks and Kanamori (1979). The expression of  $M_w$  is given in

$$M_W = \frac{2}{3} \log_{10}(M_0) - 6.06 \quad (1.1)$$

where  $M_0$  is the seismic moment measuring the energy released by the earthquake (Kanamori, 1977). The seismic moment  $M_0$  is computed by the following equation

$$M_0 = GS\delta \quad (1.2)$$

where  $G$  is the shear modulus of the rock medium,  $S$  is the surface of the rupture and  $\delta$  is the average slip.

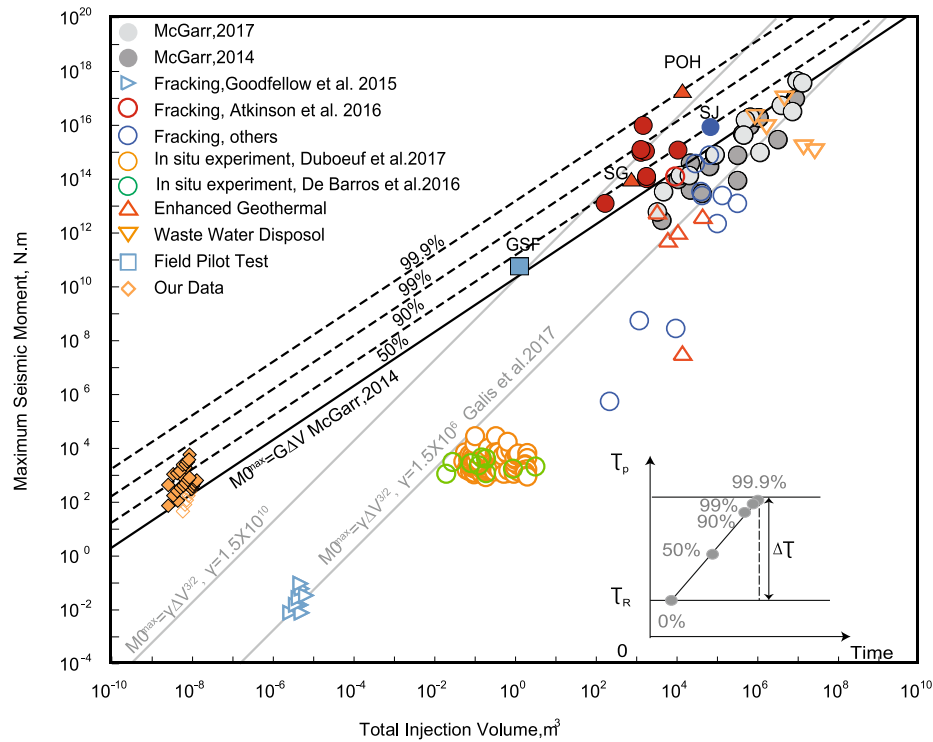


Figure 1.7: The maximum moment of seismic events with injection volume in fluid induced earthquakes (Li *et al.*, 2021). The black line: the upper bound limit of the seismic moment for assumed average stress. The black dashed lines: solution with  $c$  values, as shown in the lower-right inset. Gray solid lines: maximum seismic moment and are added for completeness with two different  $\gamma$  values.

Some induced earthquake sequences show a substantial correlation between maximum magnitudes and total fluid injected volume, such as the Cushing earthquake Mw 5.0 (light grey circles in Fig. 1.7) (McGarr and Barbour, 2017), the Fairview earthquake Mw 5.1 in 2016 (Yeck *et al.*, 2016), the Mw 5.5 Pohang earthquake in 2017 (Grigoli *et al.*, 2018; Westaway and Burnside, 2019), the Prague earthquake Mw 5.7 in 2011 (Keranen *et al.*, 2013) and the Pawnee earthquake Mw 5.8 (Grandin *et al.*, 2017; Yeck *et al.*, 2017). Researches have been done to study the dependence of earthquake maximum magnitudes on the injection volume in order to understand the mechanisms causing the ground motion and to predict the large magnitude of seismicity (McGarr, 1976; McGarr, 2014). The theory was proposed by McGarr (1976) and McGarr (2014) that the maximum seismic moment  $M_0^{max}$  doesn't exceed an upper bound dependent on the injection volume and shear modulus (black line in

Fig. 1.7). Recently, observations on induced seismicity in EGS (Diehl *et al.*, 2017; Kim *et al.*, 2018), hydraulic fracturing (Atkinson *et al.*, 2016) and field pilot experiment (Guglielmi *et al.*, 2015b) show that the seismic magnitudes can be larger than the upper bound  $M_0^{max}$ . The models predicting earthquake magnitude with injection volume will be discussed in session 1.3.4.

## 1.2.2 Seismic migration speed

Earthquake migrations are widely observed during natural and induced swarms (Chen *et al.*, 2012; Shapiro *et al.*, 2006a; Yukutake *et al.*, 2011). Early in 1997, Shapiro *et al.* (1997) concluded that seismic swarms migrate over distances of >1 km during an induced seismicity experiment performed at the bottom of the German Continental Deep Drilling Borehole (KTB) main hole (Fig. 1.8). Later in another one-year (2004-2005) fluid injection experiment in KTB (Fig. 1.9), seismicity was triggered by positive pore pressure perturbation and crustal fluid migration along the fault zones was confirmed that the major fault zones SE2 acted as pathways for the migration of fluids (Shapiro *et al.*, 2006a).

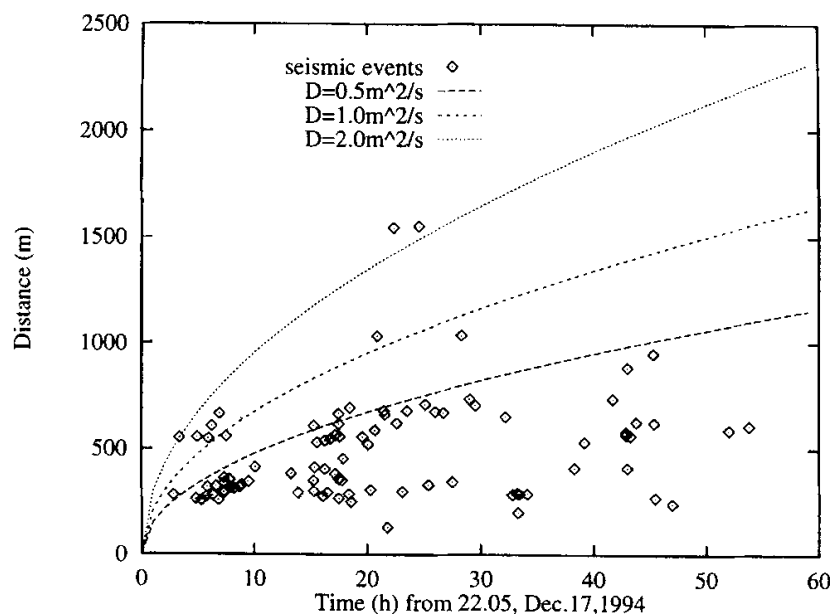
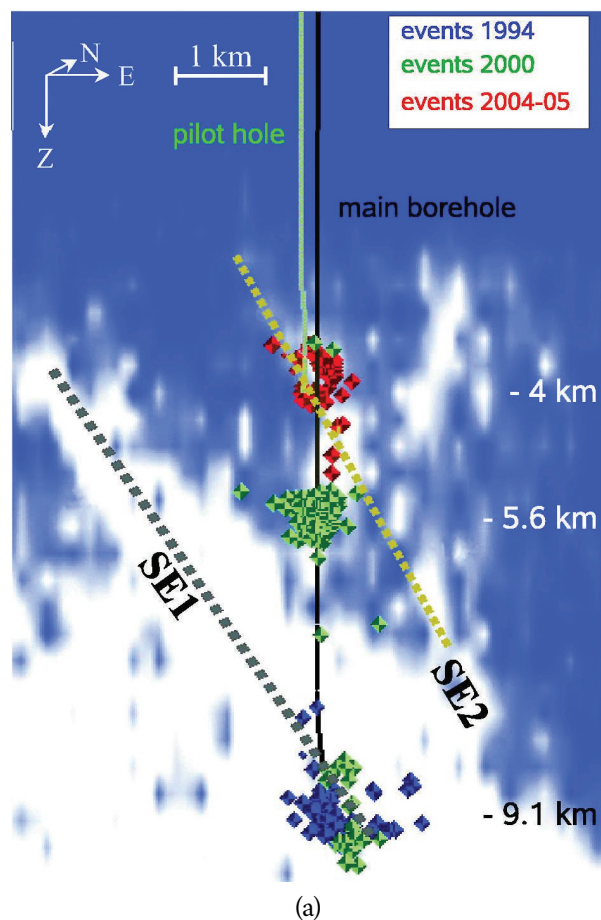
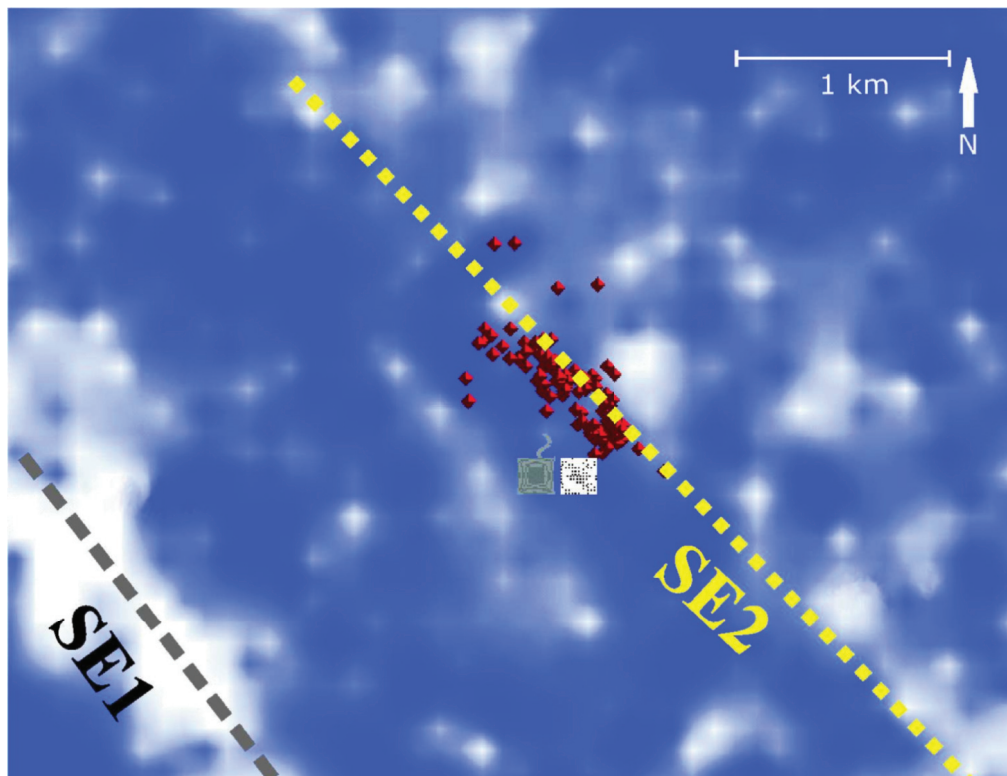


Figure 1.8: Distances of the events from the centre of the injection interval versus their occurrence times in KTB (Shapiro *et al.*, 1997)

Earthquake migration also occurs for natural seismicity. Lohman and McGuire

(2007) and Roland and McGuire (2009) found that on transform faults, migration speeds of earthquake swarms could be higher than that of the fluid diffusion. A similar feather was observed in the 2016  $M_W$  7.0 Kumamoto earthquake. An earthquake migration speed of  $\sim 20$  km/d was observed right after the Mw 6.2 foreshock. Before the 2016 Mw 7.0 Kumamoto earthquake in Japan, a Mw 6.2 foreshock occurred, which expanded towards the center of the main shock and provoked the large magnitude earthquake (Kato *et al.*, 2016). Other observations on the 2004 Mw 6.0 Parkfield earthquake on the San Andreas Fault (Peng and Zhao, 2009), the 2007 Mw 6.7 Noto Hanto earthquake in Japan (Kato and Obara, 2014) and the 2010  $M_L$  6.4 Jiashian earthquake in Taiwan (Tang *et al.*, 2014) revealed that aftershock migrations occurred following the main shock resulting from the propagation of aseismic slip along the active faults.





(b)

Figure 1.9: A vertical (a) and horizontal (b) slice of the depth-migrated 3D image at the KTB site. SE1 and SE2 are two dominant fault systems at 7.2 and 4 km depths. In (a), the seismicity induced by injection experiments of 1994, 2000, and 2004/2005 is shown. Black and green lines are the locations of boreholes. (Shapiro, 2015)

Volcanic regions often have seismic events because of magmatic processes. Observed migration speed of earthquake swarms near the Long Valley caldera in California ranged from 30 m/d to 0.5 km/hr, probably because of different triggering mechanisms (Hill *et al.*, 1990; Hough *et al.*, 2000; Prejean *et al.*, 2003; Vidale and Shearer, 2006).

Near the deep fluid injection well in Youngstown, Ohio, a cluster of 109 small earthquakes ( $M_W$  0.4-3.9) were monitored from Jan 2011 to Feb 2012. Among these detections, 12 of the 109 events whose moment magnitude was larger than  $M_w$  1.8 were recorded and relocated by Kim (2013) as shown in Fig. 1.10 (a). The 12 events were relocated along the ENE-WSW fault region (Fig. 1.10 (a)) and their vertical

location is on two rectangular planes with a length of 1.2 km and a width of 0.5 km (Fig. 1.10 (b)). The migration of these events was between March 2011 to January 2012. Thus, the migration speed of the recorded earthquake swarm was about 4 m/d or about 120 m/month. In another observation, a higher migration speed of 2 40 m/h (48 960 m/d) was detected in the fluid injection test at the Nojima fault zone in Japan (Tadokoro *et al.*, 2000).

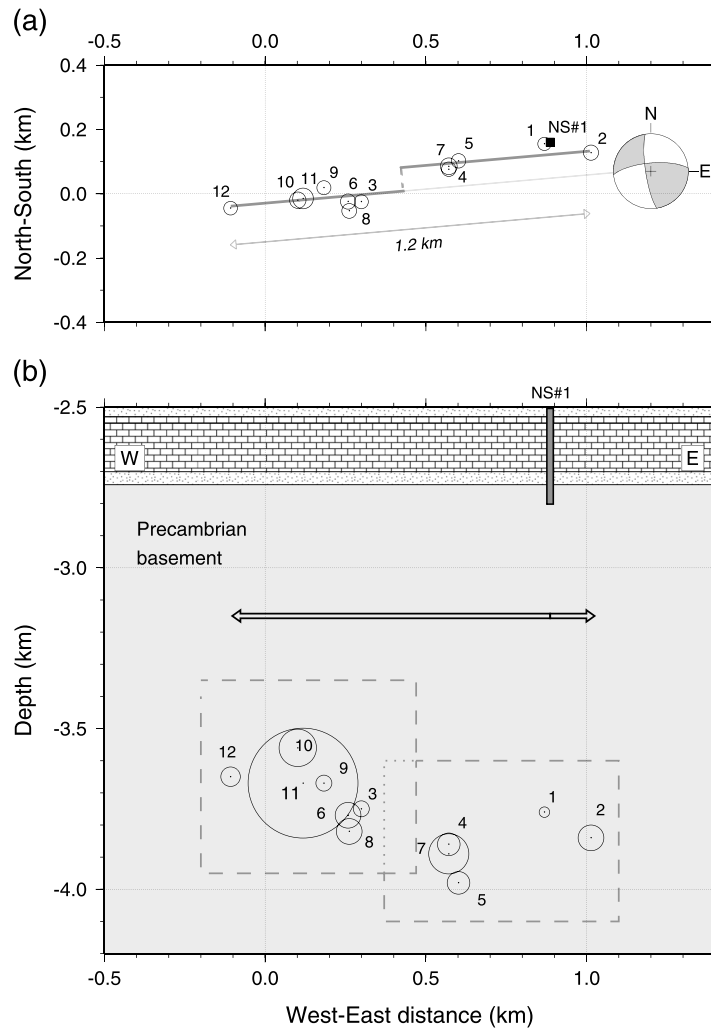


Figure 1.10: Seismic events migration. (a) Relocation of 12 recorded events. (b) Cross-section view of the seismic events. (Kim, 2013).

From Shapiro *et al.* (1997), the spatial and temporal distribution of seismic events

induced by radial fluid diffusion follows the equation

$$r = \sqrt{4\pi Dt} \quad (1.3)$$

where  $r$  is the distance of the slip event front from the injection hole,  $D$  is hydraulic diffusivity and  $t$  is time. If we take the derivation of equation (1.3) with the respect of  $t$ , we can get

$$\frac{dr}{dt} = \sqrt{\frac{\pi D}{t}} \quad (1.4)$$

here  $dr/dt$  is the velocity of the slip front migration. Shapiro *et al.* (1997) interpreted these migration speeds as a fluid diffusion and derived a hydraulic diffusivity from the earthquake migration speed. We show the seismic migration velocity in Table 1.1: the observation leads to very different values of  $D$  and speeds. Typically, the migration velocities of the fluid-driven swarms have the order of m/d. In comparison with the velocity of diffusion-induced migration, a faster velocity in the order of km/hr was observed in the creep-driven swarms in the Salton Trough, California (Lohman and McGuire, 2007). Similarly, such high-speed migration velocities in the order of km/hr were observed on the Imperial fault, California in 1966 (Brune and Allen, 1967) and in 1975 (Johnson and Hadley, 1976).

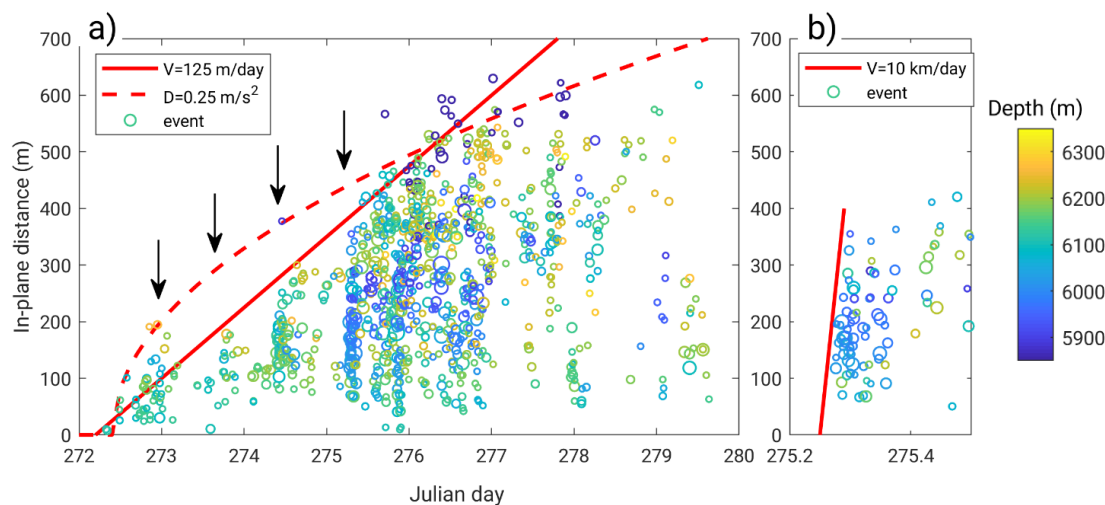


Figure 1.11: Spatial and temporal distribution of seismic events. A zoom plot of the rapid migration on Julian day 275.2 to 275.5 is in (b). (De Barros *et al.*, 2020).

De Barros *et al.* (2020) used a high-resolution relocation method to study the spatial and temporal evolution of a seismic swarm in 2015 in the Corinth Gulf in

Greece. The evolution of seismic swarms from the onset location is plotted in Fig. 1.11 (a). The migration fits the fluid diffusion mode in Eq. 1.3 from Shapiro *et al.* (1997), with a hydraulic diffusivity of  $0.25 \text{ m}^2/\text{s}$  (red dashed line). The constant slip front propagation speed is  $125 \text{ m/d}$  (solid red line in Fig. 1.11 (a)), which is consistent with the fluid-driven mechanism of seismicity interpreted by Vidale and Shearer (2006) and Chen *et al.* (2012). Among the constant migration at the velocity of  $125 \text{ m/d}$ , several apparent short-period intense events occurred from day 272 to 276 (arrows in Fig. 1.11 (a)). These intense clusters of seismic events migrated with a velocity ranging from  $2.7 \text{ km/d}$  to  $10 \text{ km/d}$  (the burst from day 275.2 to 275.4 in Fig. 1.11 (b)), in accordance with other aseismic-driven swarms (Llanos *et al.*, 2015; Lohman and McGuire, 2007).

Table 1.1: Migration speeds of different earthquakes

Swarms	$D \text{ (m}^2/\text{s)}$	Migration velocity	Distance after 3 days (km)	Mw	N/I
Kumamoto earthquake (Kato <i>et al.</i> , 2016)	0.01-1	20 km/d	80	7.0	N
Salton Through, California (Lohman and McGuire, 2007)	44	2.4-24 km/d	72	5.1	N
Youngstown, Ohio (Kim, 2013)	$9.15 \cdot 10^{-4}$	4 m/d	0.012	3.9	I
Nojima, Japan (Tadokoro <i>et al.</i> , 2000)	0.116	48-960 m/d	2.88	-2 to +1	I
Long Valley, California (Hill <i>et al.</i> , 1990)	-	30 m/d - 12 km/d	36	5.1	N
KTB induced seismic (Shapiro <i>et al.</i> , 1997)	$\sim 1$	$\sim \text{m/d}$	$\sim 0.5$	(-1.5)1.2	I
Basel geothermal site (GoertzAllmann <i>et al.</i> , 2011)	0.05	$\sim 50 \text{ m/d}$	$\sim 0.15$	3.4	I

A list of different values of earthquake migration speeds is provided in Table 1.1. Diffusivities here are computed fitting the diffusion mode in equation (1.3) from Shapiro *et al.* (1997). In the Kumamoto earthquake, diffusion coefficient  $D = 200 \text{ m}^2/\text{s}$  when fitting Shapiro *et al.* (1997)'s model, which is higher than the crustal fluids  $D$  ranging from  $0.01$  to  $1 \text{ m}^2/\text{s}$ .

How these different speeds of migration are induced will be discussed in section 1.4.

### 1.2.3 Aseismic slip

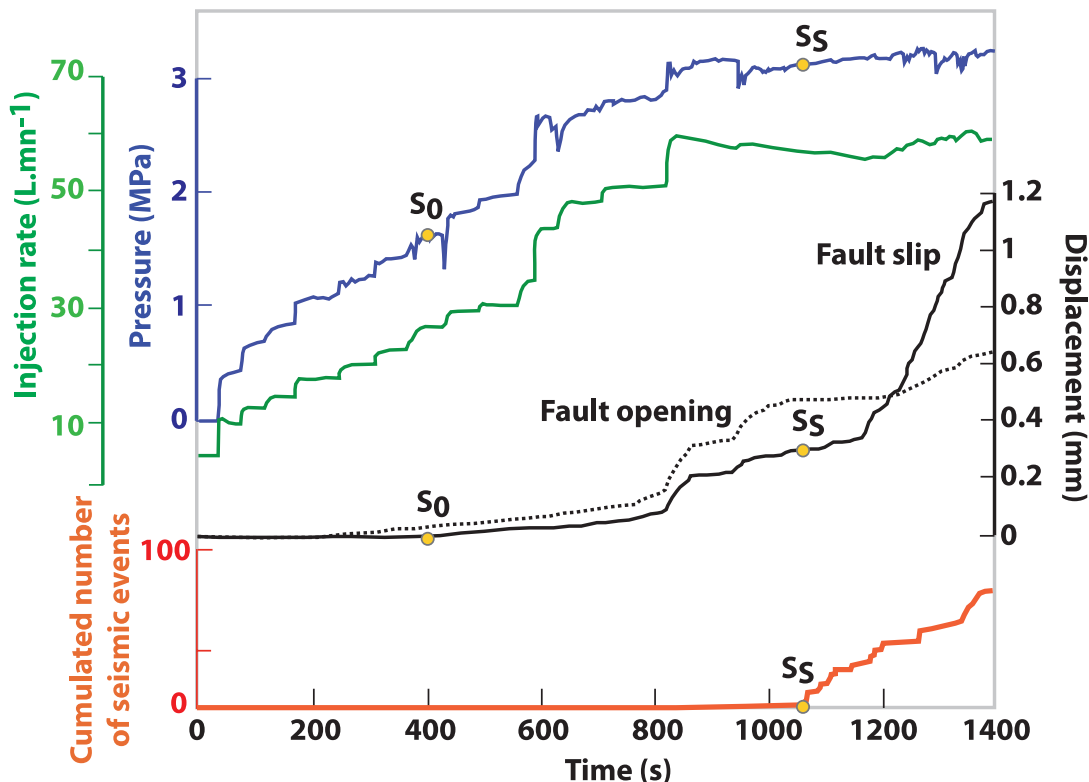


Figure 1.12: Observation of aseismic slip within an in-situ injection experiment by Guglielmi *et al.* (2015b). Temporal evolution of fluid pressure (blue), the injection rate (green), fault slip (solid black line), normal displacement (dashed black line), and cumulative number of induced earthquakes (red) during the 1400-s-long injection.

Apart from the micro-seismic activity and large magnitude induced earthquakes, fluid injection accelerates aseismic slip. Aseismic slip is normally a very slow slip ( $\sim$  mm/yr), whose motion is hard to record or detect without proper monitoring methods (Cornet, 2016; Wei *et al.*, 2015). In recent years, researchers have found that

aseismic slip, without measurable seismic activities, plays a role in the nucleation of induced seismicity. Observations of aseismic slip were identified at a geothermal site in Soultz, France, thanks to a large swarm of repeating microearthquakes (Bourouis and Bernard, 2007). In-situ fault injection experiments observed aseismic slip along the fault promoted by an increase of fluid pressure (Cappa *et al.*, 2019; Cornet, 2016; Eyre *et al.*, 2019; Guglielmi *et al.*, 2015a,b; Lengliné *et al.*, 2017). As shown in Fig. 1.12, slow aseismic slip at the order of micrometers per second ( $\mu\text{m/s}$ ) was observed in the in-situ experiment in southern France at a depth of 518 m (Guglielmi *et al.*, 2015b).

Later, Duboeuf *et al.* (2017) conducted field injection tests and the results show that injection mainly caused the aseismic slip, which resulted in micro-seismicity. Then, the stress transfer propagation related to aseismic slip causes distant earthquakes (Eyre *et al.*, 2019). Thus, aseismic slip is another way to explain earthquake migration. In addition, seismic event migration (m/day, suggesting aseismic slip front propagation) was observed during a natural earthquake swarm in the Corinth Gulf, Greece (De Barros *et al.*, 2020), along with rapid seismic bursts (showing migration at about km/day, see Fig. 1.11). Other recent numerical studies based on Corinth swarm (Dublanche and De Barros, 2021) and fluid injection experiments (Bhattacharya and Viesca, 2019) revealed that slip front propagation outpaces fluid diffusion and is indirectly associated with hydraulic diffusivity. However, what controls the maximum slip of induced seismicity and the front propagation of aseismic slip is not yet fully understood.

## 1.3 Simplified conceptual models of fluid-induced fault slip

In this section, different conceptual models of fluid-induced fault slip will be introduced.

### 1.3.1 Pore pressure change

The fundamental mechanism of fault reactivation is that the pressure change caused by fluid injection reduces the effective normal stresses (Fig 1.13) on pre-existing faults. The pre-existing fault or fracture is stable or closed due to the initial subsurface stress and frictional balance. The normal stress  $\sigma_n$  will be reduced to effective normal stress  $\sigma'_n = \sigma_n - P$  under pore pressure  $P$  (Fig 1.13(a)). When the shear stress

$\tau$  caused by initial far-field maximum and minimum principal effective stresses  $\sigma_1'$  and  $\sigma_3'$  is not beyond the frictional failure envelope  $\mu\sigma_n'$  ( $\mu$  is friction coefficient of the pre-existing surface), the fracture or fault keeps stable (Fig 1.13(b)). The slippage will not occur until the Mohr-Coulomb reaches the Coulomb failure criterion (Barton, 1976; Byerlee, 1968; Byerlee, 1978; Jaeger *et al.*, 2009) as follows:

$$\tau < \mu(\sigma_n - P) \quad (1.5)$$

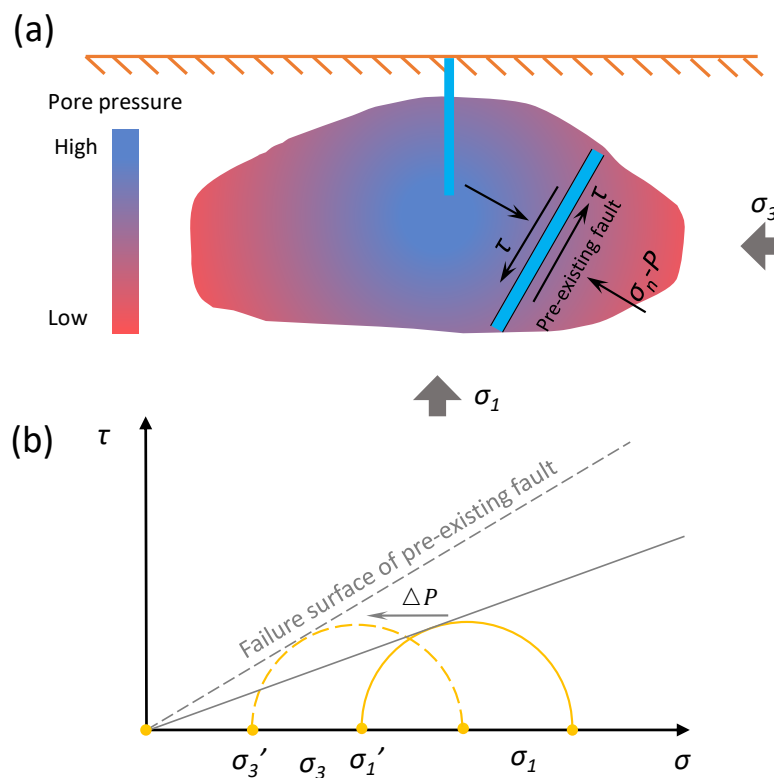


Figure 1.13: (a) Schematic model of fault plane within injection region reactivated by fluid injection and (b) Mohr-coulomb failure criterion showing fluid injection reduces effective stress and induce shear failure.  $\sigma$  and  $\tau$  are effective normal stress and shear stress on the pre-existing fault.

Equation 1.5 originates from Coulomb in 1785 and is usually used as a standard criterion for estimating fault reactivation. Based on equation 1.5, Byerlee (1978) did friction experiments on rocks and concluded that the shear and normal stress at

failure should relate by:

$$\tau = \begin{cases} 0.85\sigma_n & : \sigma_n \leq 200MPa \\ 50 + 0.6\sigma_n & : \sigma_n > 200MPa \end{cases} \quad (1.6)$$

which is referred to as Byerlee's rule.

### 1.3.2 Poro-elasticity

In the far field away from the injection borehole, the pre-existing fault may also be reactivated indirectly by fluid pressure. Segall (1989) considered additional effects of poroelastic coupling of stress and pore pressure to modify the standard model of injection-induced seismicity in Coulomb strength. Fig. 1.14 illustrates how poroelasticity changes the stress state along the far-field fault and moves the stress circle close to failure.

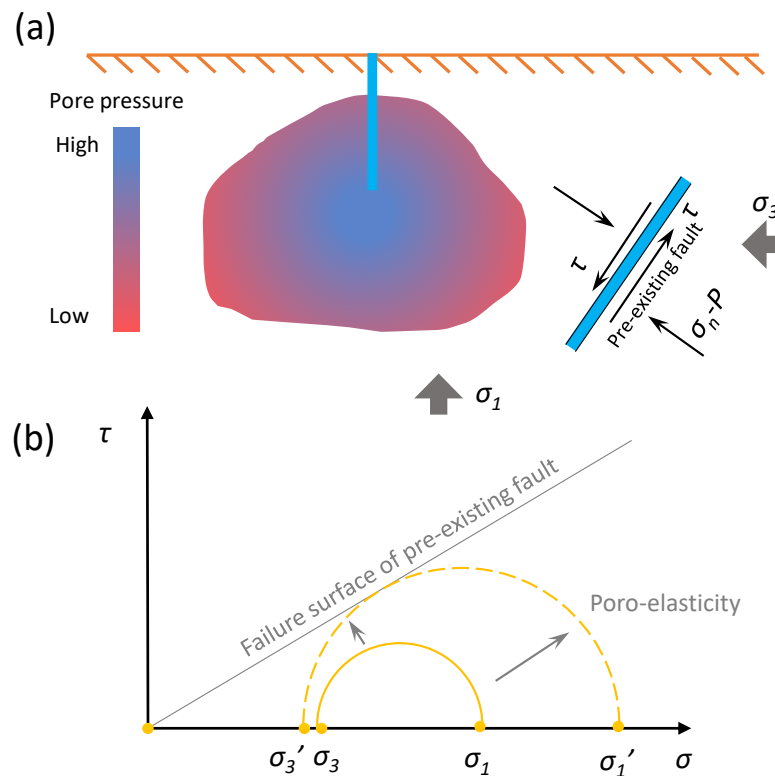


Figure 1.14: (a) Schematic model of fault plane beyond injection region reactivated by poroelasticity and (b) Mohr-coulomb failure criterion showing fluid injection reduces effective stress and induce shear failure

### 1.3.3 Aseismic slip

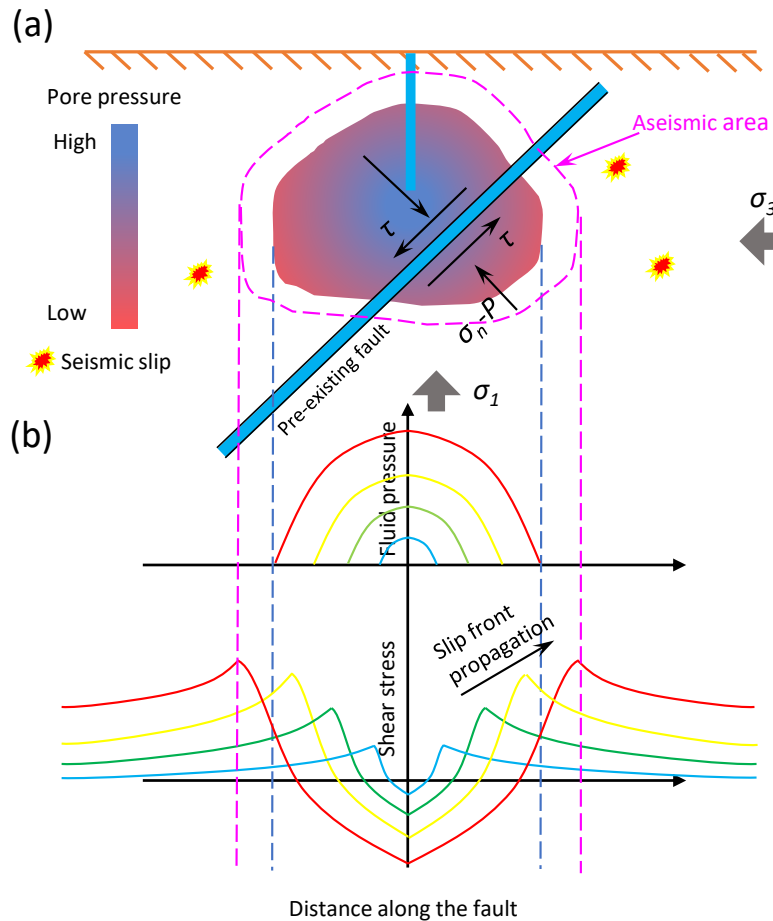


Figure 1.15: (a) Schematic model of fault plane reactivated by aseismic creep (b) Fluid pressure and shear stress evolution along the fault

Another model interpreting fault reactivation is aseismic slip. Cappa *et al.* (2019) combined in-situ measurements, laboratory experiments and numerical models and found that pore pressure accelerated aseismic creep and fault opening, which increases shear stress beyond the pressure front and induced earthquake. In the conceptual model shown in Fig. 1.15 (a), along fault exists in the injection area. The increase in fluid pressure induces a reduction of normal stress and then accelerates aseismic creep and fault opening (see stress curve evolution in Fig. 1.15 (b) and

observation in Fig. 1.13). The aseismic slip front generates peaks in shear stress. As the fluid pressure increases further, concentrated shear peaks and aseismic slip outpace the fluid pressure front and trigger seismic events in non-pressurized regions. Detailed interpretation of this conceptual aseismic slip model will be discussed in session 1.4.1.

### 1.3.4 Fluid injection volume

McGarr (2014) proposed that the maximum magnitude is based on the total injected volume. This theory proposed an upper bound for the maximum seismic moment  $M_0^{max}$  (black solid line in Fig. 1.7)

$$M_0^{max} = \Delta V \cdot G \quad (1.7)$$

where  $\Delta V$  is the total fluid injection volume and  $G$  is the shear modulus of the fault area. However, the magnitude of some observed induced earthquakes including EGS (Diehl *et al.*, 2017; Kim *et al.*, 2018), hydraulic fracturing (Atkinson *et al.*, 2016) and field experiment (Guglielmi *et al.*, 2015b) exceeded the threshold. Thus, the Equation (1.7) was improved by Li *et al.* (2021) denoting a stress ratio  $c$  as the proportion of the full stress drop magnitude:

$$M_0^{max} = \frac{1}{2(1-c)} \Delta V \cdot G \quad (1.8)$$

Equation (1.8) redefines the upper bound limit (black dashed lines in Fig. 1.7) for the maximum magnitudes of induced earthquakes, correlating with initial stress state, total injection volume and material properties.

## 1.4 Experimental study of fluid induced fault reactivation

To better understand the fluid induced fault reactivation, one needs to compare observations with physics based models. This will allow testing conceptual models. In this section, I make a review of experimental attempts, including in-situ scale injection experiments and laboratory experiments.

### 1.4.1 In-situ experiments

Injection experiments in the field are often performed at very shallow depths, enhancing aseismic contributions. An in-situ fluid injection experiment (Derode *et al.*,

2013; Guglielmi *et al.*, 2015b) on shallow crustal faults mentioned above was the first to measure the fluid-induced aseismic slip and pore-pressure evolution at the fault. The in situ injection test was in the Low-Noise Underground Laboratory in southeastern France in 2010. The fault zone was injected with an increasing rate of fluid over 1400 s and the pore pressure, flow rate, shear and normal displacement were recorded. The seismic events, fault slip, and injection parameters (rate & pressure) were measured and plotted in Fig. 1.12. This in-situ experiment observed a fault slip of 0.3 mm and fault opening before the seismic events (black solid and dash lines in Fig. 1.12), which is evidence of observation of aseismic slip induced by fluid injection (Guglielmi *et al.*, 2015b).

At the same site of underground laboratory where the injection experiment (Guglielmi *et al.*, 2015b) was conducted, another set of fluid injection experiments were done to better understand the connections between fluid diffusion, aseismic slip and seismicity (Duboeuf *et al.*, 2017). Through their experimental data, most of the deformations induced by injection were aseismic (only less than 4% were seismic). Moreover, Duboeuf *et al.* (2017) indicated that the distribution of seismicity could not be interpreted by a simple diffusion mode. The observed seismicity is more likely driven by the stress perturbation from the aseismic motion.

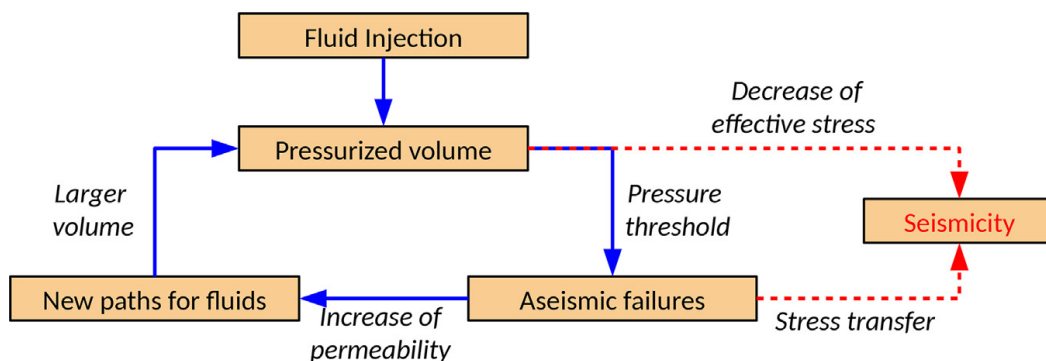


Figure 1.16: A dual process model proposed by De Barros *et al.* (2018) interpreting the seismicity driven by aseismic slip (stress transfer) and fluid pressure (effective stress decrease).

Similarly, the decametric in-situ injection experiments in low-permeable shale and high;y-fractured limestone formations conducted by De Barros *et al.* (2018) showed that the main induced deformation was aseismic. From the in-situ experiment, a model of dual process (as shown in Fig. 1.16) for fluid-induced seismicity was

proposed to better interpret the nucleation of seismicity.

### 1.4.2 Laboratorial experiments

In the above subsection, we reviewed the decametric scale injection experiments. Now we are going to introduce the small-scale laboratory tests of induced seismicity. The laboratory experiments generally studied the effect of different hydro-mechanical and injection parameters on fault reactivation behavior.

Goodfellow *et al.* (2015) performed centimeter-scale fluid injection experiments in the laboratory. The tests were on granite samples and were under different triaxial stress. Their results indicated that aseismic deformation is a significant term in the total energy budget, and during fluid pressurization, the main deformation of the fault is aseismic.

Following the in-situ experiment by Guglielmi *et al.* (2015b), Cappa *et al.* (2019) did laboratory injection experiments on the exact rock samples from the fault at the LSBB site (see Fig. 1.18 (A)). Their results revealed that fault could be activated along non-pressurized patches by the aseismic slip in pressurized regions. They confirmed the aseismic creep that increases shear stress beyond the fluid pressure front and promotes earthquake triggering.

Passelègue *et al.* (2018) studied the effect of fluid injection pressure rate and stress conditions on the reactivation of faults by conducting indoor laboratory experiments on a Westerly granite sample with a pre-existing fracture. They pointed out how the local over-pressure and the peak fluid pressure at the injection hole are dependent on the injection pressure rate, where local and intense fluid pressure perturbations reactivate large faults.

In this thesis, a part of the numerical simulations is based on this kind of injection experiment. The detailed experimental setup and assembling will be introduced in Chapter 2 and Chapter 3.

## 1.5 Numerical modeling of fluid injection-induced fault reactivation

Bhattacharya and Viesca (2019) used the experiment data of Guglielmi *et al.* (2015a)

to estimate the hydro-mechanical parameters of an activated fault and the slip evolution with time through a numerical model (Fig. 1.17 A).

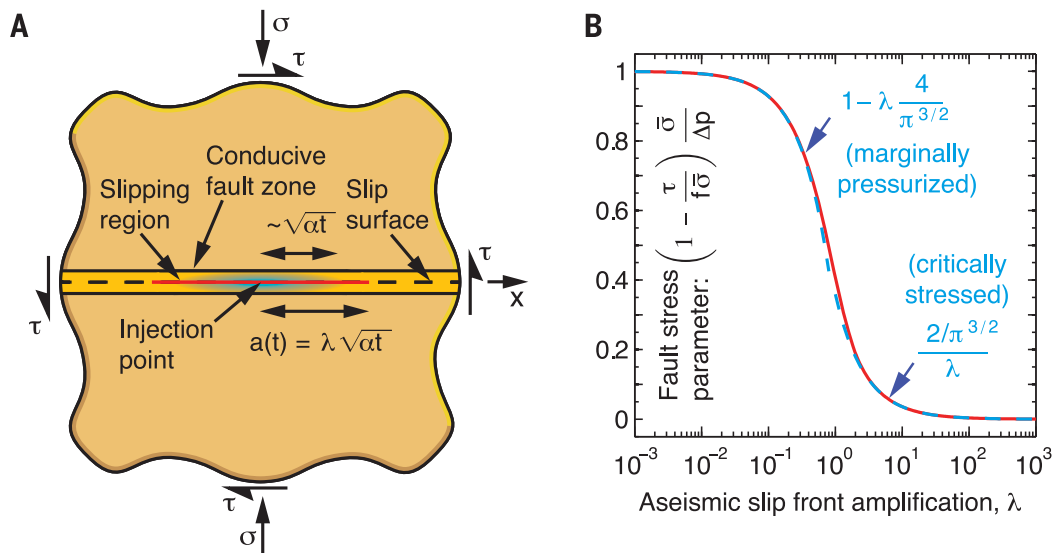


Figure 1.17: Elementary model of aseismic slip front outpace fluid front migration (Bhattacharya and Viesca, 2019)

Bhattacharya and Viesca (2019) find that fluid injection first causes an aseismic slip. As aseismic slip accumulates and the fault is critically stressed, the front of aseismic rupture propagates faster and longer distance than the pore pressure front (Fig. 1.17 B), leading to earthquake nucleation outside the fluid injection region, which has been previously proposed by Garagash and Germanovich (2012) and Viesca (2015). The numerical results are consistent with recent laboratory and in situ observations (Cappa *et al.*, 2019; De Barros *et al.*, 2018; Guglielmi *et al.*, 2015b; Schultz *et al.*, 2017).

A distinct element method (DEM) 3DEC code by Itasca Consulting Group (2016) was developed by Cappa *et al.* (2006, 2018) and Guglielmi *et al.* (2008) to evaluate the coupled hydraulic and mechanical behaviour of cracked rocks or fault zones under fluid pressurization. Results showed that the evolving fault hydraulic diffusivity depends on stress and fluid pressure (Guglielmi *et al.*, 2015a). A fault dynamics model was configured by Cappa *et al.* (2019) coupling fluid diffusion, stress- & strain-dependent permeability and frictional properties. A 3D distinct element hydro-mechanical model using 3DEC code with indoor laboratory frictional setup

(Collettini *et al.*, 2014; Scuderi and Collettini, 2016; Scuderi *et al.*, 2017) was developed to simulate an in situ fluid injection experiment (Guglielmi *et al.*, 2015b), which integrated laboratory and in situ monitoring results. A planar fault with a dip of 70° in an elastic material property was built and injection pressure as recorded in situ (Guglielmi *et al.*, 2015b) was applied. The pre-injection initial stress state of the fault was shear stress  $\tau_0$  and effective normal stress  $\sigma'_{n0} = \sigma_{n0} - p_0$ . The friction equation was governed by the rate-and-state friction law (Eq. 1.9), stemmed from laboratory experiments (Dieterich, 1979; Marone, 1998; Ruina, 1983).

$$\mu = \mu_0 + a \ln \frac{v}{v_0} + b \ln \frac{\theta v_0}{d_c} \quad (1.9)$$

where  $\mu_0$  is the steady state friction coefficient at speed  $v_0$ ;  $a$  and  $b$  are empirical constants, rate weakening occurs when  $a-b < 0$  and rate strengthening when  $a-b > 0$ ;  $v$  is the frictional slip rate;  $d_c$  is the critical slip distance and  $\theta$  is the state variable, representing the average age of the micro contacts. Along the fault, the parameters of the rate-and-state friction and fluid diffusivity keep uniform, while the pressure increases and fluid diffuse in the medium. According to the increased pressure  $p$ , shear stress was reduced to  $\tau = \mu \cdot (\sigma_n - p)$ . This 3DEC method had been coded to study the cracked rock mechanics under fluid injection (Cappa *et al.*, 2006) and to better understand the seismic rupture and off-fault fracture response (Fälth *et al.*, 2015).

The results of the numerical model show that aseismic slip propagates and develops beyond the fluid diffusion area, where normal stress stays at a high value and shear stress accumulates. As a result, the propagating aseismicity triggers seismic slip in the far field. Cappa *et al.* (2019)'s results (Fig. 1.18) correspond with McClure and Horne (2011) and Gischig (2015)'s theoretical research on pressurized rate-and state faults, proving that shear strength and friction weakening can stimulate the slip beyond the pressure front. The critical nucleation length  $L_c$  (Eq. 1.10) is the critical size for an unstable slip in the earthquake mechanics and nucleation theory (Scholz, 2019). For rate-and-state friction law:

$$L_c = \frac{G d_c}{(\sigma_n - p)(b - a)} \quad (1.10)$$

where  $G$  is the shear modulus. Fault slip remains stable (aseismic) in their results when the pressurized fluid diffusion length didn't exceed  $L_c$ . Afterward, the accelerating aseismic creep along the fault propagated and forced the fault to be in an unstable and seismic state.

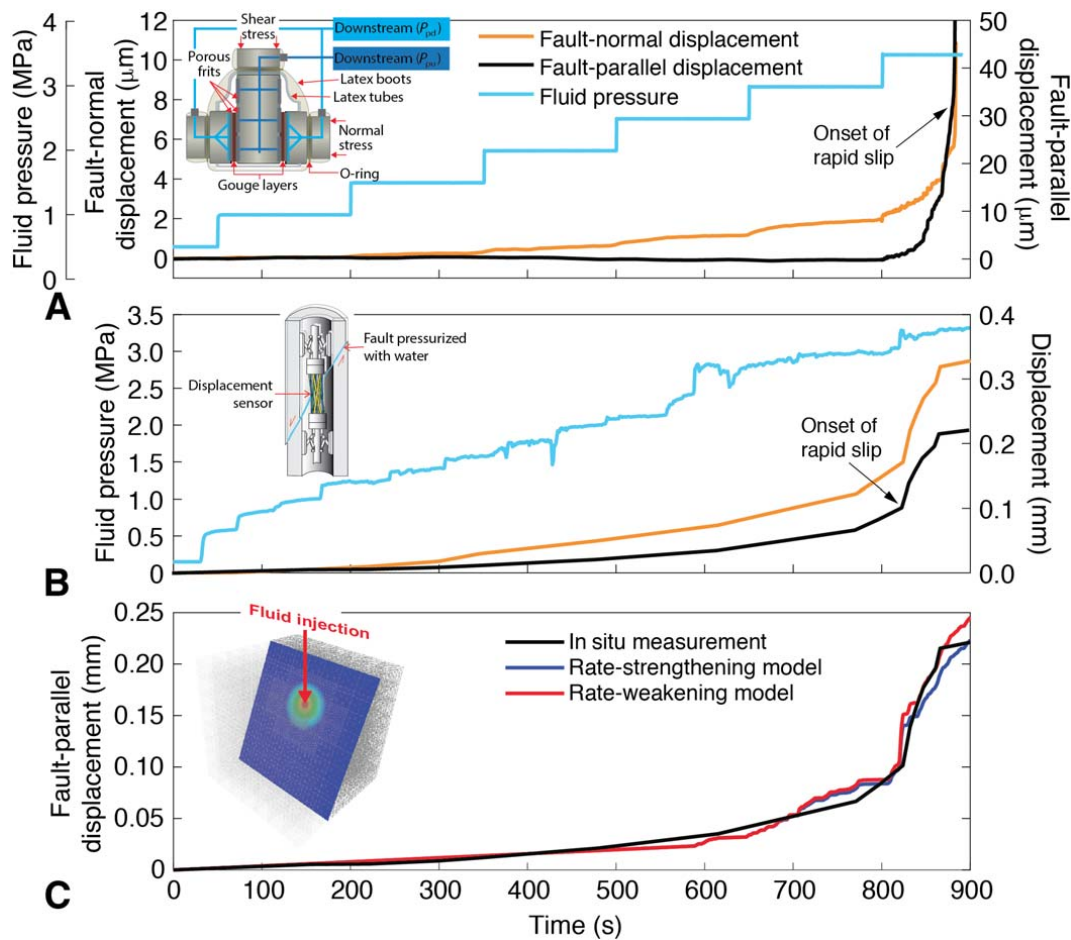


Figure 1.18: Conceptual illustration of stress stability, creep and seismic slip induced by fluid injection with experimental and numerical studies. Fault movements are induced over time by fluid injection. Fluid pressure and fault displacements were measured during fluid injection in (A) laboratory and (B) in situ experiments. (C) Agreement between observed and modeled slip and influence of the frictional model. (Cappa *et al.*, 2019)

Another recent numerical model (Dublanche and De Barros, 2021) interpreted earthquake swarms. The model couples the geometry of a tectonic fault based on the Corinth swarm (Greece) (De Barros *et al.*, 2020), elasticity, a nonlinear time- and space-dependent hydraulic diffusivity, rate-and-state friction law. The rate-and-state friction coefficient and the time- and space-dependent hydraulic diffusivity are solved numerically following the model proposed by Dublanche (2019) (basic

geometry of the numerical model in Fig. 1.19). The model reproduced the migration speeds in Corinth swarms (Fig. 1.11). Results show that the migration rate of the slip front is independent of the permeability and hydraulic diffusivity. The size of the aseismic slip region is larger than the pressurization area, which shows the seismic front can be ahead of the fluid pressure front. This recent numerical model suggests that the seismic migration is controlled by aseismic slip propagation and the resulting stress perturbation, rather than the fluid diffusion which leads to pore pressure variation on faults triggering seismic failure (Shapiro and Dinske, 2009; Shapiro *et al.*, 1997).

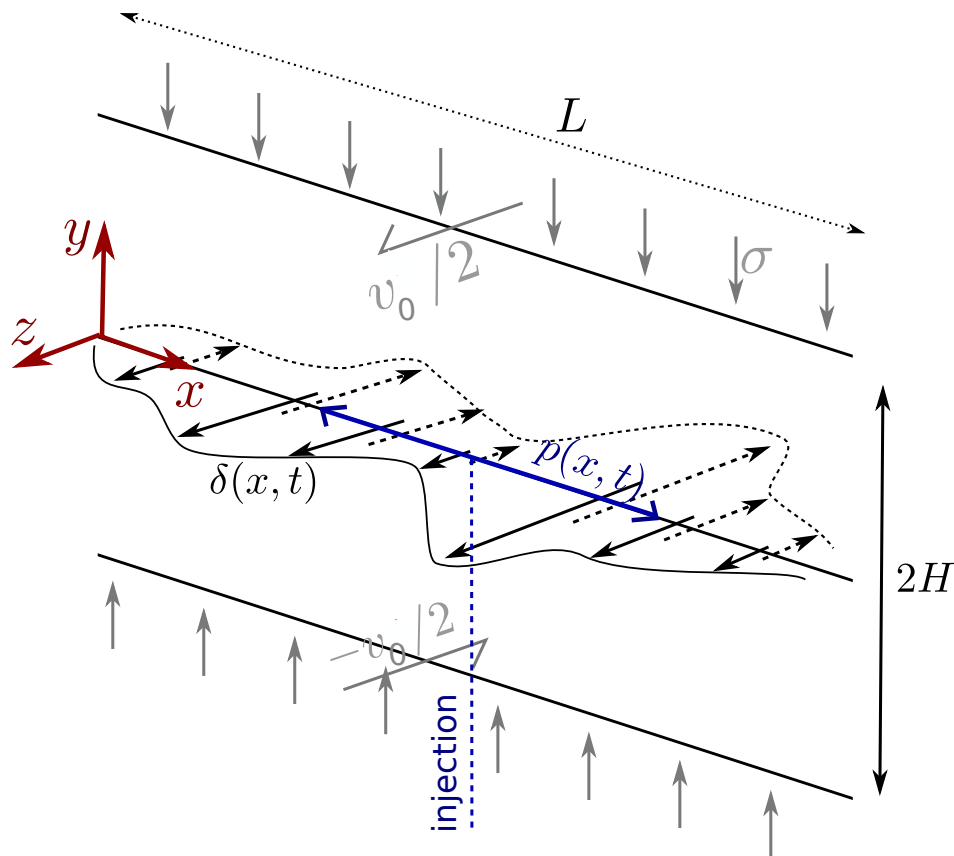


Figure 1.19: Geometry of the rate-and-state frictional fault model, whose shear cracks are driven by fluid.  $L$ : the length of the fault;  $H$ : the thickness of the elastic slabs in contact;  $\sigma_0$ : the lithostatic stress;  $v_0$ : the imposed slip rate at  $z = \pm H$ . (Dublanche, 2019)

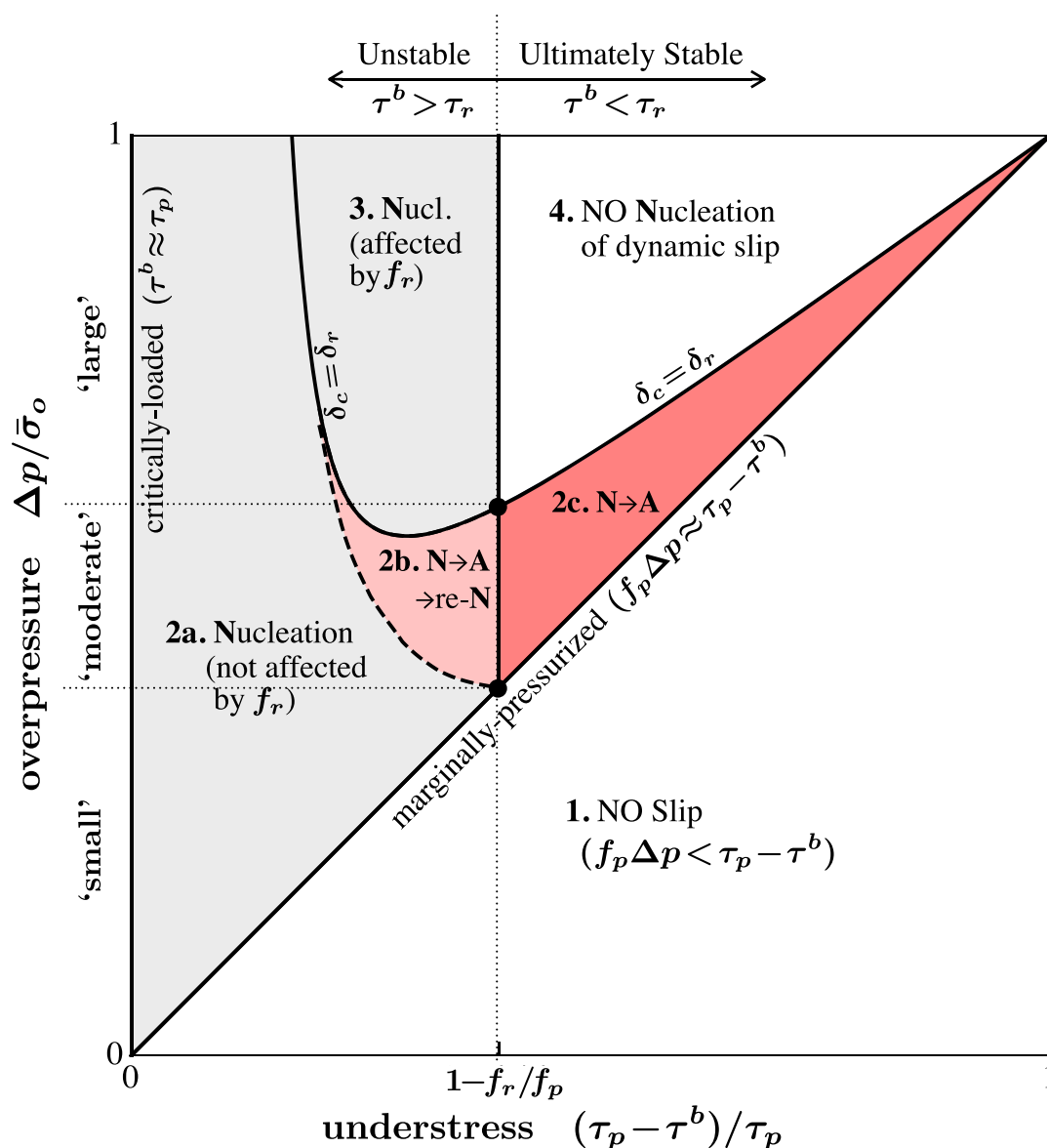


Figure 1.20: Map of different slip state in the relation between under-stress and overpressure. 1. No fault slip. 2. Nucleation of fault slip without the influence of residual friction  $f_r$  (dynamic friction coefficient). 3. Nucleation of dynamic slip influenced by  $f_r$ . 4. No dynamic slip nucleation for "large" overpressure on ultimately stable fault. (Garagash and Germanovich, 2012)

Another theoretical model developed by Galis *et al.* (2017) incorporating dynamic

rupture physics shows a scaling relation of the form:

$$M \propto \Delta V^{3/2} \quad (1.11)$$

where  $\Delta V$  is the total fluid injection volume. This theoretical model is validated by simulations and suggests that most of the induced seismicities are self-arresting ruptures which can be described with equation (1.11). However, due to strong pressure perturbations, runaway ruptures are likely to occur. This model also follows the numerical model of Garagash and Germanovich (2012), which is also based on fracture mechanics. In Garagash and Germanovich (2012)'s model (shown in Fig. 1.20), they studied the direct effect of fluid diffusion on the onset of dynamic slip. Both these two models based on rupture mechanics found the propagation of dynamic rupture is sensitive to the initial stress state of the fracture.

Table 1.2: Summary of different injection-induced seismicity numerical models

Numerical model	Geometry	Friction	Fluid flow	Main results
Bhattacharya et al. (2019)	1D	Slip weakening	Constant diffusivity	Aseismic rupture front outpace fluid migration
Cappa et al. (2019)	2D	Rate-and-state	Stress-and-strain dependent permeability	Seismicity is triggered indirectly by fluid injection but aseismic creep
Dublanchet et al. (2021)	1D	Rate-and-state	Space-and-time dependent diffusivity	Migration speed is controlled by mean stress but not diffusivity
Galis et al. (2017)	2D	Slip-weakening	Constant diffusivity	Relation between largest magnitude and injected volume
Garagash et al. (2012)	1D	Slip weakening	Constant diffusivity	Slip evolution in relation between fault initial stress and pore pressure. (Fig. 1.20)

In summary, Table 1.2 shows a list of current numerical models dedicated to the study of fluid-induced fault slip. In the table, 1D represents a one-dimensional fault, and 2D is a two-dimensional fault plane. Many of these models are based on constant hydraulic diffusivity, while stress-and-strain dependent permeability (Cappa *et al.*, 2019) and space-and-time dependent hydraulic diffusivity (Dublanchet and De Barros, 2021) are applied in the numerical models. And as shown by Guglielmi *et al.*

(2015a), hydraulic properties may influence fault slip. Now I will discuss what we know about the fault's hydraulic properties.

## 1.6 Hydraulic fault's properties

As discussed in the previous sections of this chapter, fluid pressure diffusion in the permeable fractured rock formations or fault zones might lead to detectable seismic events within underground fluid injection (Ellsworth, 2013; Keranen *et al.*, 2014). The fluid diffusivity of the fractured zone is a key property influencing fault slip. It was indicated from experimental studies that the hydraulic diffusivity change influences the fault slip modes after reactivation, whatever seismic or aseismic (Guglielmi *et al.*, 2015a; Scuderi and Collettini, 2016; Scuderi *et al.*, 2017). Understanding how hydraulic properties of a fault evolve during fluid injection is important in predicting the slip behavior (Cappa *et al.*, 2018).

According to Darcy's law and law of conservation of mass to fluid mass, pore pressure distributes in the fault plane due to a high-pressure source following the diffusion equation

$$\frac{d}{dt}p = D \frac{d^2}{dx^2}p \quad (1.12)$$

where  $D$  is the hydraulic diffusivity,  $t$  is the diffusion time and  $x$  is the distance to the injection hole (Shapiro *et al.*, 1997; Yamashita, 1997). The hydraulic diffusivity  $D$  is given by

$$D = \frac{k}{\phi\mu C_f} \quad (1.13)$$

where  $k$  is permeability,  $\phi$  is porosity,  $\mu$  is the fluid viscosity and  $C_f$  is the compressibility of the fluid and the pore space of rock (Jaeger *et al.*, 2009). The value of hydraulic diffusivity is generally expected to be between 0.01 to 10 m<sup>-2</sup>/s (Scholz, 2019), estimated from the classical model where the diffusion of fluid leads to pore pressure change and then causes effective normal stress of fault change which causes fault slip (Shapiro and Dinske, 2009). In this classical model, the fluid front is tracked by the seismic swarm expansion so that the hydraulic diffusivity is estimated by the front migration. While recent researches (Cappa *et al.*, 2006; Doan *et al.*, 2006; Guglielmi *et al.*, 2008) indicate that the hydraulic diffusivity value is lower in the fault damage zone.

An in-situ injection experiment tested the hydraulic diffusivity. The experiment monitoring fault movements, injection pressure and flow rate were conducted by Guglielmi *et al.* (2015a) using an instrumental device that allows the synchronous monitoring of fault movement during pressurization by fluid in the borehole interval of the fault zone. Hydraulic diffusivity was obtained to increase from  $\sim 2 \times 10^{-9}$  initially to  $\sim 10^3 \text{ m}^2\text{s}^{-1}$  linking to a complex 3D fault movement.

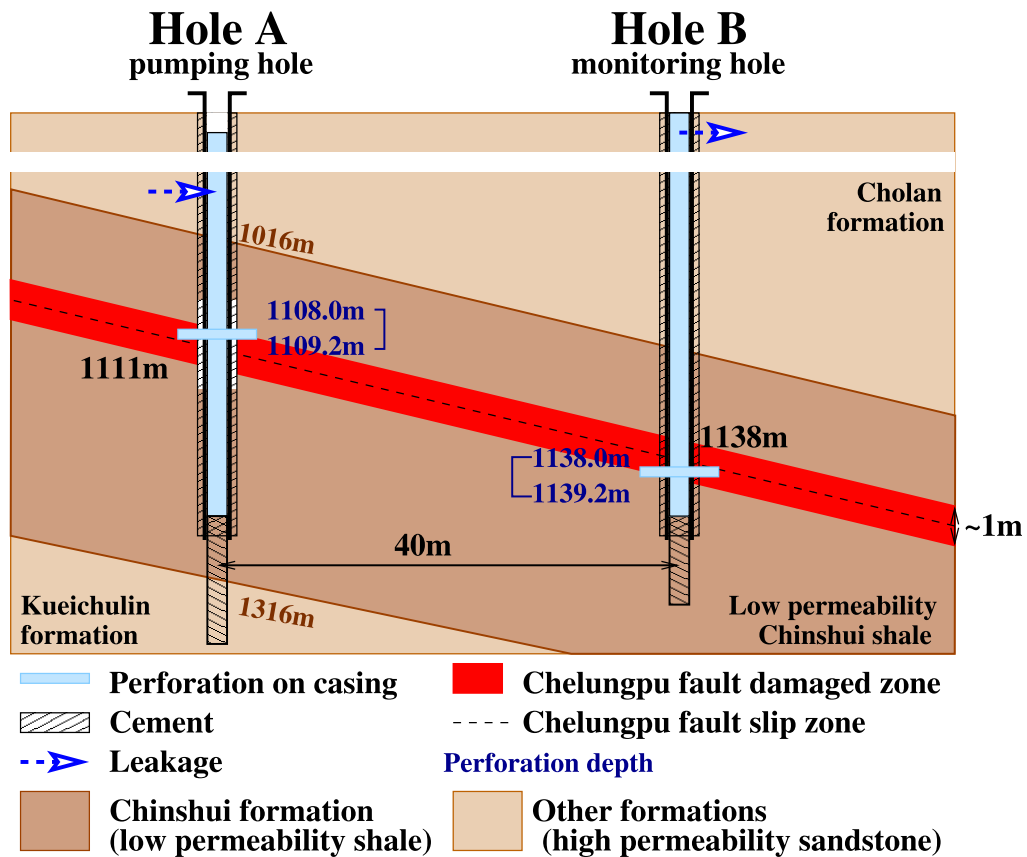


Figure 1.21: Configuration of pumping test on Chelungpu fault boreholes. (Doan *et al.*, 2006)

There are few in situ hydraulic diffusivity observations on active faults. Another injection experiment was conducted by Doan *et al.* (2006) on the Chelungpu fault damage zone after the  $M_w$  7.6 1999 Chichi earthquake. A pumping test was on a pair of boreholes separated by 40 m (Fig. 1.21). Water was pumped out of the hole A and the water level of both hole A and B was recorded in the following 3 months. Doan

*et al.* (2006) extracted a value of hydraulic diffusivity for the fractured damage zone of  $D = (7 \pm 1) \times 10^{-5} \text{ m}^2 \cdot \text{s}^{-1}$ . This value is low enough to confine the pressurized fluid during the earthquake.

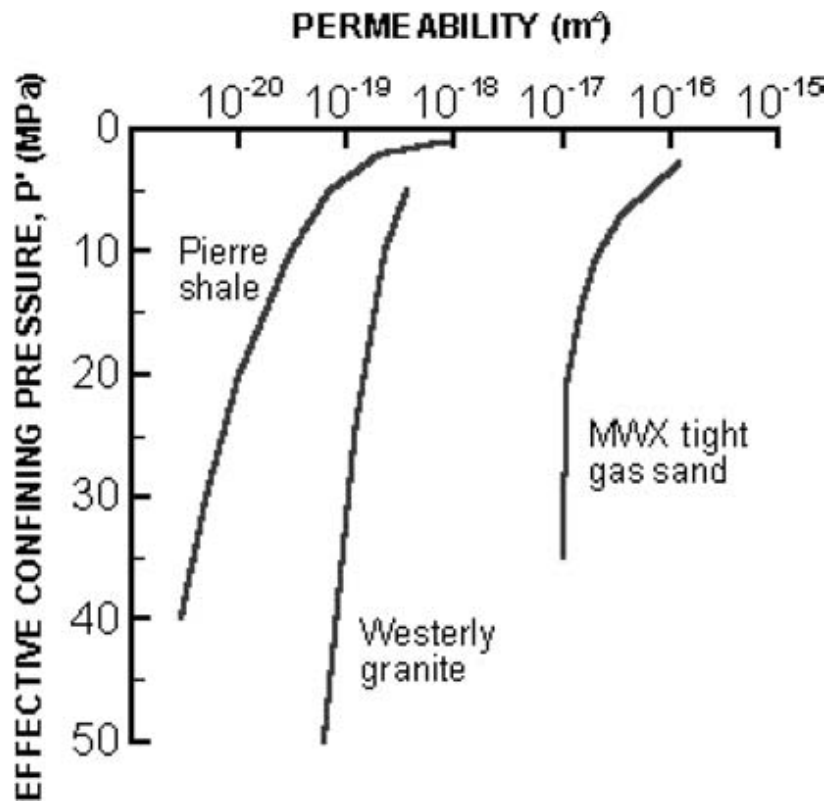


Figure 1.22: Permeability versus effective confining pressure for intact rock (Rutqvist and Stephansson, 2003)

The hydraulic diffusivity is in fact strongly influenced by permeability (equation (1.13)). The question of what controls permeability has motivated many experiments in the laboratory. Many experiments are conducted to research the intact rock permeability (pressure dependence of permeability, shown in Fig. 1.22) dependence with both confining pressure and fluid pressure (Bernabe, 1986; Brace *et al.*, 1968; Kilmer *et al.*, 1987; Neuzil, 1986; Rutqvist and Stephansson, 2003). Some models as well are used to match the observation of permeability relationship with confining pressure and fluid pressure, including exponential functions (Louis *et al.*, 1977), power functions (Kranzz *et al.*, 1979) and logarithmic function (Jones and Owens, 1980). From the results of laboratory experiments applying axial load on the rock

sample (Souley *et al.*, 2001; Wang and Park, 2002; Zoback and Byerlee, 1975), the permeability reduces about one order of magnitude due to the closure of existing pores and microfractures caused by stress increase. When axial loading is over half of the rock strength, the permeability increases with the unstable crack growth (Rice, 1992). On the other hand, the permeability of the fracture can be raised when shear slip occurs on the fault as the shear slip affects rock fragmentation, fracture roughness and the breakdown of closure (Barton *et al.*, 1995).

## 1.7 Objective of the research

In summary, we have presented a broad view of observations on seismicity and fault slip in general induced by different types of fluid injection-involved projects. Then, we clarified the general features of induced seismicity, including:

- total injection volume dependence of earthquake magnitude;
- seismic migration velocity;
- aseismic slip.

In the second step, simplified conceptual models with different geometry and induced mechanisms have been introduced. Then we have presented a brief review of the experimental and modeling framework that has been developed over the past years to study fault slip reactivation by fluid. After summarizing the main outcomes of these studies, we found the following physical and mechanical parameters have an effect on the induced seismicity:

- hydraulic properties of the fault (permeability, hydraulic diffusivity, porosity, etc);
- initial in-situ stress conditions (normal stress, shear stress, confining stress);
- injection properties (injection rate, pore pressure, total injection volume);
- frictional properties (slip weakening, slip strengthening, constant coefficient, residual friction, slip weakening sliding threshold);
- location of the pre-existing fault relative to the injection well (cross the pressurization area, far field, aseismic slip);
- material physical properties (elasticity, Poisson ratio)

In spite of the dense current studies of observations and models of induced seismicity, there are still a lot of important aspects yet to be fully understood:

- How hydraulic and mechanical parameters control the slip front propagation speed;
- The relationship between maximum slip or magnitude and hydraulic properties (injected volume, overpressures, injection rate, etc.).

In this study, we investigate behaviors of the reactivation of pre-existing faults induced by fluid injection. First, we configured 2D and 3D finite element method (FEM) numerical models with the same geometry and calibrated with a set of laboratory experiments (Passelègue *et al.*, 2018, 2020). Coupling with a solver of fluid diffusivity and slip weakening friction criterion allows the model to reproduce experimental results. Parameter tests including stress condition, injection rates, initial stress, and frictional properties are conducted to study the mechanical response of fault slip induced by injection. The aim of the work presented in this thesis is to evaluate the controlling factors for the reactivation of fault slips.

In the following chapters, we are going to organize:

## Chapter 2

This chapter introduces the theoretical framework and numerical simulation approaches of this thesis. The laboratory experiments which our numerical model simulates are first presented. Then we talk about the hydro-mechanical coupling methods of the numerical model, including elasticity, friction mechanics of rock and fluid diffusion and permeability. Afterward, the configuration of the finite element model is discussed. In addition, the diffusion equation solver coupled with our model is interpreted.

## Chapter 3

This chapter aims to clarify the experiment assembling and two calibration models. The first benchmark model is a self-similar fault slip model induced by fluid injection. We use our numerical approaches to simulate the model and verify the results. Then, the experimental assembling of the laboratory model we simulate in this thesis is introduced. We conduct a parameter study on the material properties

to reproduce the experimental results.

#### Chapter 4

This chapter is targeted at parameter studies dedicated to the mechanical control of slip front propagation and maximum slip, using the modeling approach presented in Chapter 2. First, the fluid injection parameters that can be adjusted artificially in the injection experiment are studied. We perform parametric simulations of injection rate and volumes to see how these injection parameters influence the maximum slip of the fault. Then in the following three sections, numerical simulations of the impact of the fault hydro-mechanical and frictional parameters on its reactivation will be conducted. We will compare this thesis's maximum slip and rupture propagation speed with the observations in other induced seismicity studies.

#### Chapter 5

In this chapter, we summarize and conclude the main findings of our research. We also present some perspectives to extend the study initiated here.

# Chapter 2

## Theoretical framework and numerical simulation approach

Résumé . . . . .	42
Summary . . . . .	42
2.1 Experimental set-up . . . . .	42
2.2 Hydro-mechanical coupling . . . . .	44
2.2.1 Elasticity . . . . .	44
2.2.2 Friction mechanics of rock . . . . .	50
2.2.3 Fluid diffusion and permeability . . . . .	54
2.3 Mechanical problem . . . . .	55
2.3.1 Geometry and element mesh . . . . .	55
2.3.2 Loading progress . . . . .	56
2.3.3 Boundary conditions . . . . .	57
2.4 Solving fluid diffusion equation . . . . .	58
2.4.1 Constant permeability/diffusivity . . . . .	58
2.4.2 Non-constant permeability/diffusivity . . . . .	59

## Résumé

Dans ce chapitre, l'expérience d'injection et le modèle numérique simulant la faille sous une pression de fluide injecté croissante sont présentés. Ce chapitre commence par décrire (section 2.1) la mise en place expérimentale du modèle à l'échelle du laboratoire pour la réactivation de failles induite par l'injection. Ensuite, le cadre théorique et les étapes de configuration du modèle sont décrits. Dans la section 2.2, nous dérivons les équations principales en couplant l'élasticité, le frottement et la diffusion des fluides. Ensuite, dans la section 2.3, la configuration du modèle, comprenant la géométrie, le maillage des éléments, les propriétés des matériaux, la progression de la charge, les conditions aux limites et le type de contact, est décrite. De plus, dans la section 2.4, un solveur de l'équation de diffusion est également présenté. Le résultat de l'équation de diffusion est couplé au modèle physique élastique.

## Summary

In this chapter, the injection experiment and the numerical model simulating the fault under increasing injected fluid pressure are presented. This chapter first (section 2.1) describes the experimental set-up of the laboratory scale model of injection-induced fault reactivation. Then, the theoretical framework and configuration steps of the model are described. In section 2.2 we derive the governing equations by coupling the elasticity, friction and fluid diffusion. Next in section 2.3, the model configuration including geometry, element mesh, material properties, loading progress, boundary conditions and contact type are described. In addition, in section 2.4 a solver of the diffusion equation is also presented. The result of the diffusion equation is coupled to the elastic physical model.

## 2.1 Experimental set-up

In this section, the experimental set-up by Passelègue *et al.* (2018) on which our numerical simulation is based will be introduced. The detailed geometry of the rock sample is as follows. A cylindrical sample of Westerly granite of 40 mm in diameter was cored, and then cut and precisely ground to a length of 100 mm. The cylinder was then cut at an angle of 30° with respect to its axis of revolution to create an elliptical saw cut fault interface (Fig. 2.1 A) of 40 mm in width and 80 mm in length along the strike. The fault surface was prepared with a surface grinder. A 4 mm

diameter borehole, the center of which was located at 4.5 mm from the edge of the cylinder, was drilled through the material on one side of the fault, connecting the fault surface to the bottom end of the sample (Fig. 2.1 A). The rock sample is loaded in a triaxial cell. The borehole connected to the fault allows the injection of fluid into it. The loading and injection details are in the following text.

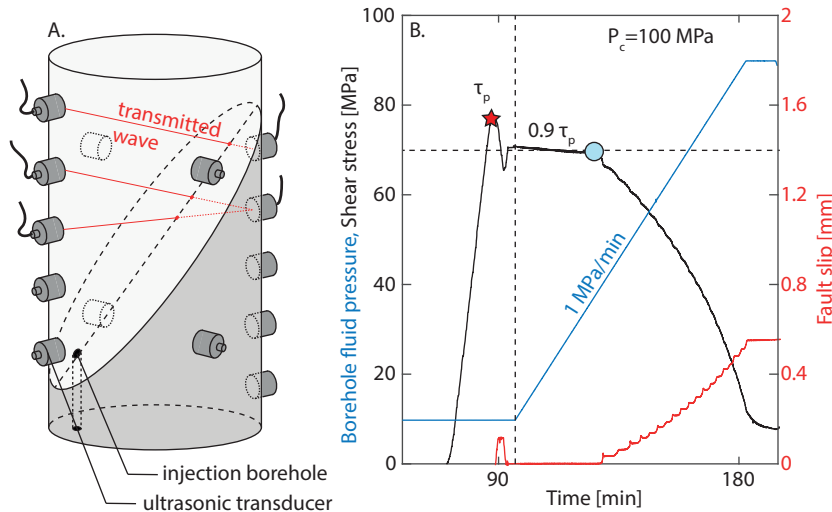


Figure 2.1: Experimental setup. (A) Schematic of the sample assembly. The length of the fault is 8 cm along the strike. The injection is conducted in the bottom sample through a borehole reaching the fault surface. (B) Fluid pressure, shear stress and slip were measured during a sliding test at constant pressure (left of the dotted vertical line) and during a fluid injection test at 1 MPa/min and initial shear stress equal to 90 % of the static frictional strength.(Passelègue *et al.*, 2018)

Passelègue *et al.* (2018) conducted experiments with initial pore pressure set to 10 MPa. There were two confining pressures, 50 and 100 MPa. A pre-injection axial loading test was conducted under constant pore pressure conditions, and it aimed to determine the shear stress  $\tau_p$  at the onset of fault reactivation. Afterward, the axial pressure was unloaded to provide an initial shear stress  $\tau_0$ , which is a specified proportion of  $\tau_p$ . Then a displacement transducer controlled the loading cap to remain still. This unloading procedure is called 'a stress relaxation' test, allowing a certain amount of elastic strain to be stored in the loading cap. The shortening of the fault sample is calculated by the decrease of axial stress and the machine

stiffness. Pore fluid was injected through the borehole connected to the fault, and the injection rate was from 1 to 1000 MPa/min. With different confining pressure  $P_c = 50$  MPa and 100 MPa, the peak value of pore pressure was 40 and 90 MPa.

This laboratory experiment model involves a coupling between the elasticity of the rock, friction and fluid diffusion along the fault. In the next section, we will give the details of these physical ingredients, and we will provide the equations governing the evolution of stress, strain, pore pressure and fault slip in the sample.

## 2.2 Hydro-mechanical coupling

### 2.2.1 Elasticity

To model the rock sample reactivation under triaxial stress and pore pressure, the elasticity equations are used to simulate the experiment. In this section, we will describe the governing equation of elasticity.

To solve hydro-mechanical problems in rock failure and fault reactivation, a series of equations in elasticity is sufficient to give a mathematical solution. The basic governing equation describing particle mechanics is Newton's law, where forces between the interacting objects are opposite in direction and equal in magnitude and force equals mass multiply acceleration. Following Newton's law, the governing law for a deformable body like metal or rock is the stress equilibrium law. All rocks obey the stress equilibrium law and in all processes or conditions occurring in the rock sample or rock mass it must be satisfied, regardless of the relationship between the stress and strain. The continuity of displacement and strain of a deformable body supplies the strain-displacement equations. In linear elasticity, the stress equilibrium law must be complemented by the constitutive equations describing the relationship between stress, strain (Hooke's law (Hooke *et al.*, 2004; Love, 2013)) and other parameters of the material. The boundary conditions are the data to give a unique solution to the linear elastic behavior of a rock mechanics problem. In conclusion, during the analysis the assemblage was required to satisfy three basic conditions: (a) equilibrium of the element forces with the external loads, (b) strain-displacement relationship of the deformed elements so that continuity of strain of the material and the displacement at the joints is maintained at, and (c) stress-strain relationships in the elements that depend on the element properties (Clough, 1990).

The most fundamental problem of elasticity is to determine the stresses and displacements of a body of known shape, given tractions or displacements on the outer boundary of the body, and prescribed volume forces at the interior points. The prescribed interior forces could load on some points or distribute uniformly or inconsistently over the whole body. Such forces are called body forces, and gravity is the commonest body force. In the elasticity application of inner forces, boundary pressures or displacements, a series of partial differential equations need to be solved to obtain the result of the stress state and displacement of the certain body, mentioned as the equation of stress equilibrium above. The equilibrium equations are derived from Newton's second law (Jaeger *et al.*, 2009), described in the next paragraph.

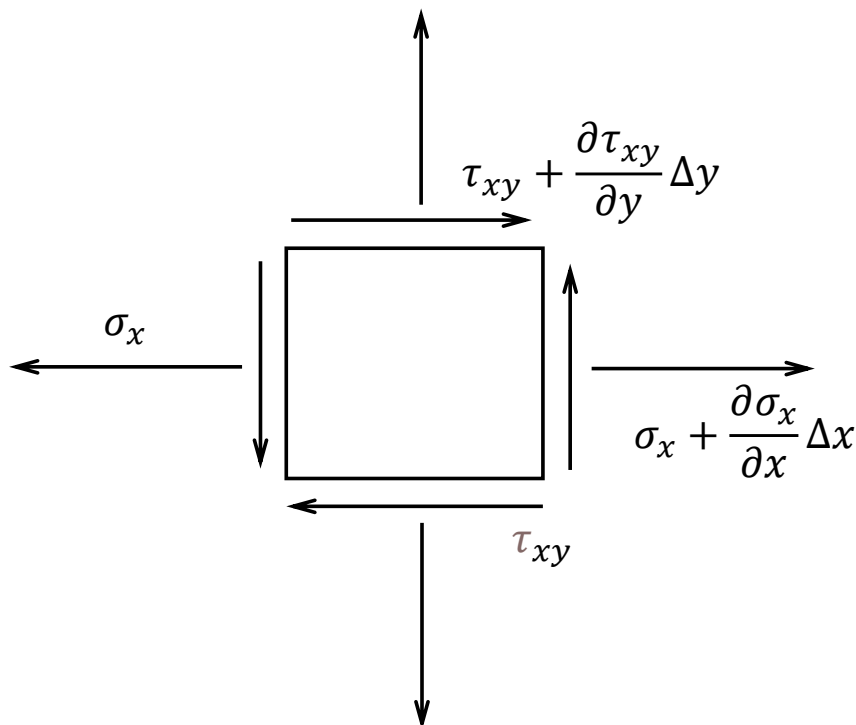


Figure 2.2: A 2D four-node element taken from a material with components of stress to derive the stress equilibrium equation.

Taking a small four-node 2D finite element of material,  $\Delta x$ ,  $\Delta y$ , from a linear body as shown in Figure 2.2, we can write the equations of equilibrium for the stress components in one direction acting on the faces of the element. Since the stresses change as one moves from point to point within the body, a variation in each stress

term is considered using a first-order Taylor series expansion. (For simplicity, only the  $x$  normal and  $xy$  shear stresses are shown.) From Newton's second law that force equals mass multiplied acceleration, summing forces in the  $x$  direction gives:

$$\sum F_x = ma_x \quad (2.1)$$

where  $a_x$  is acceleration in  $x$  direction. The mass  $m$  per unit length along  $z$  direction is density times volume  $\rho dx dy$ . Equation (2.1) can be written to the following.

$$-\sigma_x dy - \tau_{xy} dx + (\sigma_x + \frac{\partial \sigma_x}{\partial x} dx) dy + (\tau_{xy} + \frac{\partial \tau_{xy}}{\partial y} dy) dx + \rho f_x dx dy = \rho dx dy a_x \quad (2.2)$$

In most frequent cases, rocks are in static equilibrium, where displacement occurs slowly. As a result, the right hand of equation (2.2) can be neglected. Dividing equation (2.2) by  $dx dy$  and cleaning the terms gives

$$\frac{\partial \sigma_x}{\partial x} + \frac{\partial \tau_{xy}}{\partial y} + \rho f_x = 0 \quad (2.3)$$

where  $\rho f_x$  is the element force in  $x$  direction.  $X_b$  and  $Y_b$  are the body force in  $x$  and  $y$  direction per unit volume, such as gravity or an electromagnetic force. Writing the stress equilibrium equation in  $x$  and  $y$  direction as following

$$\frac{\partial \sigma_x}{\partial x} + \frac{\partial \tau_{xy}}{\partial y} + X_b = 0 \quad (2.4)$$

$$\frac{\partial \tau_{xy}}{\partial x} + \frac{\partial \sigma_y}{\partial y} + Y_b = 0 \quad (2.5)$$

Considering a three-dimensional element taken from the body under complex loading and boundary conditions, where stresses act in the  $x$ ,  $y$ , and  $z$  directions. The set of stress equations of equilibrium comes next:

$$\begin{aligned} \frac{\partial \sigma_{xx}}{\partial x} + \frac{\partial \tau_{xy}}{\partial y} + \frac{\partial \tau_{xz}}{\partial z} + X_b &= 0 \\ \frac{\partial \tau_{xy}}{\partial x} + \frac{\partial \sigma_{yy}}{\partial y} + \frac{\partial \tau_{yz}}{\partial z} + Y_b &= 0 \\ \frac{\partial \tau_{xz}}{\partial x} + \frac{\partial \tau_{yz}}{\partial y} + \frac{\partial \sigma_{zz}}{\partial z} + Z_b &= 0 \end{aligned} \quad (2.6)$$

where  $Z_b$  is the body force in  $z$  direction per unit volume.

Apart from the stress equilibrium equations, there is another set of equations solving the relationship between strains and displacements. The definition of strain is that the ratio of change in a dimension that happens with the material under stress. According to the definition, the equation of normal strain is given as follows:

$$\varepsilon = \frac{\Delta L}{L} \quad (2.7)$$

where  $\varepsilon$  is normal strain,  $\Delta L$  is the relative change of length  $L$  of the body.

In three dimension, the nine strains can be written in the form of a three-dimensional strain tensor,  $\boldsymbol{\varepsilon}$ :

$$\boldsymbol{\varepsilon} = \begin{bmatrix} \varepsilon_{xx} & \varepsilon_{xy} & \varepsilon_{xz} \\ \varepsilon_{yx} & \varepsilon_{yy} & \varepsilon_{yz} \\ \varepsilon_{zx} & \varepsilon_{zy} & \varepsilon_{zz} \end{bmatrix} = \begin{bmatrix} \frac{\partial u}{\partial x} & \frac{1}{2} \left( \frac{\partial u}{\partial y} + \frac{\partial v}{\partial x} \right) & \frac{1}{2} \left( \frac{\partial u}{\partial z} + \frac{\partial w}{\partial x} \right) \\ \frac{1}{2} \left( \frac{\partial u}{\partial y} + \frac{\partial v}{\partial x} \right) & \frac{\partial v}{\partial y} & \frac{1}{2} \left( \frac{\partial v}{\partial z} + \frac{\partial w}{\partial y} \right) \\ \frac{1}{2} \left( \frac{\partial u}{\partial z} + \frac{\partial w}{\partial x} \right) & \frac{1}{2} \left( \frac{\partial v}{\partial z} + \frac{\partial w}{\partial y} \right) & \frac{\partial w}{\partial z} \end{bmatrix} \quad (2.8)$$

where  $w$  is the displacement in  $z$  direction. Here, from equation (2.8), there are six strains and three displacements and six strain-displacement equations. When the number of unknown components is more than the number of equations, we need a set of additional equations to solve the unknowns. The additional equations are known as the compatibility equations. By taking partial derivatives of the strain components in equations (2.8), they lead to

$$\begin{aligned} \frac{\partial^2 \varepsilon_{xy}}{\partial x \partial y} &= \frac{1}{2} \left( \frac{\partial^2 \varepsilon_{xx}}{\partial y^2} + \frac{\partial^2 \varepsilon_{yy}}{\partial x^2} \right) \\ \frac{\partial^2 \varepsilon_{yz}}{\partial y \partial z} &= \frac{1}{2} \left( \frac{\partial^2 \varepsilon_{yy}}{\partial z^2} + \frac{\partial^2 \varepsilon_{zz}}{\partial y^2} \right) \\ \frac{\partial^2 \varepsilon_{zx}}{\partial z \partial x} &= \frac{1}{2} \left( \frac{\partial^2 \varepsilon_{zz}}{\partial x^2} + \frac{\partial^2 \varepsilon_{xx}}{\partial z^2} \right) \\ \frac{\partial^2 \varepsilon_{xx}}{\partial y \partial z} &= \frac{\partial}{\partial x} \left( -\frac{\partial \varepsilon_{yz}}{\partial x} + \frac{\partial \varepsilon_{zx}}{\partial y} + \frac{\partial \varepsilon_{xy}}{\partial z} \right) \\ \frac{\partial^2 \varepsilon_{yy}}{\partial z \partial x} &= \frac{\partial}{\partial y} \left( \frac{\partial \varepsilon_{yz}}{\partial x} - \frac{\partial \varepsilon_{zx}}{\partial y} + \frac{\partial \varepsilon_{xy}}{\partial z} \right) \\ \frac{\partial^2 \varepsilon_{zz}}{\partial x \partial y} &= \frac{\partial}{\partial z} \left( \frac{\partial \varepsilon_{yz}}{\partial x} + \frac{\partial \varepsilon_{zx}}{\partial y} - \frac{\partial \varepsilon_{xy}}{\partial z} \right) \end{aligned} \quad (2.9)$$

The compatibility equations were first derived by Saint Venant in 1860 (Muskhelishvili *et al.*, 1953), which are necessary and sufficient in solving displacement and strain relations in elasticity.

Above, we have introduced governing equations describing stress-force relations (equation (2.6)) and strain-displacement relations (equations (2.8) and (2.9)). Here, another set of equations is to describe the stress-strain relationship in linear elasticity, which is called the constitutive equation. The fundamental assumption of the constitutive equation is that stress components are linear functions of strain components. The stress-strain law of isotropic elasticity is usually called 'Hooke's law':

$$\begin{aligned}
 \varepsilon_{xx} &= \frac{1}{E} [\sigma_{xx} - \nu(\sigma_{yy} + \sigma_{zz})] \\
 \varepsilon_{yy} &= \frac{1}{E} [\sigma_{yy} - \nu(\sigma_{xx} + \sigma_{zz})] \\
 \varepsilon_{zz} &= \frac{1}{E} [\sigma_{zz} - \nu(\sigma_{xx} + \sigma_{yy})] \\
 \varepsilon_{xy} &= \frac{1}{2G} \tau_{xy} \\
 \varepsilon_{xz} &= \frac{1}{2G} \tau_{xz} \\
 \varepsilon_{yz} &= \frac{1}{2G} \tau_{yz}
 \end{aligned} \tag{2.10}$$

Where Young's modulus  $E$  (Pa) is the ratio of stress to the strain that results in the same direction. Poisson's ratio,  $\nu$ , is defined as the ratio of the horizontal strain to the vertical strain when the body or element is under conditions of vertical uniaxial stress.  $G$  is shear modulus (Pa) and its value equals  $E/[2(1 + \nu)]$ .

If we combine the stress equilibrium equations (equation (2.6)), the strain– stress equations (equations (2.10)), and then strain-displacement equations (equation (2.8)), we find

$$\begin{aligned}
& \lambda \left( \frac{\partial^2 u}{\partial x^2} + \frac{\partial^2 v}{\partial x \partial y} + \frac{\partial^2 w}{\partial x \partial z} \right) + G \left( \frac{\partial^2 u}{\partial x^2} + \frac{\partial^2 v}{\partial x \partial y} + \frac{\partial^2 w}{\partial x \partial z} \right. \\
& \quad \left. + \frac{\partial^2 u}{\partial x^2} + \frac{\partial^2 u}{\partial y^2} + \frac{\partial^2 u}{\partial z^2} \right) + \rho F_x = 0 \\
& \lambda \left( \frac{\partial^2 u}{\partial x \partial y} + \frac{\partial^2 v}{\partial y^2} + \frac{\partial^2 w}{\partial y \partial z} \right) + G \left( \frac{\partial^2 u}{\partial x \partial y} + \frac{\partial^2 v}{\partial y^2} + \frac{\partial^2 w}{\partial y \partial z} \right. \\
& \quad \left. + \frac{\partial^2 v}{\partial x^2} + \frac{\partial^2 v}{\partial y^2} + \frac{\partial^2 v}{\partial z^2} \right) + \rho F_y = 0 \\
& \lambda \left( \frac{\partial^2 u}{\partial z \partial x} + \frac{\partial^2 v}{\partial z \partial y} + \frac{\partial^2 w}{\partial z^2} \right) + G \left( \frac{\partial^2 u}{\partial z \partial x} + \frac{\partial^2 v}{\partial z \partial y} + \frac{\partial^2 w}{\partial z^2} \right. \\
& \quad \left. + \frac{\partial^2 w}{\partial x^2} + \frac{\partial^2 w}{\partial y^2} + \frac{\partial^2 w}{\partial z^2} \right) + \rho F_z = 0
\end{aligned} \tag{2.11}$$

Equations (2.11) are called Navier equations (Constantin and Foias, 2020). It integrates the equations of stress equilibrium, strain-displacement equations and constitutive equations, expressing all these components in terms of displacements. The displacement-based equations provide an alternative solution to the stress- or strain-based equations in elasticity discussed above in this section.

In engineering problems, it is difficult to get the exact response or solution (stresses or displacements, etc.) of a complicated model with a complex geometrical shape, specified loading and boundary conditions. To solve the mechanical equilibrium in the fluid-injection model, we use the finite element method (FEM) to find an approximate solution. The basic idea of FEM is to replace the complex problem with a simpler one (Rao, 2017). The model domain is considered to be composed of many tiny interconnected subdomains, which are called elements. The elements are connected to each other at the nodes. A node is simply a point in space, and the field variables are calculated at every node from the governing equation. Once the model is divided into discrete elements (discretization), a proper polynomial interpolation or displacement model is selected to give each element an approximate solution. From the displacement model, the stiffness and load vector of the element is derived. Then the element stiffness and load vectors are assembled to obtain the overall equilibrium equations. The problem of mechanical equilibrium (equations (2.11)) thus reduces to a set of algebraic equations, where unknowns are the three

components of the displacement at each node. Afterward, boundary conditions are used to modify the overall equilibrium equation to solve the unknown nodal displacements. Last, element strain and stress are computed from the nodal displacements.

In order to perform the FE analysis, we made use of the ABAQUS software (Abaqus *et al.*, 2019). During the FE analysis in Abaqus, the assemblage was required to satisfy three basic conditions: (a) equilibrium of the element forces with the external loads, (b) strain-displacement relationship of the deformed elements so that continuity is maintained at the joints, and (c) force-deformation relationships in the elements that depend on the element properties (Clough, 1990). These equations were implicitly solved by the Abaqus standard solver to obtain the displacement degrees of freedom for every node in the model under static conditions. Abaqus/Standard uses the Newton-Raphson method to solve the algebraic equations transformed from the set of governing equations to obtain solutions for nonlinear problems.

### 2.2.2 Friction mechanics of rock

In this section, the basic frictional properties in the weak plane of the rock will be discussed. Then, we will introduce the slip-weakening frictional law applied in the numerical model in this thesis.

Friction is the tangential shearing force that resists the relative movement of the contact between two solid surfaces. Assume that two faces in contact are pressed by a normal force  $N$ , and a shearing force is applied in parallel with the contact surface. The frictional force  $F_f$  resisting the contact movement can be dependent on the normal force and written as

$$F_f = \mu N \quad (2.12)$$

where  $\mu$  is the friction coefficient. When the shearing force reaches some critical value of friction, the surface begins to slide. Dividing the equation (2.12) by the surface area  $A$ , we get:

$$\tau = \mu \sigma \quad (2.13)$$

where  $\tau$  is the shear stress along the contact surface direction and  $\sigma$  is the normal stress on the sliding plane. Equation (2.13) is called Amonton's law, first proposed in 1699 (Dowson, 1978).

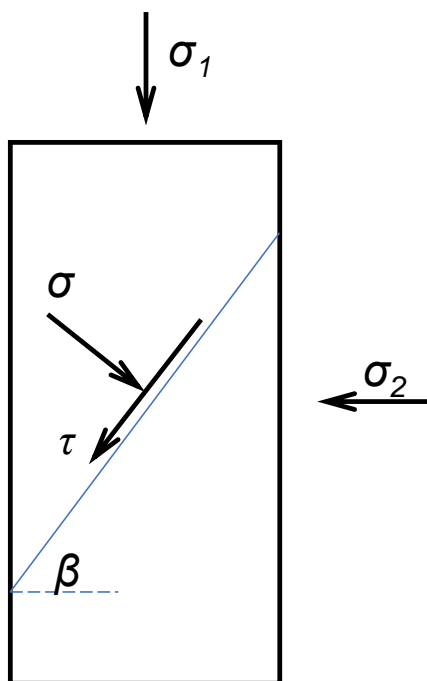


Figure 2.3: Schematic model of rock sample with the plane of weakness with outward normal vector oriented at angle  $\beta$  to the direction of maximum principal stress.

In our injection model, the rock sample is with a pre-existing fault. So we are discussing the friction on the rock with a pre-existing plane. The friction equation will be explained in a simplified model in two dimensions with a saw-cut fracture through the sample and under two stresses acting vertically as shown in Fig. 2.3. The normal vector of the plane of weakness makes an angle  $\beta$  with the direction of the maximum principal stress  $\sigma_1$ . According to equation (2.13) and Coulomb (1773), the fundamental frictional failure criterion of the weak plane is assumed to be

$$|\tau| = S_0 + \mu\sigma \quad (2.14)$$

where  $S_0$  is the cohesion of the surface,  $\sigma$  and  $\tau$  are normal and shear component along the pre-existing fault. The slippage will not occur until the failure criterion is reached (Barton, 1976; Byerlee, 1968; Byerlee, 1978; Jaeger *et al.*, 2009). Equation (2.14) origin from Coulomb and is usually used as a standard criterion for estimating

fault reactivation. Based on equation (2.14), Byerlee (1978) did friction experiments on rocks and concluded the shear and normal stress relationship through a large amount of rock brittle failure experiments and obtained:

$$\tau = \begin{cases} 0.85\sigma_n & : \sigma_n \leq 200MPa \\ 50 + 0.6\sigma_n & : \sigma_n > 200MPa \end{cases} \quad (2.15)$$

which is referred to as Byerlee's law (Fig. 2.4).

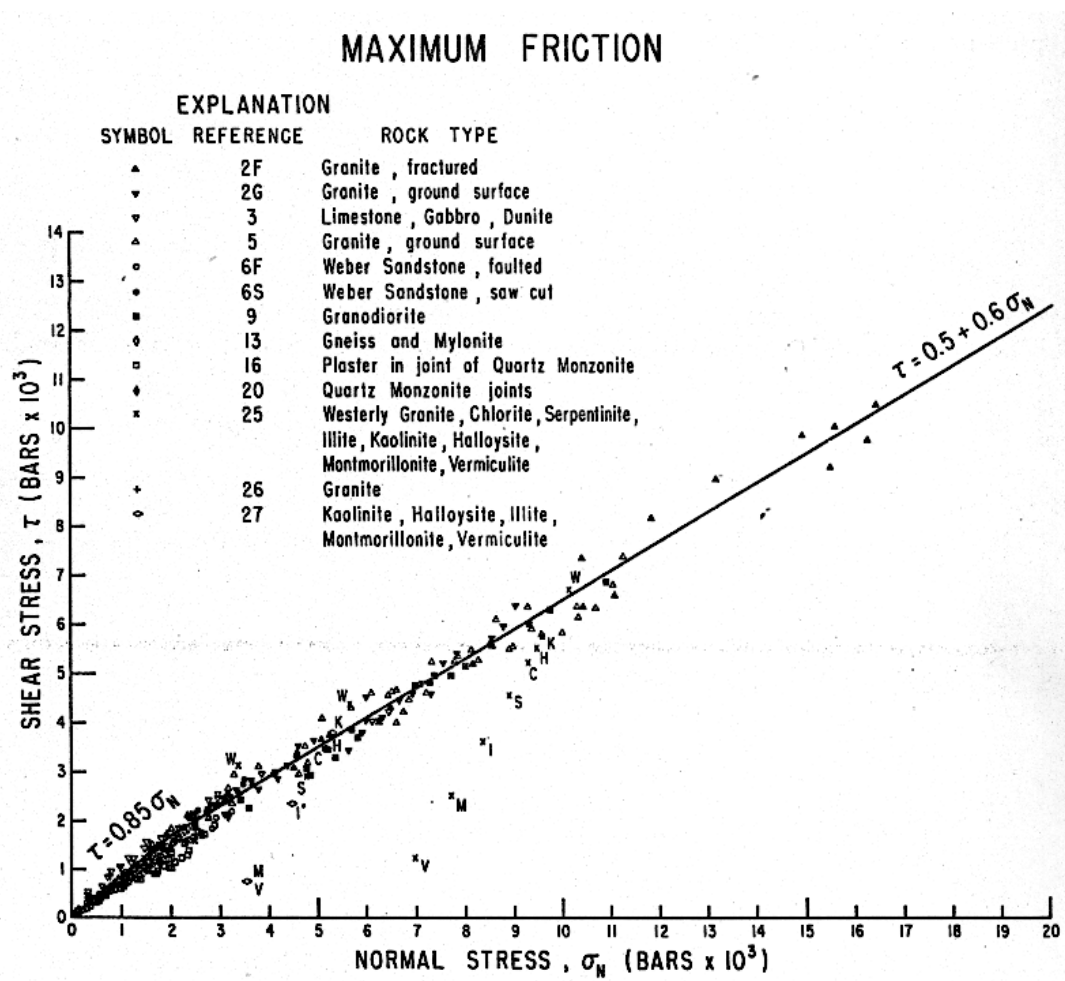


Figure 2.4: Shear stress plotted as a function of normal stress at the maximum friction for a variety of rock types at normal stresses to 20 kb. (Byerlee, 1978)

In equation (2.14),  $\sigma$  and  $\tau$  are given by

$$\begin{aligned}\sigma &= \frac{1}{2}(\sigma_1 + \sigma_2) + \frac{1}{2}(\sigma_1 - \sigma_2)\cos 2\beta \\ \tau &= -\frac{1}{2}(\sigma_1 - \sigma_2)\sin 2\beta\end{aligned}\quad (2.16)$$

where  $\sigma_1$  is the maximum principal stress and  $\sigma_2$  is the minimum principal stress. In the numerical simulation, the loading of the sample ( $\sigma_1$ ) is calculated from the experiment results in Fig. 2.1 B and equation (2.16).

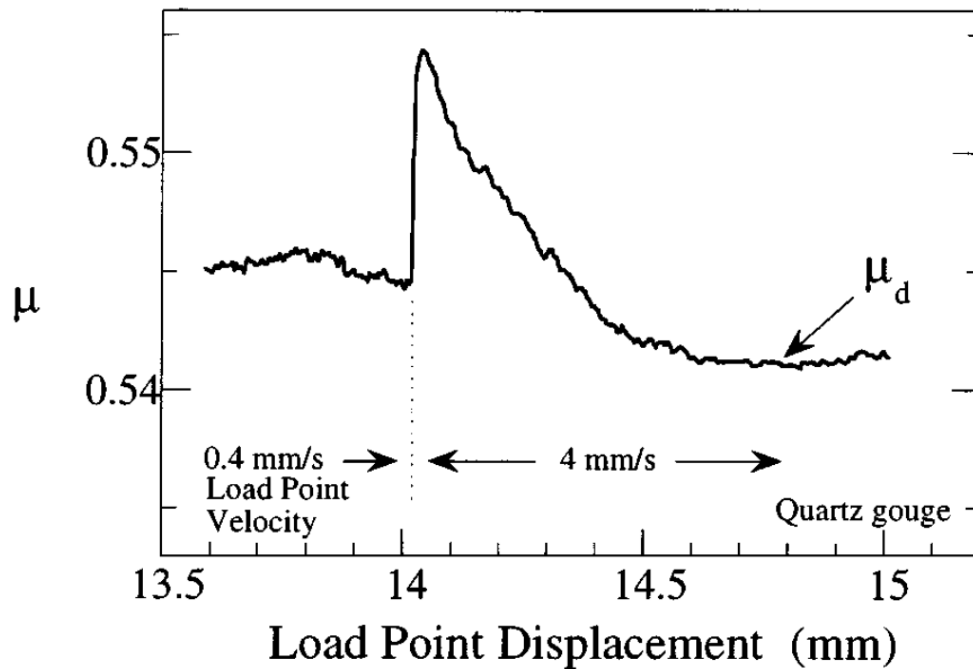


Figure 2.5: Experiment data showing friction affected by slip state. (Marone, 1998)

The fault's frictional properties are known to be slip rate or distance dependent (for example, the experimental measurement shown in Fig. 2.5) (Marone *et al.*, 1991; Scholz, 1988). Triaxial compression rock failure experiments in the laboratory indicate that the strength of intact granite or carbonate rocks declines linearly with slip (Wawersik and Brace, 1971; Wawersik and Fairhurst, 1970; Wong, 1982). In the in-situ injection experiment by Guglielmi *et al.* (2015b), seismicity was measured outside the pressurized zone due to the rate-weakening behavior of the asperities. By examining the slip history data at the injection hole from the fluid injection experiment (Guglielmi *et al.*, 2015b), Bhattacharya and Viesca (2019) used a nu-

numerical model with a slip-weakening friction coefficient to fit the slip acceleration result of the in situ experiment. Here, a user-defined friction law dependent on the displacement (Palmer and Rice, 1973; Scholz, 1988) of the fault is applied by the FRIC subroutine in Abaqus to simulate the contact problem of the fault zone. The linearly weakening friction coefficient dependent on displacement is as follows

$$\mu = \begin{cases} \frac{\mu_d - \mu_s}{D_c} \xi + \mu_s, & (\xi < D_c) \\ \mu_d, & (\xi \geq D_c) \end{cases} \quad (2.17)$$

where  $\mu_s$  is the static friction coefficient, whose value is determined from equation (2.14), (2.16), and stress results from the experiment (Fig. 2.1 B) to be 0.578,  $\mu_d$  is the dynamic friction coefficient,  $\xi$  is the relative displacement along the fault. After reaching the sliding threshold  $D_c$ , the friction coefficient remains constant.

### 2.2.3 Fluid diffusion and permeability

In this subsection, we are going to introduce the fluid diffusion equation, which governs the pore pressure distribution on fault in our numerical model. The fluid diffusion equation is derived from the conservation of mass for the pore fluid and Darcy's law. Per unit volume, the total of all masses in and out per unit time must equal the change of mass due to change in density per unit time (Childs, 2010). It is suggested from the principle of conservation of mass that the mass of a region will conserve on a local quantity without mass sources and sinks. The differential form of the mass conservation equation (the continuity equation) (Jaeger *et al.*, 2009) is given by

$$\frac{\partial \rho}{\partial t} + \nabla \cdot (\rho \mathbf{v}) = 0 \quad (2.18)$$

where  $\rho$  is the density of fluid flow,  $\nabla = (\frac{\partial}{\partial x}, \frac{\partial}{\partial y}, \frac{\partial}{\partial z})$  is the gradient operator, the vector  $\mathbf{v} = \mathbf{v}(x, y, z, t)$  is the fluid velocity as a function of space of time. Combining equation (2.18) with Fick's first law which explained the refashion between flux and density [equation (2.19) (Fick, 1855)]:

$$\rho \mathbf{v} = -D \nabla \rho \quad (2.19)$$

where  $D$  is hydraulic diffusivity, and considering the relation for static pressure, we get:

$$\frac{\partial p(x, y, t)}{\partial t} = D \nabla^2 p(x, y, t) \quad (2.20)$$

Equation (2.20) is the spatio-temporal fluid diffusion equation along the fault, where  $p(x, y, t)$  is evolving fluid pressure along the fault plane at time  $t$ ,  $D$  is hydraulic

diffusivity (Jaeger *et al.*, 2009). This equation governs the fluid pressure along the fault. In our model, the equation (2.20) is solved by an explicit finite difference method proposed by Almakari (2019b). The hydraulic diffusivity  $D$  is given by

$$D = \frac{k}{\phi\mu C_f} \quad (2.21)$$

where  $k$  is permeability,  $\phi$  is porosity,  $\mu$  is the viscosity and  $C_f$  is the compressibility of the pore fluid whose value is  $4.6 \cdot 10^{-10} \text{ Pa}^{-1}$ . In this thesis, we use different values of hydraulic diffusivity, ranging between  $\sim 10^{-5}$  to  $\sim 10^{-6} \text{ m}^2/\text{s}$  according to the discussion in section 1.1.5.

In our numerical finite element model, the fluid pressure distribution is coupled with the mechanical problem. The spatio-temporal results of equation (2.20) are solved with the increasing pore pressure at the injection point and then applied to the fault plane. The diffusive pore pressure functions as a boundary condition in the elastic mechanical model.

## 2.3 Mechanical problem

### 2.3.1 Geometry and element mesh

Table 2.1: Mechanical properties of the finite element model

Properties	Values
Young's modulus	35 GPa
Density	2.8 g/cm <sup>3</sup>
Poisson ratio	0.27
Element type	3D stress C3D8

In this section, the 3D finite element rock sample with the pre-existing fault is established using the Abaqus software to simulate the fluid-triggered fault reactivation. The studied specimen is a cylindrical rock 40 mm in width and 100 mm in height, which is cut into two separated halves by a thorough crack with an angle of 60 degrees from the horizontal to simulate the pre-existing fault. Afterward, we mesh the specimen by setting the distance of the nodes in the model as 2 mm from each other. The FE mesh contains 26400 nodes and 23522 8-node elements, whose

type is 3D stress C3D8 (8-node linear brick). After meshing the whole sample, we assign the model with the mechanical properties listed in Table 2.1. In the following subsection, we will describe the model's loading process.

### 2.3.2 Loading progress

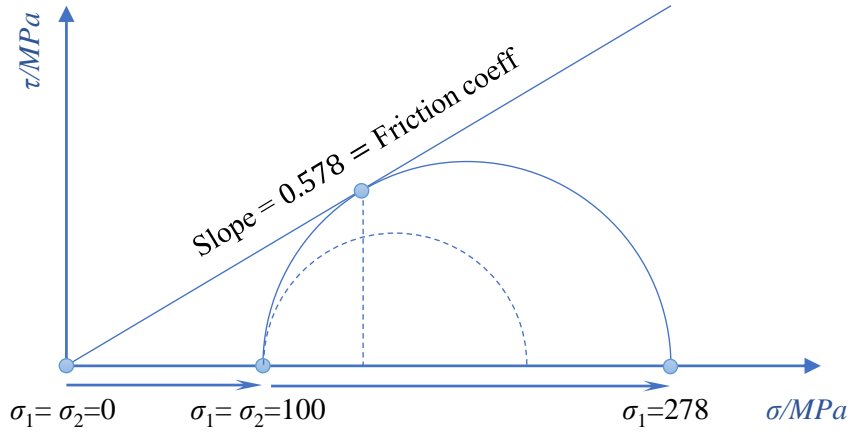


Figure 2.6: Mohr-Coulomb diagram and loading process of the experiment with 100 MPa confining pressure. When  $\sigma_1$  reaches 278 MPa, the fault begins to slip. The static friction coefficient of 0.578 is estimated from this onset point.

The stress state of the rock sample is calculated by the Mohr-Coulomb criterion (equation (2.14)). Based on the known peak shear stress  $\tau = 78$  MPa, constant confining pressure  $\sigma_2 = 100$  MPa and initial fluid pressure 10 MPa from Fig. 2.1 (B) (Passelègue *et al.*, 2018), the normal stress  $\sigma$  is calculated from the experiment data and equation (2.16). Then the peak axial stress  $\sigma_1$  is solved from  $\tau$ ,  $\sigma_2$  and  $\sigma$ , where  $\sigma_1 = 278$  MPa. The Mohr-Coulomb diagram and loading process are shown in Fig. 2.6. The loading process of our numerical model includes the following phases:

- (1)  $\sigma_1$  and  $\sigma_2$  increase from 0 to 100 MPa.
- (2) The confining pressure  $\sigma_2 = \sigma_3$  maintains constant at 100 MPa and  $\sigma_1$  increases from 100 to 278 MPa. The onset of the fault occurs when  $\sigma_1$  reaches 278 MPa.

- (3)  $\sigma_1$  reduces to make shear stress of the fault  $\tau = 90\% \cdot \tau_p$ . Then the fluid pressure at the borehole begins to increase from 10 MPa to 90 MPa at a certain injection rate.

In our numerical model, the loading conditions are consistent with the experiment described above. The loading curve is shown in Fig. 2.1 B. Before the pressure and injection loading are applied, we display the Stress Field Editor in Abaqus to make sure the initial stress field is the same as the experiment. In the initial step, we set  $\sigma_x = \sigma_y = 100$  MPa in the predefined stress field, here  $\sigma_x$  and  $\sigma_y$  are stress in  $x$  and  $y$  direction. This initial stress field setting is to make sure the numerical model converges during the loading process. After setting the initial stress field, the axial loading pressure acting on the top of the sample and the confining pressure around the rock cylinder increase from 0 to 100 MPa equally.

Once the surrounding pressure reaches 100 MPa, which is equivalent to the experiment,  $\sigma_2$  keeps constant and the axial loading continues to increase. The increasing shear stress is realized by applying an axial pressure on the top of the specimen. The pressure varies at this step from 0 MPa to 278 MPa to ensure the shear stress peak reaches  $\tau_p = 78$  MPa. After shear stress reaches its peak, we decrease the axial loading to make shear stress equal to 90% of  $\tau_p$ . Fluid pressure is realized by applying a 10 MPa pressure along the fault plane. After shear stress decreases to 90%, an increasing diffusive fluid pressure is injected from a borehole on the fault 4.5 mm from the edge at a constant rate up to 90 MPa.

### 2.3.3 Boundary conditions

Boundary conditions of the model domain are as follows:

Top: traction free,  $p = 0 \rightarrow 279$  MPa

Bottom:  $v = 0$  mm,  $p = 0$  MPa, middle point of bottom line: fixed

Surrounding boundary:  $u = 0$  mm,  $p = 100$  MPa

where  $u$  and  $v$  are horizontal and vertical displacements, respectively, and  $p$  is pressure. Fig. 2.7 gives a schematic view of the boundary conditions of the finite element model.

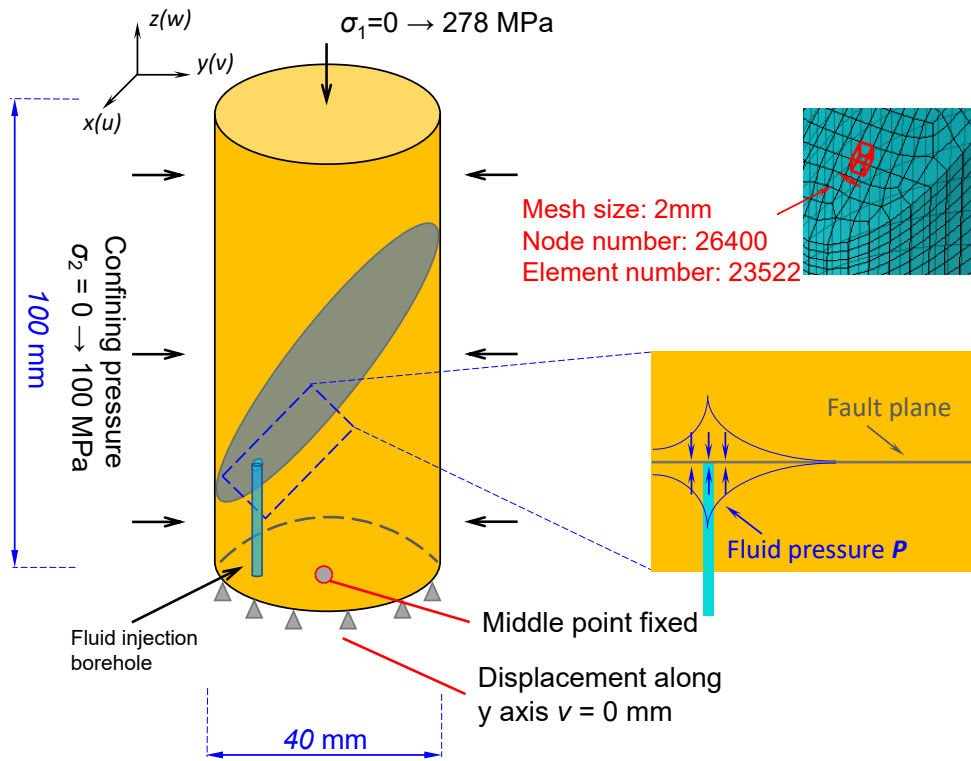


Figure 2.7: Boundary conditions of the mechanical model.

## 2.4 Solving fluid diffusion equation

### 2.4.1 Constant permeability/diffusivity

In this study, we use a solver proposed by Almakari *et al.* (2020) and Almakari (2019a,b) to estimate the fluid pressure diffusion on the fault plane. The solver gives a solution to the diffusion equation (2.20). They used the Forward Time Central Space (FTCS) explicit finite difference approach to solve the diffusion equation. At first, the boundary condition of the diffusive fault is that no liquid is allowed to flow outside the fault plane, the flow at the boundaries of the fault is 0. On the other hand, the source of the diffusive fault is the controlled pressure at the injection hole. The fault eclipse (long axis 0.04 m, short axis 0.02 m) is discretized into a group of equal computational cells of size  $\Delta x \cdot \Delta y$ . Here  $\Delta x = \Delta y = 0.0025$  m.  $p_{i,j}^k$  denotes the mesh function that approximates  $p(x_i, y_j, t_k)$ , where  $i$  and  $j$  are node numbers

and  $k$  is the time step number. The diffusion equation (2.20) can be written as

$$\frac{p_{i,j}^{k+1} - p_{i,j}^k}{\Delta t} = D \left( \frac{p_{i-1,j}^k - 2p_{i,j}^k + p_{i+1,j}^k}{\Delta x^2} + \frac{p_{i,j-1}^k - 2p_{i,j}^k + p_{i,j+1}^k}{\Delta y^2} \right) \quad (2.22)$$

If  $\Delta x = \Delta y = h$  ( $h$  is the node spacing in  $x$  and  $y$  directions), equation (2.22) can be written as

$$p_{i,j}^{k+1} = \left(1 - \frac{4\Delta t D}{h^2}\right) p_{i,j}^k + \Delta t D \left( \frac{p_{i,j-1}^k + p_{i-1,j}^k + p_{i+1,j}^k + p_{i,j+1}^k}{h^2} \right) \quad (2.23)$$

The time step  $\Delta t$  in the finite difference method should satisfy the condition to make the numerical model stable:

$$\Delta t \leq \frac{h^2}{4D} \quad (2.24)$$

where  $D$  is hydraulic diffusivity, and in Chapter 4 we first chose constant values of  $D = 5 \cdot 10^{-6}$ ,  $1 \cdot 10^{-5}$ ,  $5 \cdot 10^{-5}$  m<sup>2</sup>/s to do parameter study. Equation (2.24) is the stability condition and the time step is satisfied at each iteration.

## 2.4.2 Non-constant permeability/diffusivity

In this paragraph, we will discuss the hydraulic permeability/diffusivity enhancement according to a number of experimental studies. On the one hand, hydraulic permeability/diffusivity is influenced by the change of effective stress in the fault system. As we know, the normal stress along the fault decreases with fluid injection pressure (Rutter and Mecklenburgh, 2018). In this case, the permeability enhancement might happen due to the normal effective stress drop. Zoback and Byerlee (1975) observed permeability changes with stress changes based on laboratory experiments on rock samples. Another laboratory permeability test shows that the fracture permeability is more affected by pore pressure change than by confining pressure (Ghabezloo *et al.*, 2009). On the other hand, during fault reactivation, the permeability was observed to evolve following the slip accumulation (Baghbanan and Jing, 2008; Zhang and Tullis, 1998) during seismicity and shear displacement in laboratory scale tests (Chen *et al.*, 2000; Gutierrez *et al.*, 2000).



## Chapter 3

# Numerical model configuration and calibration

Résumé . . . . .	62
Summary . . . . .	62
3.1 Theoretical benchmark for numerical/ hydro-mechanical model .	62
3.1.1 Geometry and model properties . . . . .	62
3.1.2 Loading and boundary conditions . . . . .	63
3.1.3 Numerical results comparison . . . . .	68
3.2 Experimental calibration for numerical/hydro-mechanical model .	69
3.2.1 Experiment assembling . . . . .	70
3.2.2 Parametric study of material property . . . . .	73
3.2.3 Nucleation length and fault stability . . . . .	76
3.2.4 Result comparison . . . . .	77
3.3 Conclusion . . . . .	78

## Résumé

Dans ce chapitre, le modèle numérique est testé par rapport à une référence théorique et à des résultats expérimentaux. Tout d'abord, les résultats numériques obtenus par la méthode des éléments finis sont comparés à une solution analytique proposée par Viesca (2021). Dans une deuxième étape, le modèle est calibré à partir de mesures expérimentales. Pour cela, nous estimons d'abord la rigidité effective de l'ensemble du système de chargement de l'expérience d'injection en laboratoire, selon Passelègue *et al.* (2018), y compris la colonne de chargement et l'échantillon de roche. Ensuite, une étude paramétrique basée sur les propriétés des matériaux est réalisée. Différentes rigidités effectives de l'échantillon de roche sont simulées et comparées aux résultats expérimentaux. En couplant l'équation de diffusion des fluides et la loi de friction de glissement-fragilisation, cette étape de calibration garantit que notre modèle numérique est cohérent à la fois avec la théorie et les observations expérimentales.

## Summary

In this chapter, the numerical model is tested against a theoretical benchmark and experimental results. First, the numerical results of the finite element method are compared with a closed-form solution by Viesca (2021). In the second step, the model is calibrated with experimental measurements. To do that, we first estimate the effective stiffness of the whole loading system of the indoor injection experiment by Passelègue *et al.* (2018), including the loading column and rock sample. Afterward, a parametric study based on the material property is carried out. The different effective stiffness of the rock sample is simulated to compare with the experiment results. Coupling with the fluid diffusion equation and slip-weakening friction law, this calibration step ensures that our numerical model is consistent with both theory and experimental observations.

## 3.1 Theoretical benchmark for numerical/ hydro-mechanical model

### 3.1.1 Geometry and model properties

In recent years, there has been growing interest in understanding the behavior of fault slip in response to fluid injection, as this can have important implications for a

range of engineering and geophysical applications. Viesca (2021) has proposed a self-similar solution to a problem of fault slip in response to fluid injection (Fig 3.1) that has important implications for our understanding of fault mechanics. Specifically, the model considers a 1D fault plane lying on  $y = 0$  in a 2D elastic medium and a line fluid source of constant pressure at  $x = 0$  along the  $z$ -axis. The medium containing the fault is linearly elastic, and the deformation may be in-plane or anti-plane. The shear modulus of the medium is  $G$ , and the Poisson ratio  $\nu$ . The effective elastic modulus is defined as  $G' = G/[2(1 - \nu)]$  for the in-plane (mode-II) case and  $G' = G/2$  for the anti-plane (mode-III) case. The friction on the interface is given by a constant friction coefficient  $\mu$ .

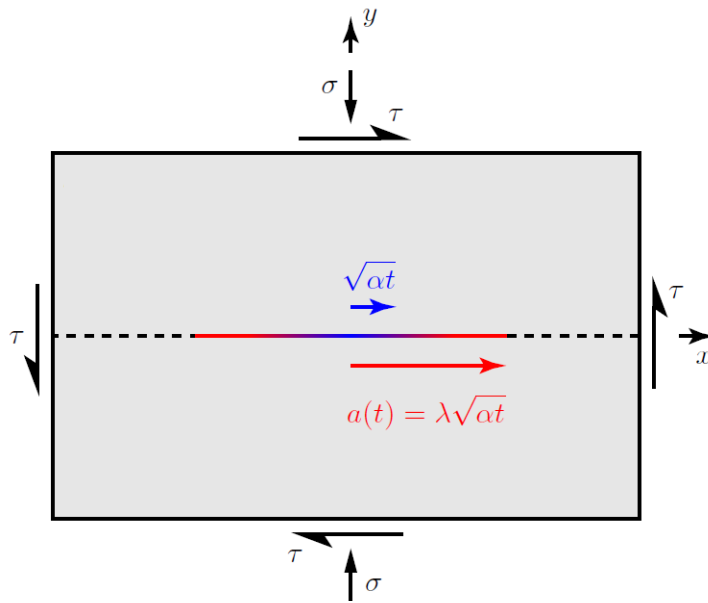


Figure 3.1: Brief geometry of the 2D self-similar isotropic elastic model loaded with normal stress  $\sigma$  and shear stress  $\tau$ . The model has a 1D fault with fluid injected at  $x = 0$ . The diffusive front of fluid is  $\sqrt{\alpha t}$ , where  $\alpha = 4\alpha_{hy}$  is a nominal constant hydraulic diffusivity. No leak-off of fluid is allowed in the model. The slip front  $a(t) = \lambda\sqrt{\alpha t}$ , where  $t$  is the time since the fluid injection and  $\lambda$  is the rupture growth factor.(Viesca, 2021)

### 3.1.2 Loading and boundary conditions

Viesca (2021) denotes the initial (pre-injection) fault shear stress  $\tau$  (in-plane or anti-plane), the fault friction coefficient  $\mu$ , the initial pore fluid pressure on interface  $p_0$ , the initial total fault-normal compressive stress  $\sigma$ , and the initial effective normal

stress  $\sigma' = \sigma - p_0$ . The initial fault strength is  $\tau_p = \mu\sigma'$ . This problem was presented in Bhattacharya and Viesca (2019) and Viesca (2021) and is a simpler version of one considered by Garagash and Germanovich (2012), who examined the response to injection of a fault whose friction coefficient weakens with slip.

In this model, the one-dimensional diffusion of pore fluid pressure along the fault is governed by:

$$p_t = \alpha_{hy} p_{xx} \quad (3.1)$$

where  $\alpha_{hy}$  is the hydraulic diffusivity value of fluid along the fault plane and where the pore pressure evolution is subject to the initial pressure state and injection at constant pressure  $\Delta p$  at  $x = 0$ ,

$$p(x, 0) = p_0, p(0, t > 0) = \Delta p \quad (3.2)$$

The solution to this problem is given by the following pore pressure distribution:

$$p(x, t) = p_0 + \Delta p \cdot \text{erfc}(x/\sqrt{\alpha t}) \quad (3.3)$$

where a nominal hydraulic diffusivity is adopted

$$\alpha = 4\alpha_{hy} \quad (3.4)$$

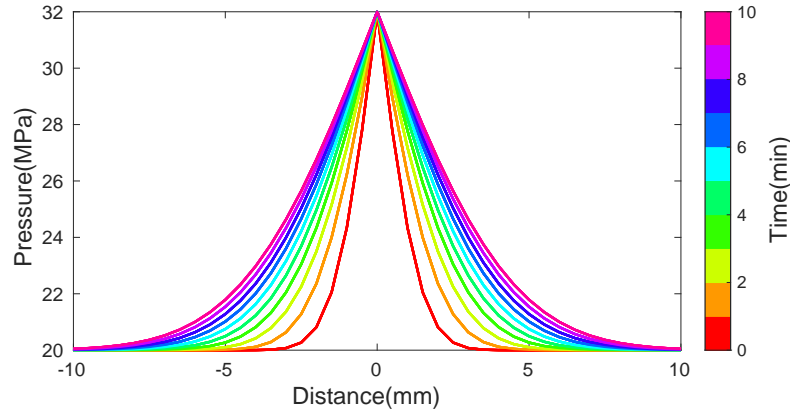


Figure 3.2: Fluid pressure diffusion along  $x$ -axis. Pressure evolution is plotted every minute, which is the solution to equation (3.3)

For hydraulic properties:  $p_0 = 20$  MPa,  $\Delta p = 12$  MPa,  $\alpha_{hy} = 0.01$  m<sup>2</sup>/s. The detailed fluid pressure diffusion history along the fault plane is plotted in Fig. 3.2.

The governing equation of the frictional contact of the fault obeys a Coulomb friction law: the slip doesn't occur until the shear stress  $\tau$  reaches a critical value  $\tau_s$ , which is the static friction coefficient times the effective normal stress. We have

$$\tau_s = \mu[\sigma - p(x, t)] \quad (3.5)$$

where  $\mu$  is the constant friction coefficient. Where sliding occurs, this strength must equal the shear stress on the fault.

Above we have provided the expression of pore pressure. We are giving the closed-form solution for fault slip in the following. Due to Rice *et al.* (1968), the shear stress  $\tau_s$  comprises quasi-static changes arising from a slip distribution  $\delta$  and the initial shear stress  $\tau$ . Thus, the stress-slip relation can be written as:

$$\tau_s(x, t) = \tau + \frac{G'}{\pi} \int_{-a(t)}^{a(t)} \frac{\partial \delta(s, t) / \partial s}{s - x} ds \quad (3.6)$$

where  $a(t)$  is crack length and  $x = a(t) = \lambda \sqrt{at}$  is the fracture front location. Since  $\sqrt{at}$  is the fluid pressure propagation front (Shapiro *et al.*, 2006a; Shapiro *et al.*, 1997), here  $\lambda$  is the rupture growth factor, determining if the crack front lags ( $\lambda < 1$ ) or outpaces ( $\lambda > 1$ ) the fluid pressure front.

From equation (3.3), (3.5) and (3.6), we can derive the non-dimensionalized equation:

$$\left(1 - \frac{\tau}{\tau_p}\right) \frac{\sigma'}{\Delta p} - \operatorname{erfc} |\lambda \bar{x}| = -\frac{1}{\pi} \int_{-1}^1 \frac{d\bar{\delta}/d\bar{s}}{\bar{x} - \bar{s}} d\bar{s} \quad (3.7)$$

where  $\left(1 - \frac{\tau}{\tau_p}\right) \frac{\sigma'}{\Delta p}$  is a sole parameter which is bound between 0 and 1. The sole parameter reflects the initial state of stress of the fault. The upper bound represents a marginally pressurized fault and the lower bound denotes a critically stressed fault where initial shear stress  $\tau = \tau_p$ .  $x = a(t)\bar{x}$  is the similarity coordinate, and  $\delta(x, t) = \bar{\delta}[x/a(t)]a(t)\mu\Delta p/G'$ . The solution to be solved is the slip distribution  $\bar{\delta}$  and the rupture propagation factor  $\lambda$ , along with their dependence on the sole parameter  $\left(1 - \frac{\tau}{\tau_p}\right) \frac{\sigma'}{\Delta p}$ .

The solution of  $\lambda$  is determined from a boundary condition that the crack-tip stress intensity factors of the rupture must be zero (Viesca, 2021), which writes:

$$\left(1 - \frac{\tau}{\tau_p}\right) \frac{\sigma'}{\Delta p} = \frac{1}{\pi} \int_{-1}^1 \frac{\operatorname{erfc} |\lambda x|}{\sqrt{1 - x^2}} dx \quad (3.8)$$

where  $\lambda$  is implicitly solved with its dependence on the sole parameter. The integrand on the right hand of equation (3.8) can be estimated by Gauss-Chebyshev quadrature (Viesca, 2021; Viesca and Garagash, 2018). In the following paragraph, we are going to present the asymptotic approximation of the integral of  $\lambda$  when the fault is under different initial stress conditions.

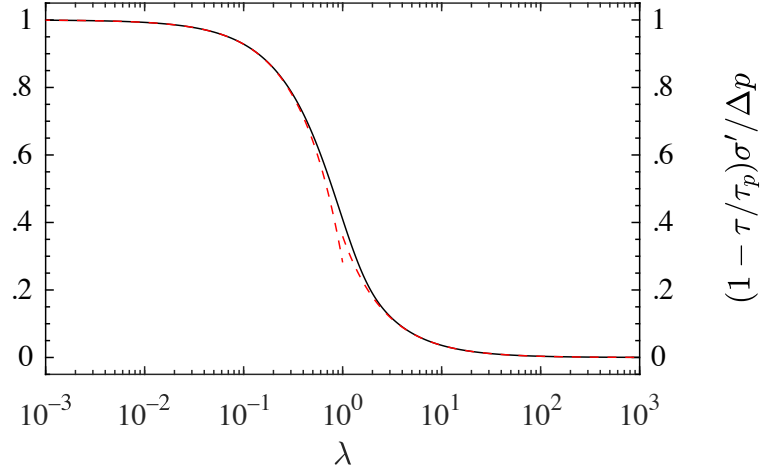


Figure 3.3: Relation between the crack growth factor  $\lambda$  and initial stress parameter (black line). Red dashed lines are approximations in equation (3.9) and (3.10). (Viesca, 2021)

Since the sole parameter boundary, the relationship between  $\lambda$  and the sole parameter and the solution of the slip distribution will be discussed in two situations:

**(i) Marginally pressurized faults**

In this limit,  $\tau \rightarrow \mu(\sigma' - \Delta p)$  and  $\left(1 - \frac{\tau}{\tau_p}\right) \frac{\sigma'}{\Delta p} \rightarrow 1$ . The rupture lags the fluid pressure diffusion ( $\lambda < 1$ ). The relation between the crack growth factor and the initial stress parameter follows:

$$\left(1 - \frac{\tau}{\tau_p}\right) \frac{\sigma'}{\Delta p} \approx 1 - \frac{4}{\pi^{3/2}} \lambda - O(\lambda^3) \quad (3.9)$$

**(ii) Critically stressed faults**

In this limit,  $\tau \rightarrow \tau_p$  and  $\left(1 - \frac{\tau}{\tau_p}\right) \frac{\sigma'}{\Delta p} \rightarrow 0$ . The rupture outpaces the fluid pressure diffusion ( $\lambda > 1$ ). The relation between the crack growth factor  $\lambda$  and the initial stress parameter becomes:

$$\left(1 - \frac{\tau}{\tau_p}\right) \frac{\sigma'}{\Delta p} \approx 1 - \frac{2}{\pi^{3/2}} \frac{1}{\lambda} O(\lambda^{-3}) \quad (3.10)$$

The relation between factor  $\lambda$  and the sole parameter in two situations of the pressurized fault are plotted in Fig. 3.3.

After determining  $\lambda$  from equation (3.8), we now look for the solution for slip distribution  $\bar{\delta}$ . Equation (3.8) can be inverted for  $d\bar{\delta}/d\bar{x}$

$$\frac{d\bar{\delta}}{d\bar{x}} = -\frac{\sqrt{1-\bar{x}^2}}{\pi} \int_{-1}^1 \frac{\operatorname{erfc}|\lambda\bar{s}|}{\sqrt{1-\bar{s}^2}} \frac{1}{\bar{x}-\bar{s}} d\bar{s} \quad (3.11)$$

using the methodology of Gauss-Chebyshev quadrature similarly as equation (3.8), the right hand of equation (3.11) can be estimated to get the result of  $\bar{\delta}$ .

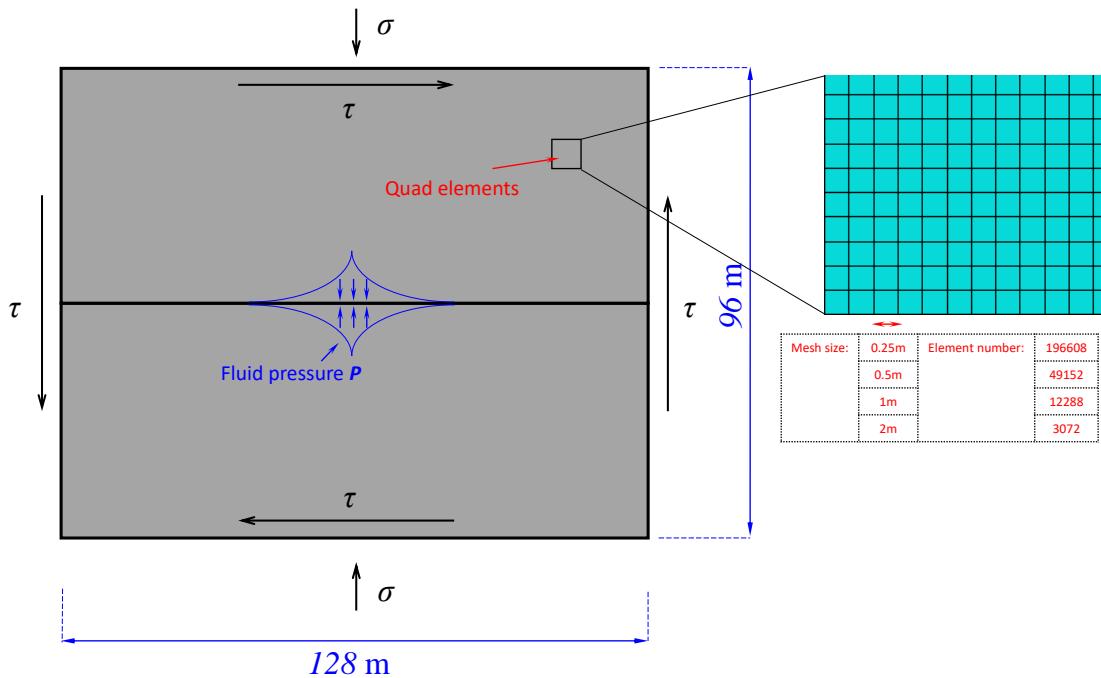


Figure 3.4: Numerical model configuration in Abaqus. Model size: 128 m  $\times$  96 m; element size: 0.25 m  $\times$  0.25 m. The number of nodes is 198018, and the number of elements is 196608. Normal stress  $\sigma$  is 50 MPa. Shear stress  $\tau$  is 12 MPa. A diffusive fluid pressure  $P$  is applied on the fault plane.

After having the results of fluid pressure and fault slip evolution with time, we configure a 2D 128 m  $\times$  96 m finite element model in Abaqus to compare our finite element model with the self-similar model. The model has 198018 nodes and 196608

elements. Each element is a 4-node plane strain (element type CPE4R in Abaqus) quad, ignoring the strain in the Z direction to simulate the mechanical performance of the fault. The sizes of the mesh vary between  $0.25 \text{ m} \times 0.25 \text{ m}$ ,  $0.5 \text{ m} \times 0.5 \text{ m}$ ,  $1 \text{ m} \times 1 \text{ m}$  and  $2 \text{ m} \times 2 \text{ m}$ . Respectively, the element numbers are 196608, 49152, 12288 and 3072. The set of mesh resolutions is designed to compare the numerical simulation results with the theoretical estimations. The boundary condition of the model is that, on the top and bottom, normal stress  $\sigma$  is 50 MPa. Around the whole model, the shear stress  $\tau$  is 12 MPa, as shown in Fig. 3.4 to make the system stable under the force balance. The fault displacement in  $y$  direction  $U_2$  is limited to 0 mm. Along the fault plane, increased fluid pressure is applied as the self-similar model proposed by Viesca (2021).

### 3.1.3 Numerical results comparison

Here for specific choices of fault parameters:  $\sigma = 50 \text{ MPa}$ ,  $\tau = 12 \text{ MPa}$ ,  $\mu = 0.5$ ,  $G = 30 \text{ GPa}$ ,  $\nu = 1/4$ ,  $G' = 20 \text{ GPa}$ . The solution to equation (3.11) is shown in Fig. 3.5. The solid lines are theoretical solutions in time  $t = 1, 5$  and  $10 \text{ min}$ .

In Figure 3.5, we compare the fault slip results obtained from Abaqus with the numerical slip distributions of Viesca (2021) at three different time intervals after the initiation of fluid injection ( $t = 1, 5, \text{ and } 10 \text{ minutes}$ ). The theoretical results are represented by black lines, while the finite element results are plotted in various colors, each corresponding to a different mesh size. For the finite element model, we used a friction coefficient of 0.5, Young's Modulus  $E$  of 75 GPa, and Shear Modulus  $G$  of 30 GPa, which were held constant across all mesh sizes.

During the configuration and calculation of the finite element model, we discovered that the mesh resolution greatly affects the mechanical performance of the fluid injection-induced slip. Therefore, we designed the mesh sizes in the finite element model to vary between  $0.25\text{m} \times 0.25\text{m}$ ,  $0.5\text{m} \times 0.5\text{m}$ ,  $1\text{m} \times 1\text{m}$ , and  $2\text{m} \times 2\text{m}$ . The results in Figure 3.5 show that with higher numerical resolution, the finite element model's physical and mechanical behavior more closely matches the benchmark model estimation. In addition to the amplitude of fault slip, the onset of slip fronts at different times also consistently matches Viesca (2021)'s numerical solutions. This comparison verifies that our coupled finite element model is capable of reproducing the fault slip induced by fluid injection.

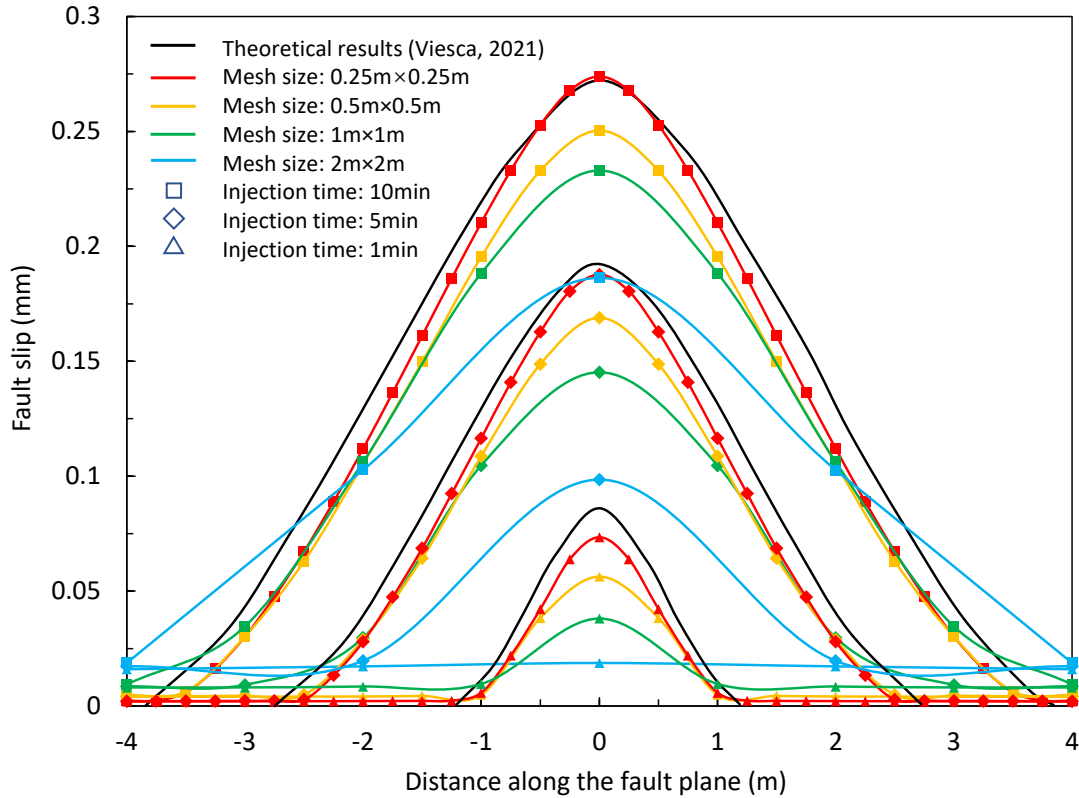


Figure 3.5: Comparison between finite element model's fault slip results and theoretical estimation by Viesca (2021). Friction coefficient 0.5, Young's Modulus  $E = 75\text{GPa}$ , Shear Modulus  $G = E/[2(1 + \nu)] = 30\text{GPa}$ . Mesh sizes in the finite element model vary between  $0.25\text{m} \times 0.25\text{m}$ ,  $0.5\text{m} \times 0.5\text{m}$ ,  $1\text{m} \times 1\text{m}$  and  $2\text{m} \times 2\text{m}$ . The results are at three time intervals 1, 5 and 10 min since fluid injection.

## 3.2 Experimental calibration for numerical/hydro-mechanical model

In Chapter 2, we introduced the experimental setup, including the laboratory injection experiment's loading process and material properties. This section will describe the experimental assembling of the triaxial compression and injection equipment and the rock specimen.

### 3.2.1 Experiment assembling

The fractured rock sample was assembled with a triaxial oil-medium equipment of the Rock and Ice Physics Laboratory at the University College of London, shown in Fig. 3.6 (a) (Eccles *et al.*, 2005). The borehole is located at the bottom of the sample. And the bottom of the specimen was connected to a fluid injection system, including a servo-hydraulic pore fluid intensifier, a pressure transducer measuring the pore pressure of the injection hole and a Linear Variable Differential Transducer (LVDT) measuring the variations of the fluid volume of the intensifier. On the other side, the top of the specimen was linked to a pressure transducer. The triaxial stresses were realized by two independent loading equipment: an electromechanical pump and a servo-hydraulic actuator. The pump controlled the confining pressure  $P_c$  and the axial stress  $\sigma_1$  was controlled by the actuator, respectively. The specimen shortening equaled the axial ram displacement, measured by an external device, and was corrected from the stiffness of the loading column. A load cell measured the axial loading. The relative fault slip displacement is computed by the projection of the specimen shortening on the fault plane direction. The normal and shear stresses on the fault plane are acquired by solving the equation (2.16) in Chapter 2 with the axial and confining stress state of the sample.

### Effective stiffness of the loading system

The effective Young's modulus of our numerical model will be estimated. In the numerical model based on the laboratory experiment (Passelègue *et al.*, 2018), the injection test is conducted on a rock sample excluding the loading cap and pedestal. From Passelègue *et al.* (2018), the fault slip and hydro-mechanical behaviors are dependent on the stiffness of the whole loading system. Thus, an effective stiffness of the sample in the numerical model representing the rock with the steel loading column needs to be assumed, in order to make a comparison between the experimental and numerical results. However, Young's modulus of the loading cap and pedestal is unknown from the experiment data. To estimate the effective Young's modulus, a group of parametric numerical study will be conducted in the following section to be as a calibration between the numerical model and experimental model.

### Effective Young's modulus

After describing the assembling of the experiment, we will now estimate the effective Young's modulus of the whole loading system. As presented above, the experimental

study contains the rock sample with the steel loading column, while the numerical study is based on an equivalent fault sample where the loadings are directly applied.

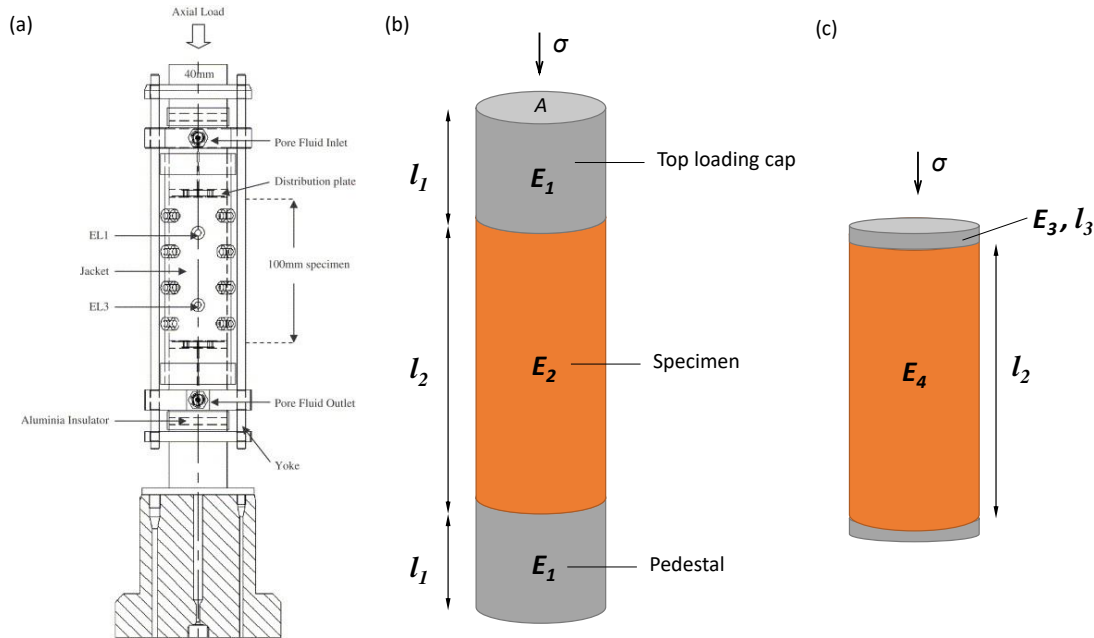


Figure 3.6: (a) Sample assembly: four electrodes of silver paint are mounted on the rock specimen, 40 mm in diameter by 100 mm long, inside the yoke. (Eccles *et al.*, 2005) (b) Simplified model representing the loading cap and specimen assembling of the laboratory triaxial fluid injection experiment (Passelègue *et al.*, 2018).  $\sigma$  is axial stress, leading to a shortening of the length of the whole loading system  $l_{exp}$ .  $l_{exp} = 2l_1 + l_2$ , where  $l_1$  is the length of the top loading cap and the pedestal, and  $l_2$  is the length of the specimen.  $E_1$  and  $E_2$  are Young's modulus of the loading column and the fault sample. (c) A schematic view of the finite element model, whose effective stiffness  $E_{nm}$  is equivalent to the experimental model  $E_{exp}$ . Young's modulus and length of the loading cap and pedestal in the numerical model are  $E_3$  and  $l_3$ . The fault sample has an elastic strength of  $E_4$  and its length  $l_2$  is the same as that of the laboratory experiment.

A simplified model representing the experimental assembling described above is shown in Fig. 3.6 (b). The simplified model consists of the top loading cap, the specimen and the pedestal. Here, we assume that the top and bottom steel have the same length  $l_1$  and Young's modulus  $E_1$ . The elastic modulus and length of the

specimen are  $E_2$  and  $l_2$ . Another simplified model representing the numerical model is shown in Fig. 3.6 (c). In the finite element model, the normal axial loading  $\sigma$  is directly applied on the top of the rock sample. So here we assume in the equivalent model that Young's modulus of loading cap and pedestal  $E_3 \rightarrow +\infty$ , the length of the loading cap  $l_3 \rightarrow 0$ , the modulus of the numerical model is  $E_4$  which has the same length  $l_2$  with the experimental specimen.

From the experiment data (Passelègue *et al.*, 2018), we already know the length of the specimen  $l_2 = 100$  mm, Young's modulus  $E_2 = 54$  GPa, the stiffness of the loading machine  $k_1 = 480$  kN/mm, and the results of the fault slip during the injection process. The definition of stiffness and the relation between stiffness and elastic modulus are (Jaeger *et al.*, 2009)

$$k = \frac{F}{\Delta l} = \frac{E_{exp}A}{l}, \quad E_{exp} = \frac{k l_{exp}}{A} = E_{nm} \quad (3.12)$$

where  $F$  is the force on the body,  $\Delta l$  is the change in length,  $A$  is the cross-sectional area,  $l_{exp}$  is the total length of the loading system,  $E_{exp}$  and  $E_{nm}$  are the equivalent young's modulus of the whole loading system in the laboratory experiment and numerical model.

To calibrate the numerical model with the experiment results, the equivalent Young's modulus  $E_{exp}$  of the whole laboratory loading system including the top loading cap, the specimen and the pedestal (Fig. 3.6 (b)) will be computed. From the definition of strain, we have

$$\frac{\sigma}{E_{exp}} = \frac{\Delta l_{exp}}{l_{exp}} = \frac{2\Delta l_1}{l_{exp}} + \frac{\Delta l_2}{l_{exp}} \quad (3.13)$$

where  $\sigma$  is axial stress,  $l_{exp} = 2l_1 + l_2$  is the total length,  $\Delta l$ ,  $\Delta l_1$  and  $\Delta l_2$  are the shortening of the whole loading system, top-bottom part and the specimen. By replacing the relative shortening with the stress-strength relationship, equation (3.13) can be written as

$$\frac{\sigma}{E_{exp}} = \frac{2\sigma X_1}{E_1} + \frac{\sigma X_2}{E_2} \quad (3.14)$$

where  $X_1 = l_1/l_{exp}$  and  $X_2 = l_2/l_{exp}$ . By dividing  $\sigma$  from both sides, we get

$$E_{exp} = \frac{E_1 E_2}{2X_1 E_2 + X_2 E_1} \quad (3.15)$$

Equation (3.15) is the expression of the equivalent elastic modulus in the experiment loading system.

Similarly, in the numerical model (Fig. 3.6 (c)) the stress-strain relationship of the whole loading system can be written as

$$\frac{\sigma}{E_{nm}} = \frac{2\sigma X_3}{E_3} + \frac{\sigma X_4}{E_4} \quad (3.16)$$

where  $E_{nm}$  is the equivalent young's modulus in the numerical model,  $l_{nm} = 2l_3 + l_2$  is the total length,  $X_3 = l_3/l_{exp}$  and  $X_4 = l_2/l_{exp}$ . With the assumption of  $E_3 \rightarrow +\infty$  and  $l_3 \rightarrow 0$ , we have  $X_3/E_3 \rightarrow 0$  and  $X_4 \rightarrow 1$ . Equation (3.15) and (3.16) can be written as:

$$E_{exp} = \frac{E_1 E_2}{2X_1 E_2 + X_2 E_1} = E_{nm} = E_4 \quad (3.17)$$

Consequently, the elastic modulus  $E_4$  in the numerical model is equivalent to the whole loading system. Here, the missing length of the loading column  $l_1$  makes the elastic modulus  $E_1$  unknown in equation (3.17) from the experiment data. We need to conduct a set of numerical model calibration tests with different equivalent elastic modulus  $E_4$  to verify that the equivalent model matches experiment results and inversely resolve the length of loading cap  $l_1$  and its elastic modulus  $E_1$  using equation (3.12) and (3.15).

In the next section, the parametric study with a set of equivalent Young's modulus of the loading system will be discussed. The calibration of the numerical model results will be compared with the laboratory experiment. This calibration study verifies the reproduction of numerical results with the experiment.

### 3.2.2 Parametric study of material property

In this section, the whole loading column including the specimen, top loading cap and the pedestal in the laboratory experiment is modeled by an equivalent specimen with the effective Young's modulus  $E_{nm}$ . The numerical calibration tests are simulated in both 2 dimensions and 3 dimensions.

#### 2D calibration

A 2-dimensional finite element model is configured in Abaqus to simulate the laboratory scale injection experiment. The FE model contains 2361 four-node plane strain elements (CPE4R) and 2513 nodes.

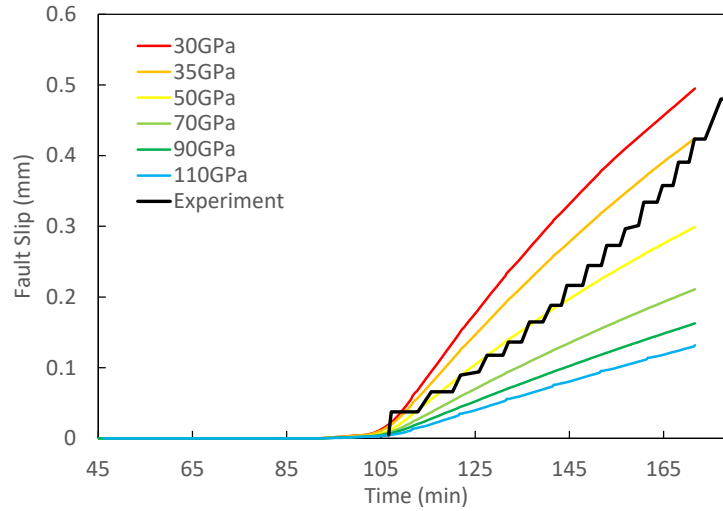


Figure 3.7: 2D finite element model calibration results. Static friction coefficient  $\mu_s = 0.578$ , dynamic friction coefficient  $\mu_d = 0.45$ , critical slip distance  $d_c = 0.35\text{mm}$ . Hydraulic diffusivity  $D = 5 \times 10^{-5} \text{ m}^2/\text{s}$ . The confining pressure is 100 MPa and the injection rate is 1 MPa/min.

A displacement-dependent slip weakening friction coefficient is chosen to solve the pre-existing fault plane contact problem, as indicated from triaxial compression rock failure experiments (Wawersik and Brace, 1971; Wawersik and Fairhurst, 1970; Wong, 1982). The friction coefficient declines linearly with slip displacement and keeps still when the slip reaches the critical slip distance  $d_c$ . The static friction coefficient is estimated from the sliding critical stress state and equation (2.16). When shear stress reaches its peak value ( $\tau_p = 78 \text{ MPa}$ ), the fault plane starts to slip and the static friction coefficient is 0.578 at this point. According to the slip history in the injection experiment by Guglielmi *et al.* (2015b), the numerical model by Bhattacharya and Viesca (2019) derived the slip weakening model whose friction coefficient weakened linearly from 0.6 to 0.4. In addition, triaxial compression rock failure experiments in the laboratory (Marone, 1998) revealed that the friction coefficient decreased linearly from 0.555 to 0.54 with rock slip. During the numerical simulation, we also find that the dynamic friction coefficient  $\mu_d$  affects the fault stability, which will be discussed in more detail later in this section. Based on the above injection experiment, numerical derivation, laboratory rock failure tests and fault stability, in this calibration simulation the dynamic friction coefficient  $\mu_d$  is chosen as 0.45. In terms of the critical slip distance  $d_c$ , the above experiments show that the friction coefficient keeps still when the rock slip is around 0.4 mm - 0.5 mm.

Here we take  $d_c = 0.35$  mm.

The stress and loading conditions of the specimen are consistent with the experiment. The confining pressure is 100 MPa and the injection rate is 1 MPa/min. Injection begins at an initial stress equal to 90%  $\tau_p$ . Pore pressure diffuses along the fault plane and the hydraulic diffusivity  $D = 5 \times 10^{-5} \text{ m}^2/\text{s}$ . The diffusing fluid pressure is coupled in the finite element model with a finite difference solver in 1-dimension proposed by Almakari *et al.* (2020) and Almakari (2019a,b). A set of six numerical tests with effective Young's modulus  $E_{nm}$  ranging from 30 GPa to 110 GPa are simulated to be calibrated with the experiment. The results of the calibration tests are shown in Fig. 3.7.

### 3D calibration

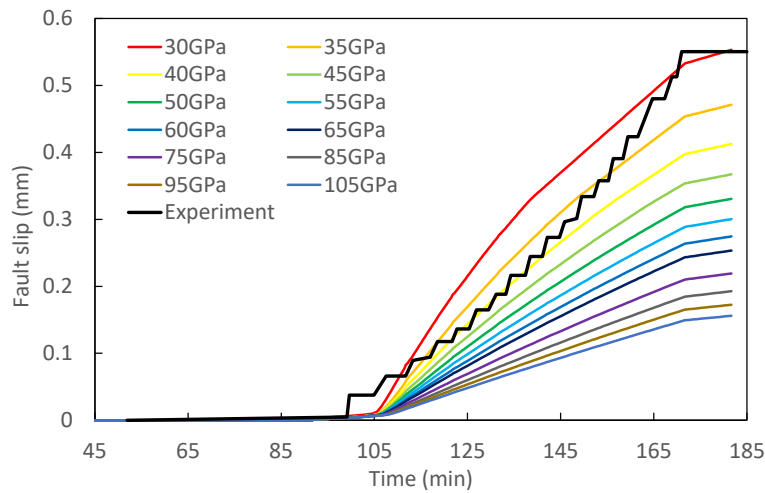


Figure 3.8: 3D finite element model calibration results. Static friction coefficient  $\mu_s = 0.578$ , dynamic friction coefficient  $\mu_d = 0.45$ , critical slip distance  $d_c = 0.35\text{mm}$ . Hydraulic diffusivity  $D = 5 \times 10^{-5} \text{ m}^2/\text{s}$ . The confining pressure is 100 MPa and the injection rate is 1 MPa/min.

Another 3-dimensional finite element model is established to do the calibration test in order to reproduce the experiment. The model is a cylinder with a section diameter of 40 mm and a height of 100 mm, which is consistent with the experimental sample. The model contains 23522 linear hexahedral eight-node brick elements (type C3D8) and 26400 nodes. The numerical approach is the same as the 2D model

described above, coupled with the slip-weakening friction law and the diffusion solver. The loading process and boundary conditions of the 3D numerical are consistent with the laboratory experiment to compare the slip results. A set of twelve numerical tests with the effective Young's modulus  $E_{nm}$  ranging from 30 GPa to 105 GPa are simulated to be calibrated with the experiment. The results of the calibration tests are shown in Fig. 3.8.

### 3.2.3 Nucleation length and fault stability

According to the earthquake nucleation theory (Scholz, 2019), stable fault slip is likely to turn to an unstable state if the friction coefficient of the contact plane change from static  $\mu_s$  into dynamic  $\mu_d$ . The fault remained stable and aseismic when the rupture length did not exceed the critical nucleation length  $L_c$ . When the accelerating aseismic slip exceeded  $L_c$ , the fault became unstable with seismic slip. The critical nucleation length is given by

$$L_c = \frac{Gd_c}{\sigma_n(\mu_s - \mu_d)} \quad (3.18)$$

where  $G$  is the shear strength of the fault,  $d_c$  is the critical slip distance of the friction weakening,  $\sigma_n$  is the normal stress on the fault plane.

As mentioned in the choice of the residual friction  $\mu_d$  and critical slip distance  $d_c$  in the calibration modeling, we find the frictional parameters have an influence on the fault stability. In this subsection, we present the results of the relationship of fault stability with frictional parameters in Fig. 3.9. The four  $d_c$  values 0.25, 0.3, 0.35, and 0.4 mm were taken, and dynamic friction coefficient  $\mu_d$  ranged from 0.33 to 0.53. With lower  $\mu_d$  and  $d_c$ , it is more difficult for the numerical results of fault slip to be stable. Here we plotted the threshold line between stable and unstable faults. Below the dashed threshold line, the fault is unstable and above is stable.

When the values of  $d_c = 0.35$  mm and  $\mu_d = 0.35$  were used in the simulation with a shear modulus  $G$  of 11.8 GPa and normal stress  $\sigma_n$  of 135 MPa, the results showed a rapid acceleration of fault slip, indicating instability. Using these physical values in Equation (3.18), we obtained a critical nucleation length of  $L_c = 140$  mm. Therefore, Equation (3.19) describes the relationship between  $\mu_d$  and  $d_c$  as:

$$\mu_d = \mu_s - \frac{G}{L_c \sigma_n} d_c = 0.578 - 0.624 d_c \quad (3.19)$$

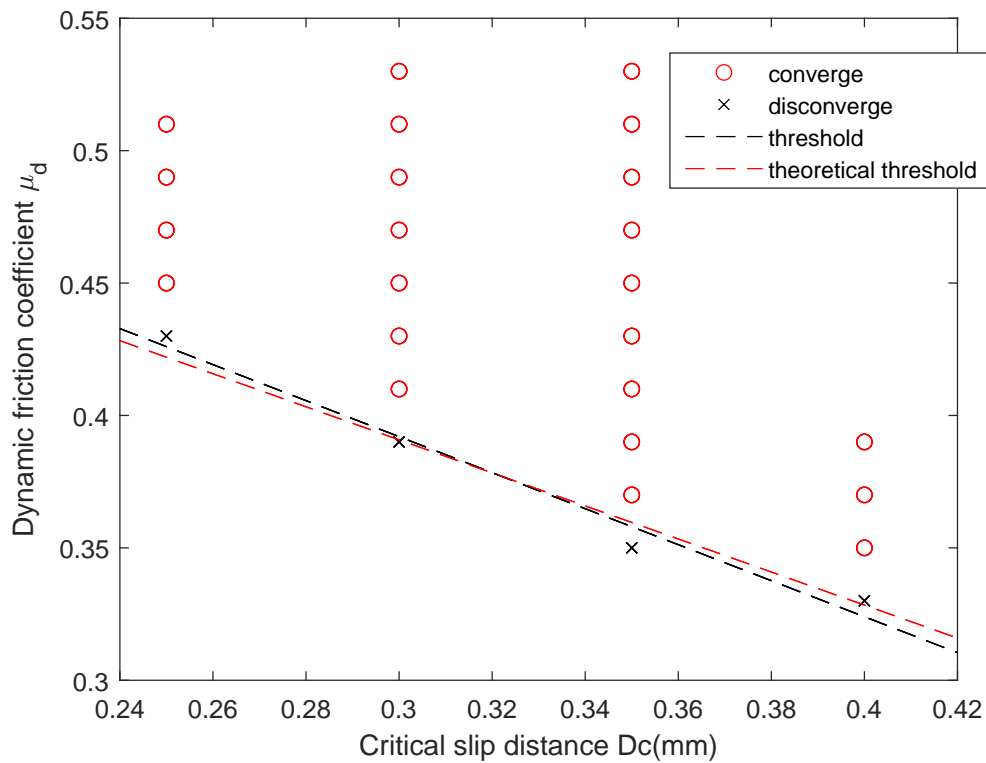


Figure 3.9: Convergence of the numerical model with the frictional parameter tests. Below the dashed threshold line, the fault is unstable and above is stable.

The red dashed line in Fig. 3.9 represents the result of Equation (3.19), which is compared to the black dashed line representing the finite element numerical relationship between  $\mu_d$  and  $d_c$ . This comparison shows that our coupled numerical model can simulate the stable and unstable fault sliding behavior with different friction parameters, consistent with earthquake rupture nucleation theory.

### 3.2.4 Result comparison

In this numerical test, the estimated static friction coefficient is 0.578, close to the static friction 0.6 observed in the test at constant fluid pressure. The calibration results (Fig. 3.7 and 3.8) show that in both 2D and 3D models, the trend is clear that the slip displacement and slip rate increase when the equivalent Young's modulus

of the whole system  $E_{nm}$  is decreasing. Results show when  $E_{nm} = 30$  GPa, numerical fault slip behavior matches the experiment best. Through equation (3.12) and (3.15), the value of loading machine stiffness  $k_1 = 480$  kN/mm and the equivalent Young's modulus of the whole experimental system from the calibration results  $E_{exp} = E_{nm} = 30$  GPa, we estimate the length of the loading column  $l_1 = 56.3$  mm and  $E_1 = 21.5$  GPa. In the numerical finite element model, when Young's modulus is 30 GPa, the average slip displacement along the fault plane reaches 0.55 mm when the injection ends, which is consistent with the experiment result. Meanwhile, at the injection rate of 1 MPa/min, borehole fluid pressure at the onset of slip in both 2D and 3D faults are 40 MPa, aligning with the experimental results.

From the results between the numerical and experimental fault slip, we see some differences. The curve of the relative displacement of the fault plane has different shapes (Fig. 3.7 and 3.8). In the numerical model, the slope of fault displacement at the onset of slip is higher than that of the experiment, which means the slip rate when it starts is larger. While near the end of the fluid injection, when the pressure is approaching 90 MPa, the slip rate in numerical simulation decreases but in the experiment, the slip velocity is observed to accelerate. As was indicated from experimental studies, the hydraulic diffusivity change influences the fault slip modes after reactivation, whatever seismic or aseismic (Guglielmi *et al.*, 2015a; Scuderi and Collettini, 2016; Scuderi *et al.*, 2017). On the other hand, many experiments are conducted to research the intact rock permeability dependence with both confining pressure and fluid pressure (Bernabe, 1986; Brace *et al.*, 1968; Kilmer *et al.*, 1987; Neuzil, 1986; Rutqvist and Stephansson, 2003). In the numerical calibration in this chapter, we use a constant hydraulic diffusivity, which may not be realistic to restore the sliding behavior. Also, the displacement-dependent friction coefficient plays a role in sliding. If the dynamic friction coefficient  $\mu_d$  or the sliding threshold  $D_c$  influences the slip curve is to be discussed. What parameters control the slip behavior of the fault in fluid injection experiments are not well understood. In the following chapters, we will focus more on how the injection conditions, fault's hydro-mechanical properties, stress state and frictional properties could impact the fault reactivation and slip behavior.

### 3.3 Conclusion

In comparison with the benchmark theoretical model by Viesca (2021), we established an injection-induced fault slip model with simple self-similar geometry using

the finite element method coupled with a diffusion equation solver. The numerical simulation results by FEM are compared with the solution by Viesca (2021) (Fig 3.5). Results show that a higher numerical model resolution can better match the results of the theoretical model. With a constant friction coefficient, the same material properties, same loading and boundary conditions as the theoretical model, our finite element model coupled with the fluid diffusion solver reproduces the fault slip results. Fault slip and the slip propagation are both consistent with Viesca (2021)'s numerical model.

Additionally, a set of more complicated finite calibration tests are configured. For the calibration, we use the experimental results of the laboratory injection experiments by Passelègue *et al.* (2018). The models are in 2D and 3D, with the same geometry as in the indoor injection experiments (Passelègue *et al.*, 2018). The model is coupled with a user-defined slip-weakening friction law and a fluid diffusion solver in the finite element method. In these models, the parametric study with a set of effective Young's modulus of the whole loading column is conducted to calibrate the numerical model with an accurate Young's modulus of the fault sample. Results show that a lower elastic modulus promotes the sliding of fault during fluid injection. When the equivalent Young's modulus is 30 GPa, the fault slip results are consistent with experimental results. We also conducted numerical simulations to investigate the effect of friction parameters on fault stability. The results show that our friction model is consistent with the earthquake rupture nucleation theory. The above calibration and numerical tests on fault stability demonstrate that our coupled model can be used to simulate and reproduce fault reactivation experiments induced by fluid injection.

However, differences between numerical and experimental results show that how the mechanical parameters influence the fault slip accumulation is not fully understood. In the following chapters, we are going to do different groups of parametric numerical simulations, including the fault's hydro-mechanical properties, stress state and frictional properties, to better reveal the mechanism of fault reactivation and slip behavior under the fluid injection.



## Chapter 4

# Effect of hydro-mechanical, injection and frictional parameters on the slip reactivation: Simulation and results

Résumé . . . . .	82
Summary . . . . .	82
4.1 Introduction . . . . .	83
4.2 Numerical model . . . . .	86
4.2.1 Mechanical problem: geometry, loading process and boundary conditions . . . . .	86
4.2.2 Governing equations . . . . .	89
4.3 Effect of hydraulic parameters . . . . .	91
4.4 Effect of stress state . . . . .	99
4.4.1 Initial stress . . . . .	99
4.4.2 Confining stress . . . . .	102
4.5 Effect of frictional parameters . . . . .	104
4.6 Discussion . . . . .	106
4.6.1 Rupture propagation speed . . . . .	107
4.6.2 Maximum slip vs. Injection volume . . . . .	111
4.7 Conclusion . . . . .	117

## Résumé

Les failles peuvent être réactivées de manière a-sismique par injection de fluide, mais le mécanisme et les facteurs qui contrôlent le glissement et la propagation de la rupture ne sont pas complètement compris. Dans cette étude, nous développons une méthode des éléments finis 3D inspirée des expériences d'injection à l'échelle centimétrique en laboratoire afin d'étudier le contrôle hydro-mécanique sur la réactivation du glissement a-sismique. Nous étudions l'impact du débit d'injection, de la diffusivité hydraulique, de l'état de contrainte et des propriétés de friction sur la vitesse de propagation et l'amplitude maximale des événements de glissement a-sismique générés dans notre modèle. Nous montrons que la propagation de l'avant du glissement a-sismique simulé est conforme aux prédictions basées sur la mécanique de la rupture élastique linéaire. Dans les plages de paramètres typiques, la contrainte et le débit d'injection ont un effet prédominant sur la propagation du glissement, tandis que les propriétés de friction et la diffusivité de la faille jouent un rôle secondaire. Une contrainte initiale proche de la rupture et des débits d'injection élevés augmentent à la fois la vitesse de l'avant du glissement et réduisent le temps de réactivation des événements de glissement a-sismique. Nos simulations conduisent également à une relation d'échelle de glissement final maximal de la forme  $\sqrt{\Delta V}$ , où  $\Delta V$  est le volume injecté, ce qui, en supposant une variation de cisaillement constante, conduit à une relation d'échelle maximale du moment sismique de la forme  $\Delta V^{3/2}$ . Cette dernière prédiction est en accord avec des études mécaniques et théoriques récentes sur le glissement a-sismique. L'approche de modélisation originale présentée ici pourrait également être utilisée pour renforcer l'interprétation mécanique des expériences en laboratoire.

## Summary

Faults can be reactivated aseismically by fluid injection but the mechanism and factors controlling the slip and rupture propagation behavior are not fully understood. Here, we develop a 3D finite element method inspired by injection experiments at the laboratory centimetric scale, to investigate the hydro-mechanical control on aseismic slip reactivation. We study the impact of injection rate, hydraulic diffusivity, stress state and frictional properties on the propagation speed and the maximum magnitude of aseismic slip events generated in our model. We show that the propagation of simulated aseismic slip front is consistent with predictions based on linear elastic fracture mechanics. Considering typical parameter ranges, stress and

injection rate have a dominant effect on slip propagation, while frictional properties and fault's hydraulic diffusivity play a secondary role. Initial stress close to failure and high injection rates both increase slip front speed and reduce the reactivation time of aseismic slip events. Our simulations also lead to a maximum final slip scaling as the  $\sqrt{\Delta V}$  where  $\Delta V$  is the injected volume, which under an assumption of constant shear drop, leads to a maximum seismic moment scaling as  $\Delta V^{3/2}$ . This latter prediction is consistent with recent mechanical and theoretical studies on the aseismic slip. The original modeling approach presented here could also be used to strengthen the mechanical interpretation of laboratory experiments.

## 4.1 Introduction

Fluid injection is a widely used technique in various industrial activities, such as hydraulic fracturing of shale formations or coal seams to obtain natural gas and oil (Ellsworth, 2013; Maxwell, 2014), Enhanced Geothermal System (EGS) for thermal power generation from hot and low permeability rock reservoirs (Blöcher *et al.*, 2018; Riffault *et al.*, 2018), re-injection of wastewater disposal in oil and gas industry (Majer and Peterson, 2007; McGarr, 2014) and Carbon Capture and Storage (CCS) for reducing the carbon content in the atmosphere (Rinaldi *et al.*, 2014). Despite its benefits, fluid injection is often associated with seismic events. Micro-seismic events are observed near the fluid injection wells for several days, months or years, even after shut-in and bleed-off (Deichmann and Giardini, 2009; Mukuhira *et al.*, 2017; Schmittbuhl *et al.*, 2021). In addition to these small earthquakes, fluid injections also trigger large earthquakes causing significant damage, such as the  $M_W$  5.7 Oklahoma earthquake (Keranen *et al.*, 2013) and the  $M_W$  5.5 Pohang earthquake in South Korea (Grigoli *et al.*, 2018). Earthquakes correspond to fast (cm/s or m/s) slip on preexisting critically loaded. Reactivation happens when shear stress surpasses the frictional failure envelope described by Byerlee's law (Barton, 1976; Byerlee, 1968; Byerlee, 1978; Jaeger *et al.*, 2009). Segall (1989) proposed that far-field faults can be indirectly reactivated by fluid pressure through the effects of poroelastic coupling, modifying the standard theory.

One notable observation about induced seismicity is the correlation between the maximum magnitudes of induced earthquakes and the total volume of fluid injected in some cases (Grandin *et al.*, 2017; Grigoli *et al.*, 2018; Keranen *et al.*, 2013; Li *et al.*, 2021; McGarr and Barbour, 2017; Westaway and Burnside, 2019; Yeck *et al.*, 2016, 2017). To better understand the underlying mechanisms leading to ground motion

and predict the potential for large magnitude seismicity, studies have investigated the relationship between maximum earthquake magnitudes and injection volume (McGarr, 1976; McGarr, 2014), with the prevailing theory suggesting that the maximum seismic moment  $M_0^{max}$  does not exceed an upper bound that is dependent on the injection volume and shear modulus. However, recent observations of induced seismicity in Enhanced Geothermal Systems (Diehl *et al.*, 2017; Kim *et al.*, 2018), hydraulic fracturing (Atkinson *et al.*, 2016), and field pilot experiments (Guglielmi *et al.*, 2015b) have challenged this theory by revealing that the seismic magnitudes can surpass the upper bound  $M_0^{max}$ .

In addition to earthquakes, the fluid injection can also trigger slow aseismic slip on faults (slip rates  $\ll$  mm/s). The aseismic slip has been observed at geothermal sites (Bourouis and Bernard, 2007) and in in-situ fault injection experiments (Cappa *et al.*, 2019; Cornet, 2016; Guglielmi *et al.*, 2015a,b; Lengliné *et al.*, 2017), where it was promoted by an increase in fluid pressure. Aseismic slip events propagate along faults leading to stress transfers eventually triggering earthquakes (Cappa *et al.*, 2018, 2019; Lohman and McGuire, 2007; Wynants-Morel *et al.*, 2020). Pore pressure accelerates fault opening and aseismic slip. Aseismic slip then redistribute stress, which triggers earthquakes (Cappa *et al.*, 2019). So that seismic events can be induced in non-pressurized regions. This mechanism is supported by observations of migrating earthquakes during natural and induced swarms (De Barros *et al.*, 2020; Eyre *et al.*, 2019; Lengliné *et al.*, 2017; Lohman and McGuire, 2007). Aseismic slip is thus an important component in the triggering of induced earthquakes. However, despite extensive studies on the source mechanism of seismicity, there is still a lack of understanding of how the hydraulic, geomechanical, and frictional parameters affect the dynamics of aseismic slip. In particular, what controls the maximum aseismic moment and the slip front propagation is not fully understood. Comprehending fault slip reactivation mechanisms due to fluid injection is crucial to managing associated risks.

Over the past decades, injection-induced fault slip has been studied through laboratory (cm scale) and field (decametric scale) experiments, enabling the monitoring of aseismic slip, pore-pressure evolution and seismicity caused by fluid injection. Lab experiments have focused on the impact of various hydro-mechanical and injection parameters on the reactivation behavior of faults, with findings suggesting that aseismic deformation plays a significant role in the total energy budget (Goodfellow *et al.*, 2015). Passelègue *et al.* (2018) found that intense and localized fluid pressure perturbations can reactivate large faults, with the level of local over-pressure and

peak fluid pressure at the injection hole depending on the injection pressure rate and stress conditions. In the laboratory experiments on rock samples from the LSBB fault site, Cappa *et al.* (2019) found that aseismic slip in pressurized regions can activate faults along non-pressurized patches, confirming aseismic creep as a mechanism that increases shear stress beyond the fluid pressure front and promotes earthquake triggering. In the field, evidence of aseismic slip induced by fluid injection was first observed in southeastern France (Derode *et al.*, 2013; Guglielmi *et al.*, 2015b), and a dual process was proposed based on experiments in low-permeable shale and highly-fractured limestone formations (De Barros *et al.*, 2018). Following the in-situ observations from Guglielmi *et al.* (2015b), Bhattacharya and Viesca (2019) estimated hydro-mechanical parameters of an activated fault and slip evolution over time, finding that fluid injection leads to aseismic slip which, as it accumulates, causes earthquake nucleation outside of the fluid injection region due to the front of aseismic rupture propagating faster and further than the pore pressure front, in line with recent observations (Cappa *et al.*, 2019; De Barros *et al.*, 2018; Guglielmi *et al.*, 2015b; Schultz *et al.*, 2017).

This problem could also be studied numerically. Using the 3-Dimensional Distinct Element Code (3DEC), Cappa *et al.* (2006, 2018, 2019) and Guglielmi *et al.* (2008) were able to evaluate the coupled hydraulic and mechanical behavior of cracked rocks or fault zones under fluid pressurization. The model included the hydromechanical coupling of a 2-Dimensional (2D) fault plane at an in-situ decametric scale, rate-and-state friction and stress- and strain-dependent permeability. Their analysis revealed that the evolving fault hydraulic diffusivity depends on stress and fluid pressure, and that aseismic slip can trigger seismic slip in the far field when the propagating aseismic slip front exceeds the critical nucleation length. Another recent numerical model by Dublanchet and De Barros (2021) simulated a tectonic fault in 1-Dimension (1D) coupling rate-and-state friction and time- and space-dependent hydraulic diffusivity, suggesting that seismic migration is primarily controlled by aseismic slip propagation and stress perturbation, as opposed to direct pore pressure triggering. A numerical model with a 2D fault plane, slip-weakening friction and constant hydraulic diffusivity developed by Galis *et al.* (2017) predicts that most induced earthquakes are self-arresting ruptures obeying a scaling relation of the form  $M_0 \propto \Delta V^{3/2}$ , where  $M_0$  represents the seismic moment and  $\Delta V$  is the total fluid injection volume. Additionally, the model indicates that strong pressure perturbations may cause runaway ruptures and that both this model and the model of Garagash and Germanovich (2012) based on fracture mechanics found that the propagation of dynamic rupture is sensitive to the initial stress state of the

fracture. In a recent study by Sáez *et al.* (2022), a 3D model of a planar fault with constant friction was simulated, resulting in the aseismic slip and a scaling relation between aseismic moment  $M_0$  and injection volume  $\Delta V$  of  $M_0 \propto \Delta V^{3/2}$ . However, these numerical models have not simulated the laboratory-scale fluid injection experiments on a pre-fractured rock sample, leaving a knowledge gap on the impact of varying hydraulic, stress state, and frictional parameters on aseismic slip behavior.

In this study, our objective is to investigate the aseismic slip behavior of a laboratory scale pre-existing fault induced by fluid injection, as aseismic slip plays an important role in triggering earthquakes by generating the shear stress and aseismic creep outpacing the fluid pressurized region (Cappa *et al.*, 2019; Dublanquet and De Barros, 2021; Guglielmi *et al.*, 2015b). We will, in particular, investigate what is the mechanical control on (i) aseismic slip front propagation and (ii) what is the scaling between aseismic moment and injected volume. We will further design a 3D finite element method (FEM) numerical model and calibrate them using a set of laboratory experiments (Passelègue *et al.*, 2018, 2020). By coupling the models with a solver of fluid diffusivity and slip-weakening friction criterion, we aim to reproduce experimental results and study the impact of hydraulic, stress state, and frictional parameters on aseismic slip reactivation in a laboratory scale saw-cut rock sample. In the following, we will first present the modeling approach and the calibration. We will then present the results of our parametric study, and we will finally confront our predictions to fracture mechanics theory, and discuss scaling laws about fluid-induced aseismic slip.

## 4.2 Numerical model

### 4.2.1 Mechanical problem: geometry, loading process and boundary conditions

Our model reproducing the laboratory triaxial compression experiment with fluid injection is inspired from the experiment by Passelègue *et al.* (2018, 2020). We consider a cylindrical rock sample of 40 mm in width and 100 mm in height, which is cut into two separated halves by a thorough crack with an angle of 60 degrees from the horizontal to simulate the pre-existing fault (Fig. 4.1a). Afterward, we mesh the specimen by setting the distance of the nodes in the model as 2 mm from each other. The FE mesh contains 26400 nodes and 23522 8-node elements, whose type is 3D stress C3D8 (8-node linear brick). After meshing the whole sample, we

assign the model with the mechanical properties listed in Table 4.1. We chose an effective Young's modulus that accounts for the stiffness of the loading frame, as shown in Chapter 3. This required a calibration test, detailed in Chapter 3.

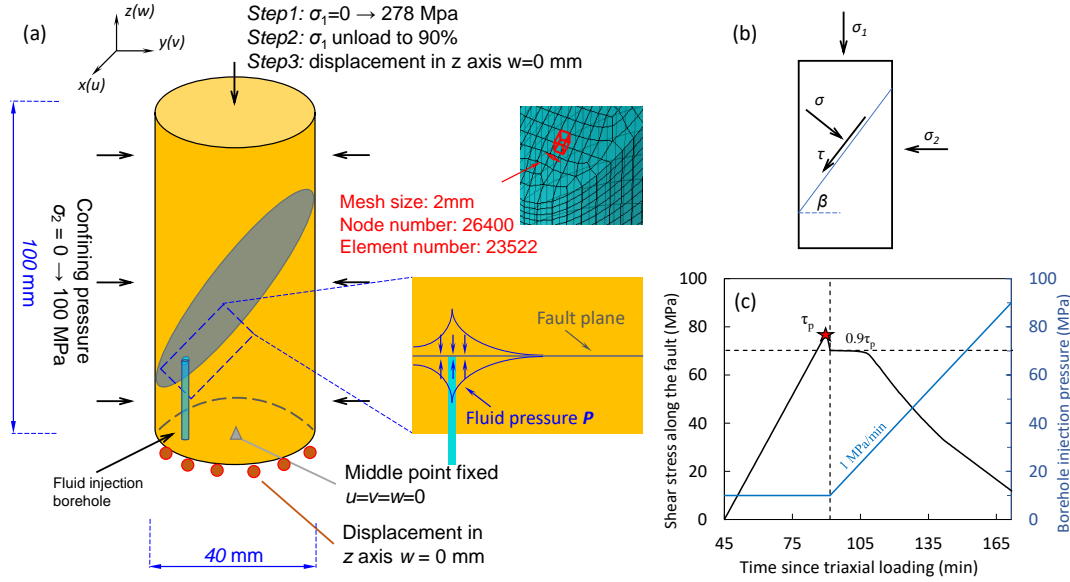


Figure 4.1: Experimental setup modeled in this study. **a** Configuration of the 3D finite element model under triaxial loading. The fault is injected by fluid through a borehole whose center is at 4.5mm from the edge of the sample. Mesh size: 2mm, node number: 26400 and element number: 23522. **b** Schematic model of rock sample with a plane of weakness with outward normal vector oriented at angle  $\beta$  to the direction of maximum principal stress  $\sigma_1$ .  $\sigma_2$  is the minimum principal stress and  $\sigma$ ,  $\tau$  are the normal and shear stress along the fault plane. **c** The shear stress evolution and borehole injection pressure change of the numerical model during triaxial loading and fluid injection.

The loading of the pre-fractured specimen is inspired from the shear stress state of the triaxial compression fluid injection experiment (Passelègue *et al.*, 2018) (Fig. 4.1b). The shear stress  $\tau$  and normal stress  $\sigma$  on the fault are given by:

$$\begin{aligned}\sigma &= \frac{1}{2}(\sigma_1 + \sigma_2) + \frac{1}{2}(\sigma_1 - \sigma_2)\cos 2\beta \\ \tau &= -\frac{1}{2}(\sigma_1 - \sigma_2)\sin 2\beta\end{aligned}\quad (4.1)$$

where  $\sigma_1$  is the maximum principal stress and  $\sigma_2$  is the minimum principal stress and the plane of weakness is oriented at an angle  $\beta = 60^\circ$  to the direction of the minimum principal stress ( $\sigma_2$ ). Initially, the fault is saturated with a fluid with the pressure  $P_0 = 10$  MPa, so that the effective normal stress is  $\sigma' = \sigma - P_0$ . Based on the known peak shear stress  $\tau_p = \tau = 78$  MPa (Fig. 4.1c), constant confining pressure  $\sigma_2 = 100$  MPa and initial fluid pressure 10 MPa from the experiment, the axial loading  $\sigma_1 = 278$  MPa is calculated from equation (4.1). The loading process consists of a stress relaxation test (Passelègue *et al.*, 2018) including the following phases (Fig. 4.1a):

- (1)  $\sigma_1$  and  $\sigma_2$  increase from 0 to 100 MPa.
- (2) Apply an initial water pressure  $P_0$  of 10 MPa on the fault interface. The confining pressure  $\sigma_2$  maintains constant at 100 MPa and  $\sigma_1$  increases from 100 to 278 MPa. The onset of the fault occurs when  $\sigma_1$  reaches 278 MPa and the peak shear stress  $\tau_p = 78$  MPa.
- (3)  $\sigma_1$  reduces to make shear stress of the fault  $\tau = 90\% \cdot \tau_p$ . Then the fluid pressure at the borehole begins to increase from 10 MPa to 90 MPa at a certain injection rate and the displacement on the top of the fractured specimen along  $z$  direction  $w = 0$  mm.

Table 4.1: Mechanical properties of the finite element model

Properties	Values
Young's modulus	30 GPa
Density	2.8 g/cm <sup>3</sup>
Poisson ratio	0.27
Element type	3D stress C3D8
Mesh size	2 mm
Node number	26400
Element number	23522

The boundary conditions for the model domain, illustrated in Figure 4.1c, are defined as follows: The displacement in the Z-axis is fixed at  $w = 0$  mm at the bottom, and the middle point is fixed  $u = v = w = 0$ . Fig. 4.1 gives a schematic view of the 3D finite element model with the geometry, triaxial loading and boundary conditions.

### 4.2.2 Governing equations

Within the two sample blocks, we assume a purely elastic behavior. The governing equations and the Navier Equations (Constantin and Foias, 2020; Jaeger *et al.*, 2009), integrating the equations of static stress equilibrium, strain-displacement equations and the constitutive equations (Hookes law), expressing all these components in terms of displacements(Clough, 1990; Hooke, 1678; Love, 2013; Muskhelishvili *et al.*, 1953):

$$\begin{aligned}
& \lambda \left( \frac{\partial^2 u}{\partial x^2} + \frac{\partial^2 v}{\partial x \partial y} + \frac{\partial^2 w}{\partial x \partial z} \right) + G \left( \frac{\partial^2 u}{\partial x^2} + \frac{\partial^2 v}{\partial x \partial y} + \frac{\partial^2 w}{\partial x \partial z} \right. \\
& \quad \left. + \frac{\partial^2 u}{\partial x^2} + \frac{\partial^2 u}{\partial y^2} + \frac{\partial^2 u}{\partial z^2} \right) + F_x = 0 \\
& \lambda \left( \frac{\partial^2 u}{\partial x \partial y} + \frac{\partial^2 v}{\partial y^2} + \frac{\partial^2 w}{\partial y \partial z} \right) + G \left( \frac{\partial^2 u}{\partial x \partial y} + \frac{\partial^2 v}{\partial y^2} + \frac{\partial^2 w}{\partial y \partial z} \right. \\
& \quad \left. + \frac{\partial^2 v}{\partial x^2} + \frac{\partial^2 v}{\partial y^2} + \frac{\partial^2 v}{\partial z^2} \right) + F_y = 0 \\
& \lambda \left( \frac{\partial^2 u}{\partial z \partial x} + \frac{\partial^2 v}{\partial z \partial y} + \frac{\partial^2 w}{\partial z^2} \right) + G \left( \frac{\partial^2 u}{\partial z \partial x} + \frac{\partial^2 v}{\partial z \partial y} + \frac{\partial^2 w}{\partial z^2} \right. \\
& \quad \left. + \frac{\partial^2 w}{\partial x^2} + \frac{\partial^2 w}{\partial y^2} + \frac{\partial^2 w}{\partial z^2} \right) + F_z = 0
\end{aligned} \tag{4.2}$$

where  $u$ ,  $v$  and  $w$  are the displacement in  $x$ ,  $y$  and  $z$  directions,  $G$  is shear modulus,  $\lambda = 2G\nu/(1 - 2\nu)$  is the Lamé parameter (here  $\nu$  is Poisson ratio),  $F_x$ ,  $F_y$  and  $F_z$  are the body force in  $x$ ,  $y$  and  $z$  directions. The FEM is used in engineering to solve Navier equations with complex geometries, loads, or boundary conditions. In this study, the ABAQUS software (Abaqus *et al.*, 2019) is used to perform the FEM analysis, solving the resulting algebraic equations for unknown nodal displacements under static conditions.

On the fault, we used slip-weakening friction law following the experimental and in-situ observations of the dependence of friction properties on slip distance (Ida, 1972; Palmer and Rice, 1973; Scholz, 1988). A user-defined friction law is applied by the FRIC subroutine in Abaqus to simulate the contact problem of the fault zone. The linearly weakening friction coefficient dependent on displacement is as follows

$$\mu = \begin{cases} \frac{\mu_d - \mu_s}{d_c} \xi + \mu_s, & (\xi < d_c) \\ \mu_d, & (\xi \geq d_c) \end{cases} \tag{4.3}$$

where  $\mu_s$  is the static friction coefficient, whose value is determined from the onset of fault slip in the laboratory experiment (Passelègue *et al.*, 2018) to be 0.578,  $\mu_d$  is the dynamic friction coefficient,  $\xi$  is the relative displacement along the fault. After reaching the sliding threshold  $d_c$ , the friction coefficient remains constant. Based on the experimental measurements by Marone *et al.* (1991) and in-situ injection experiments (Guglielmi *et al.*, 2015b), four  $d_c$  values 0.25, 0.3, 0.35, 0.4 mm will be taken in our study, and dynamic friction coefficient  $\mu_d$  ranges from 0.33 to 0.53.

According to fault stability in earthquake mechanics (Scholz, 2019) and theoretical and numerical studies (Cappa *et al.*, 2019; Gischig, 2015; McClure and Horne, 2011), the fault remains stable and aseismic when the rupture length  $L$  does not exceed the critical nucleation length  $L_c$ , but when the accelerating aseismic slip exceeds  $L_c$ , the fault becomes unstable and exhibits seismic slip. The critical nucleation length  $L_c$  is given by

$$L_c = \frac{Gd_c}{\sigma_n(\mu_s - \mu_d)} \quad (4.4)$$

where  $\sigma_n$  is the effective normal stress on the fault. To focus on aseismic slow slip instead of dynamic earthquakes, we select frictional parameters in our quasi-static model to ensure that the critical nucleation length  $L_c$  remains higher than the sample fault length  $L$ . With the frictional parameters above, we obtain the  $L_c$  ranging between 94 mm and 336 mm. The sample length  $L = 80 \text{ mm} < L_c$  ensures the fault stability and the slip remains aseismic.

The governing equation of the pore pressure distribution on the fault is the diffusion equation, which is derived from the conservation of mass for the pore fluid and Darcy's law (Jaeger *et al.*, 2009). The boundary condition of the diffusive fault is that no liquid is allowed to flow outside the fault plane (Homogeneous Neumann boundary condition). The spatio-temporal fluid diffusion equation along the fault is given by

$$\frac{\partial p(x, y, t)}{\partial t} = D \nabla^2 p(x, y, t) \quad (4.5)$$

where  $p(x, y, t)$  is evolving fluid pressure along the 2D fault plane at time  $t$ ,  $\nabla^2 = (\frac{\partial^2}{\partial x^2}, \frac{\partial^2}{\partial y^2})$  is the Laplacian operator. The hydraulic diffusivity  $D$  is given by

$$D = \frac{k}{\phi\mu(C_f + C_p)} \quad (4.6)$$

where  $k$  is permeability,  $\phi$  is porosity,  $\mu$  is the viscosity and  $C_f$ ,  $C_p$  are the compressibility of the pore fluid and pore volume whose values are  $4.6 \cdot 10^{-10} \text{ Pa}^{-1}$  and from

$\sim 1 \cdot 10^{-9}$  to  $\sim 1 \cdot 10^{-11} \text{ Pa}^{-1}$  (Ojala and Grande, 2022; Walsh, 1965; Wong *et al.*, 1989), respectively. Recent injection researches on the cracked region suggest the value of fluid diffusivity  $D = (7 \pm 1) \times 10^{-5} \text{ m}^2 \cdot \text{s}^{-1}$  in the fault damage zone (Cappa *et al.*, 2006; Doan *et al.*, 2006; Guglielmi *et al.*, 2008). In this study, we investigate the influence of fluid diffusivity on fault reactivation behavior by utilizing various hydraulic diffusivity values within the order of  $1 \times 10^{-5}$  to  $1 \cdot 10^{-6} \text{ m}^2 \cdot \text{s}^{-1}$ . The fluid pressure is controlled at the injection borehole as shown in Fig. 4.1c. The solution to the fluid diffusion equation (4.3) is obtained using a solver developed by Almakari *et al.* (2020; 2019) through the Forward Time Central Space (FTCS) explicit finite difference approach.

The calibration of our model based on the laboratory injection experiments by Passelègue *et al.* (2018) is shown in Chapter 3. To conduct further research, we will carry out three groups of numerical tests. In the first group, we will maintain a fixed initial stress state of 90%  $\tau_p$ , a confining pressure of 100 MPa, dynamic friction  $\mu_d = 0.5$ , and critical sliding distance  $d_c$  of 0.35 mm. By varying the hydraulic parameters, we will investigate the mechanical behavior of pre-cracked samples under three different hydraulic diffusivity values:  $D = 5 \cdot 10^{-5} \text{ m}^2/\text{s}$ ,  $1 \cdot 10^{-5} \text{ m}^2/\text{s}$ , and  $5 \cdot 10^{-6} \text{ m}^2/\text{s}$ . We will also test injection rates ranging from 1 to 1000 MPa/min under each hydraulic diffusivity. The second group will focus on manipulating the initial stress state while holding other parameters constant, specifically by varying the initial shear stress from 50% to 90% of  $\tau_p$  prior to the increase in fluid injection pressure. The third group will simulate changes in friction parameters by varying only the critical sliding distance  $d_c$  vary with 0.25, 0.30, 0.35 and 0.40 mm and residual friction coefficient  $\mu_d$  from 0.33 to 0.53. Through conducting these three groups of injection experiments, we will explore the impact of hydraulic, stress state, and frictional parameters on sliding behavior, stress performance, and rupture propagation speed on the fault. Additionally, we aim to examine the correlation between aseismic moment evolution, total fluid injection volume, and the aforementioned parameters.

### 4.3 Effect of hydraulic parameters

In this part, we show the results of the numerical simulation of the laboratory scale fluid injection-induced fault reactivation tests. The complete solution to the diffusion equation (4.5) is the diffusive fluid pressure at discrete nodes along the fault plane. The results are two-dimensional within an elliptical interface of 40 mm in width and 80 mm in length due to the shape of the cylinder sample and fault plane.

Fig. 4.2 shows the finite difference solution to equation (4.5). Here we define the fault plane's elliptical long axis as the X-axis and the endpoint close to the injection borehole as the origin of the axis. In Fig. 4.2 are fluid pressure map histories over the fault plane under the injection rates of 100 and 1000 MPa/min. Here we used a constant hydraulic diffusivity  $D = 1 \cdot 10^{-5} \text{ m}^2/\text{s}$ . It is obvious from the figure that under a higher injection rate, the pore pressure is more concentrated close to the borehole.

We apply the pore pressure solutions in Abaqus as a boundary condition on the fault. The pore pressure is used as an effective normal stress in the model. We vary injection rates between 1, 10, 100, and 1000 MPa/min to study how the injection rate influences fault reactivation. Meanwhile, the injection rates are under different diffusivities:  $5 \cdot 10^{-5} \text{ m}^2/\text{s}$ ,  $1 \cdot 10^{-5} \text{ m}^2/\text{s}$ , and  $5 \cdot 10^{-6} \text{ m}^2/\text{s}$ .

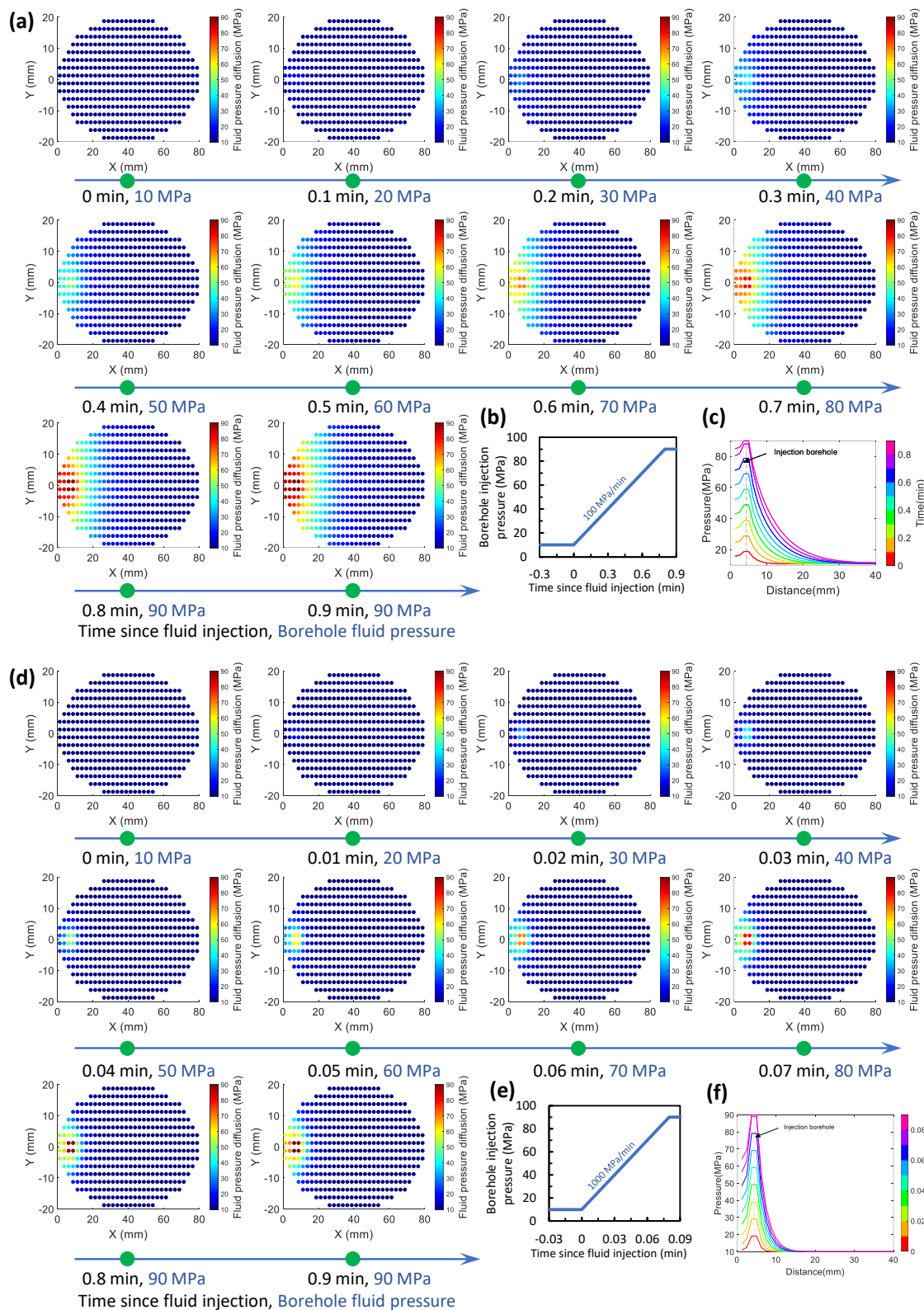


Figure 4.2: **a, d** Fluid pressure evolution with time on the 2D fault ellipse under the injection rates of 100MPa/min and 1000 MPa/min. The pressure is plotted with every injection pressure increase of 10 MPa. Hydraulic diffusivity  $D = 1 \cdot 10^{-5} \text{ m}^2/\text{s}$ . **b, e** Schematic borehole injection pressure history of two injection rates. **c, f** Diffusive pore pressure history along the fault plane's long axis under different injection rates. Red lines indicate the center of the injection hole ( $x = 4.5 \text{ mm}$ ).

In Fig. 4.3 and Fig. 4.4, we display the fault slip and shear stress evolution on the fault under two different injection rates (i.e. for the pore pressure shown in Fig. 4.2). The hydraulic diffusivity of both simulations is  $1 \cdot 10^{-5} \text{ m}^2/\text{s}$ . The evolution of displacement and shear stress on the 2D elliptical fault every 6 seconds are shown in Fig. 4.3, under the injection rate of 100 MPa/min. Fig. 4.4 shows a 1000 MPa/min injection rate and the evolution of stress and slip every 0.6 seconds. The figures give an intuitive and detailed view of how stress and slip propagate. An aseismic slip event nucleates around the borehole and propagates in the  $X$  and  $Y$  directions. This aseismic slip is associated with a shear stress drop in the slipping region. Shear stress is redistributed to the other parts of the fault. The propagation speed of the shear stress front and slip front at 100 MPa/min is 81.75 m/d and that at 1000 MPa/min is 103.20 m/d. At the lower injection rate, both the shear stress front and fault slip front propagate slower than that under higher injection rates. The value of average shear stress drop at 100 and 1000 MPa/min are 12.630 MPa and 1.230 MPa, and fault displacement under these two injection rates are 0.199 mm and 0.102 mm. We observe a trend that the shear stress drop and fault displacement under lower injection rates are more prominent than that under higher injection rates. Comparing the stress and slip front propagation in Fig. 4.3 with the fluid pressure front evolution in Fig. 4.2a, we find that both shear stress and fault slip propagates faster and further than the pressure front.

In Fig. 4.3c and 4.4c, we plot the shear stress and slip profiles along the fault to figure out why a higher injection rate induces lower fault slip. We pick the stress and slip data along the long axis (dashed line on the fault plane) of the fault ellipse and project it into the  $X$ -axis (schematic diagram of the ellipse section in Fig. 4.3c and 4.4c). The profiles are from 0 to 40 mm along the fault. Note that the slip rates of the fault in this set of injection tests range in the order of mm/day, which is direct evidence of induced aseismic slip.

Under the 1000 MPa/min injection rate (Fig. 4.4c), pore fluid pressure is more concentrated around the injection hole ( $x=4.5\text{mm}$ ) during the process of fluid injection. This pressure concentration induces the shear stress concentration and causes the fault slip around the injection hole higher than faraway points. While under a lower injection rate of 100 MPa/min (Fig. 4.3c), when the injection pressure reaches 90 MPa, a longer injection time leads to a larger pressurized area than the 1000 MPa/min injection rate. This larger fluid-pressurized area induces a larger slip area and thus a higher fault displacement, under constant stress drop.

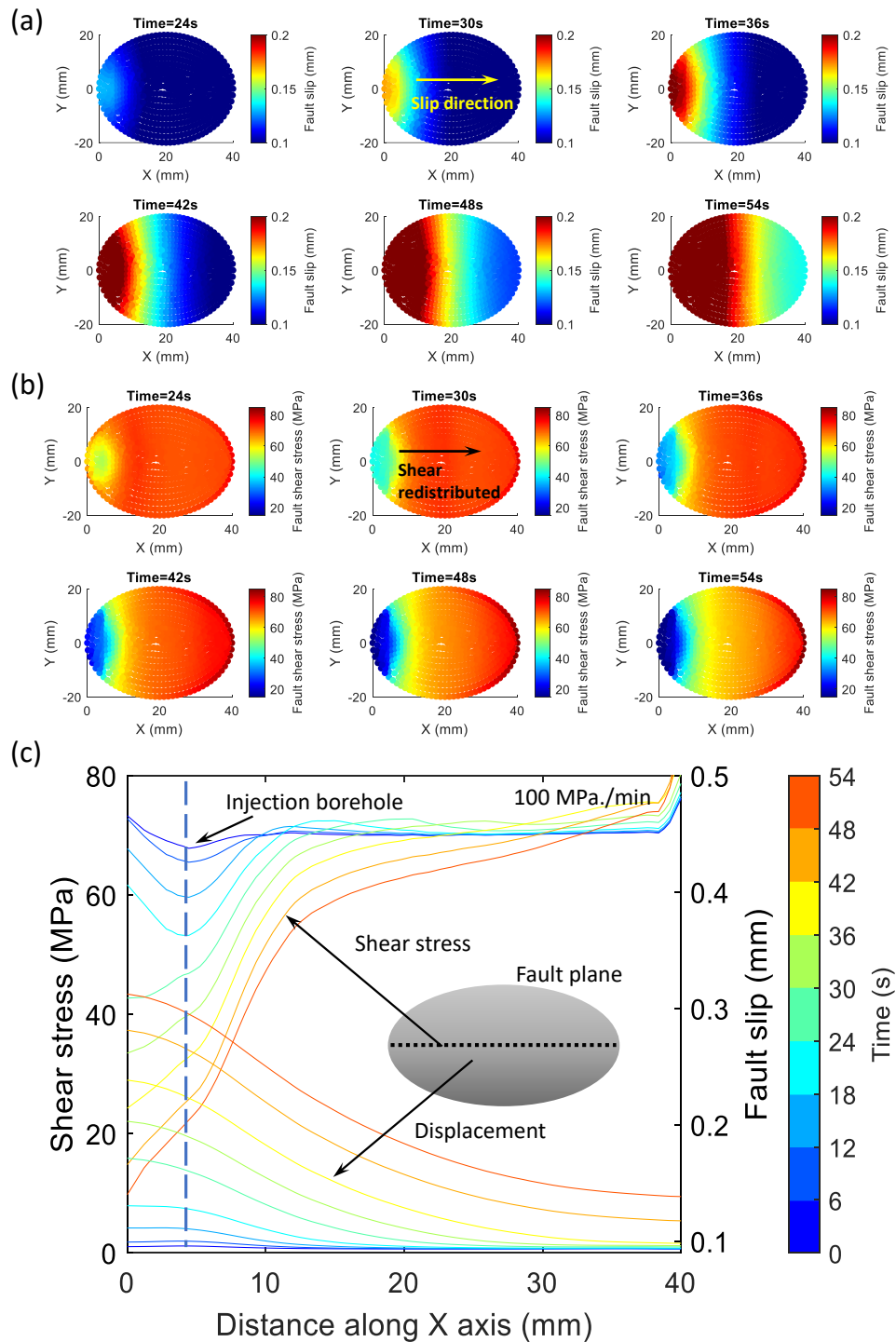


Figure 4.3: **a** Slip evolution histories on the fault after the increase of fluid injection pressure with the rate of 100 MPa/min. **b** Shear stress evolution histories on the fault after the increase of fluid injection pressure with the rate of 100 MPa/min. **c** Evolution of shear stress and slip in fault profile with time. Hydraulic diffusivity is  $1 \cdot 10^{-5} \text{ m}^2/\text{s}$ . Time since the start of fluid injection is indicated in the subfigure's title.

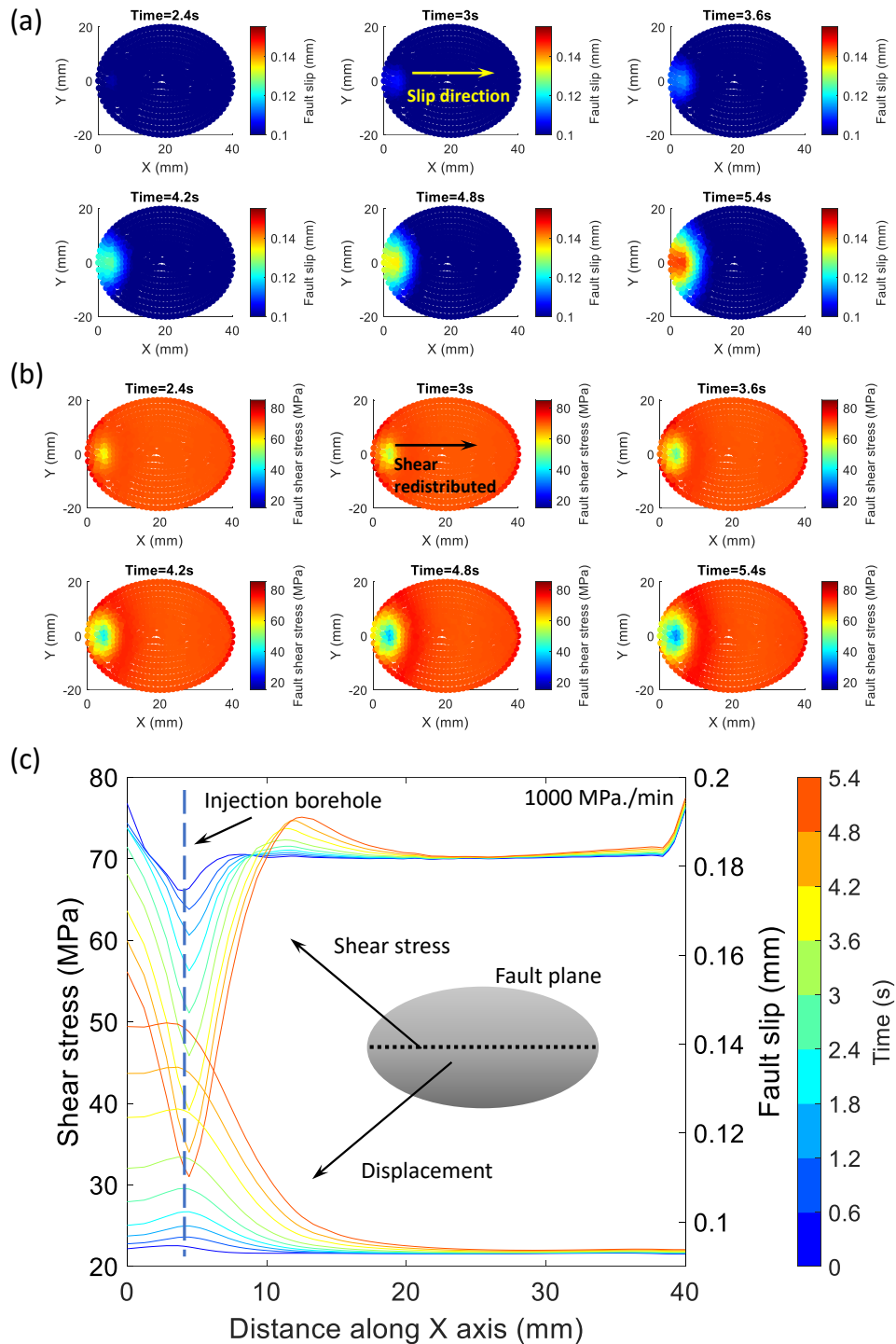


Figure 4.4: **a** Slip evolution histories on the fault after the increase of fluid injection pressure with the rate of 1000 MPa/min. **b** Shear stress evolution histories on the fault after the increase of fluid injection pressure with the rate of 1000 MPa/min. **c** Evolution of shear stress and slip in fault profile with time. Hydraulic diffusivity is  $1 \cdot 10^{-5} \text{ m}^2/\text{s}$ . Time since the start of fluid injection is indicated in the subfigure's title.

Fig. 4.5a shows the maximum displacement of the fault under different injection rates and hydraulic diffusivity. The results indicate that the maximum slip of the fault has a decreasing trend as the injection rate increases. With the injection rate of 1 MPa/min, maximum displacement ranges between 0.617 and 0.6822 mm. When the injection rate reaches 1000 MPa/min, the maximum slip decreases from around 0.65mm to 0.126-0.285 mm. A similar trend is observed in all groups of hydraulic diffusivity.

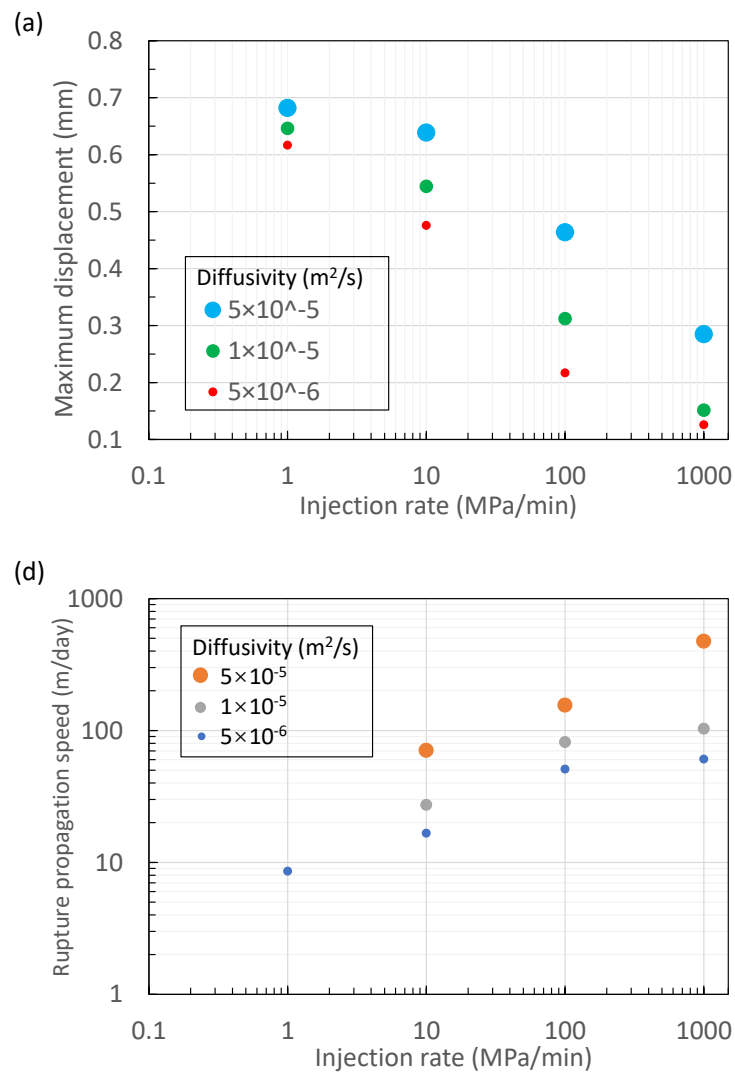


Figure 4.5: **a** Relationship between maximum displacement and injection rate under three groups of hydraulic diffusivity. **b** Rupture propagation speed against injection rate and hydraulic diffusivity.

In our numerical simulation, we observe shear stress migration along the fault ellipse from the stress map (Fig. 4.3b and 4.4b) and profile (Fig. 4.3c and 4.4c) evolving with time. Therefore, we consider estimating the rupture propagation speed from stress migration. Here we assume that the migrating shear stress peak indicates the aseismic slip front (or rupture propagation front). The distance of the shear stress peak from the end of the fault plane is the rupture length. Rupture propagation

speed is estimated by the shear peak migration speed.

Fig. 4.5d shows the rupture propagation speed  $V_r$  under the injection rate at 1, 10, 100 and 1000 MPa/min, along with hydraulic diffusivity at  $5 \cdot 10^{-5} \text{ m}^2/\text{s}$ ,  $1 \cdot 10^{-5} \text{ m}^2/\text{s}$ , and  $5 \cdot 10^{-6} \text{ m}^2/\text{s}$ . Results show that  $V_r$  ranges from 8.5824 m/day to 475.2 m/day. We find that the speed increases with the injection rate under the same hydraulic diffusivity. A higher hydraulic diffusivity at the same injection rate results in a higher rupture propagation speed. The rupture propagation speed is dependent both on injection rate and hydraulic diffusivity.

## 4.4 Effect of stress state

In this subsection, we will study how the stress state influences the reactivation of fault slip, including initial stress and confining stress. First, the initial shear stress at the beginning of fluid injection will be controlled from  $90\%\tau_p$  to  $50\%\tau_p$ .  $\tau_p$  is the peak shear stress at the onset of fault activation. Second, the confining pressure of the fault sample will be decreased from 100 MPa to 50 MPa. We will present the stress and slip results while the stress states change.

### 4.4.1 Initial stress

We investigate how the initial stress state affects fluid-induced fault reactivation behavior. To achieve this, we control the initial shear stress on the fault plane at the beginning of fluid injection by unloading the axial stress. Once the initial shear stress  $\tau_i$  reaches a specific ratio of  $\tau_p$ , the loading cap is held still, and fluid injection begins. We vary the initial shear stress ratio  $\tau_i/\tau_p$  from  $90\%\tau_p$  to  $50\%\tau_p$ , where  $\tau_p = 78 \text{ MPa}$  is the critical peak shear stress at the onset of fault activation (Fig. 4.6a). Throughout the unloading control process, shear stress decreases as slip accumulates, as shown in Fig. 4.6a for the period of 0 to 1.6 minutes. The schematic view of the fluid pressure at the injection borehole with the rate of 10 MPa/min is shown in Fig. 4.6b.

In this set of numerical tests, with various initial stress states, the injection process is the same: the pressure of the injection borehole was from 10 to 90 MPa at the rate of 10 MPa/min and kept still at 90 MPa for 1 min (Fig. 4.6b). We find that higher initial stress causes the fault to be reactivated at an earlier injection time and induces a larger maximum fault slip (Fig. 4.6a and 4.6d). Aside from the fault reactivation and maximum fault slip, the curves depicting crack propagation shift

towards earlier fluid injection times as the initial stress ratio increases, indicating the impact of initial stress on the onset of rupture propagation. Higher initial stress (fault close to failure) nucleates an aseismic slip even sooner since the pore pressure needs to increase more at a lower initial shear stress ratio  $\tau_i/\tau_p$ . The Mohr-Coulomb envelope in Figure 4.6c also accounts for the reactivation of crack propagation. Lower effective normal stress along the fault can trigger the initiation of rupture opening under a lower initial stress ratio. Fig. 4.6e demonstrates the influence of the initial stress ratio  $\tau_i/\tau_p$  on the maximum fault slip. The maximum fault slip induced by fluid injection ranges from 0.1536 mm to 0.476 mm.

It can be seen from the average stress and slip diagram that with the increase of initial stress, the reactivation produces more slip. This is reflected in the larger sliding distance (0.359 - 0.405 mm with 85% - 90% $\tau_p$ ). Another indication is that under low initial stress, fault reactivation occurs later, which leaves time for pressurization (Fig. 4.6a and 4.6d). The initiation of fault slip is at a borehole fluid pressure of  $\sim 40$  MPa under 90% initial stress, while under 50% $\tau_p$  initial stress, the fault is reactivated at  $\sim 80$  MPa. This trend is also observed in the laboratory experiment (Passelègue *et al.*, 2018). See also from the Mohr-Coulomb diagram (Fig. 4.6b), under a lower initial stress ratio the fault requires a lower effective normal stress to be reactivated, which is induced by a higher mean pore pressure along the fault.

Fig. 4.6d and 4.6e show the rupture propagation speed  $V_r$  versus the initial stress ratio and the rupture length evolution with time under different initial stresses.  $V_r$  is 0.8777 m/day when initial stress is 50% $\tau_p$ , and the speed reaches 16.643 m/day when initial stress is 90%. From Fig. 4.6e, we find that the rupture propagation speed increases with  $\tau_i/\tau_p$ . Theoretical studies of injection-induced earthquake nucleation also reveal the same dependence on the stress state (Dublançhet, 2019; Garagash and Germanovich, 2012; Viesca and Rice, 2012; Wynants-Morel *et al.*, 2020). The pre-injection stress state may influence the aseismic propagation of a rupture front relative to fluid migration (Garagash and Germanovich, 2012). Fig. 4.6d shows the rupture length evolution with time since fluid injection under different initial stress ratios, where rupture propagation speed weakens with a lower initial stress ratio.

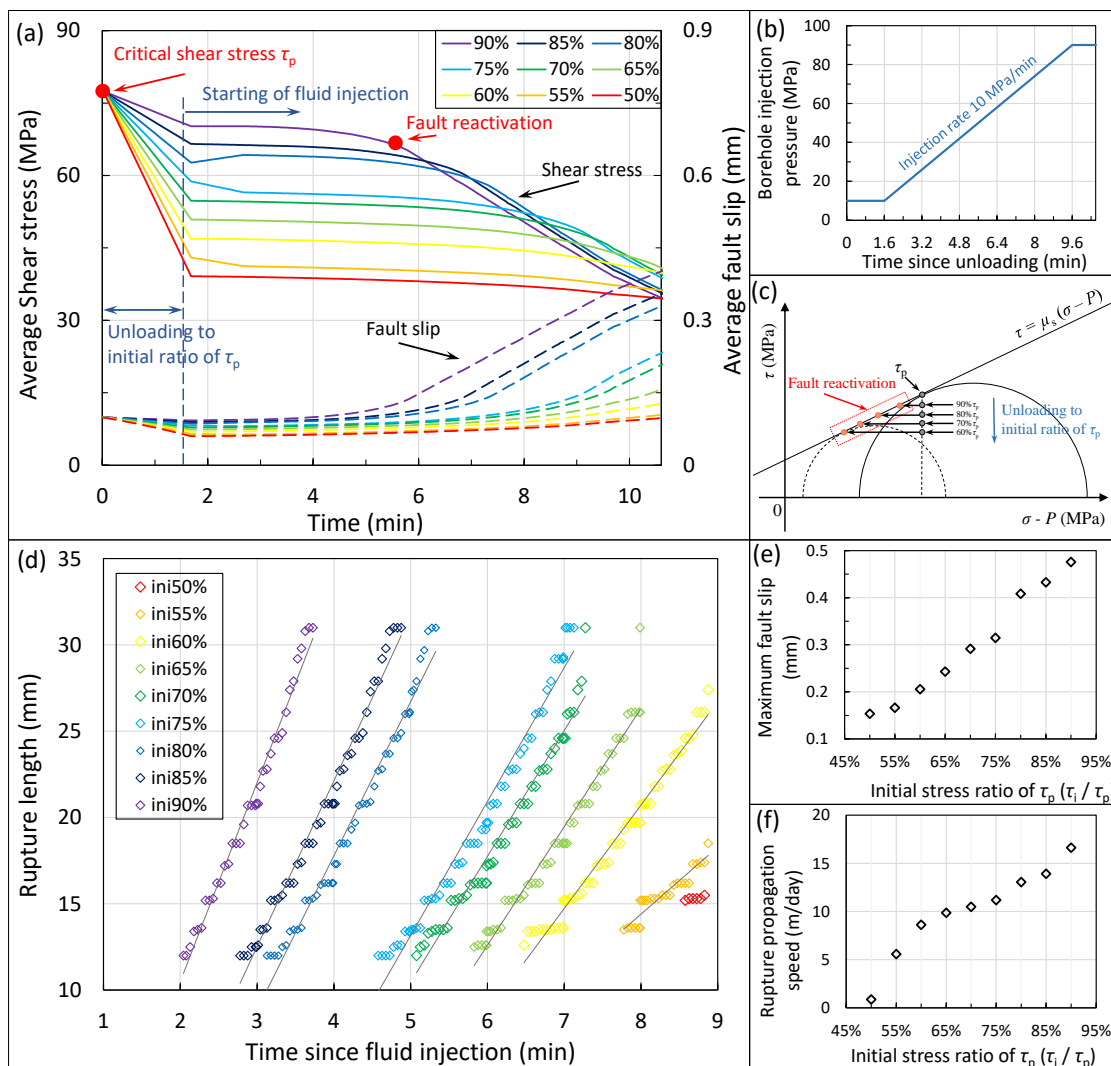


Figure 4.6: Effect of initial stress ratio ( $\tau_i/\tau_p$ ) on injection tests. **a** Average shear stress and slip displacement along the fault versus time with initial stress ratio ranging from 90% to 50%. The injection rate is 10 MPa/min. Hydraulic diffusivity =  $5 \cdot 10^{-6} \text{ m}^2/\text{s}$ . **b** Schematic borehole injection pressure history. **c** Mohr-Coulomb diagram interpreting the reactivation of fault with different initial stress ratios. **d** Rupture length evolution with time under different initial stress ratios. The time is since fluid injection from 0-9 min. **e** Maximum fault slip versus initial stress ratio with initial stress ranging from 90% to 50%. **f** Rupture propagation speed  $V_r$  with initial stress ratios ranging from 90% to 50%.

### 4.4.2 Confining stress

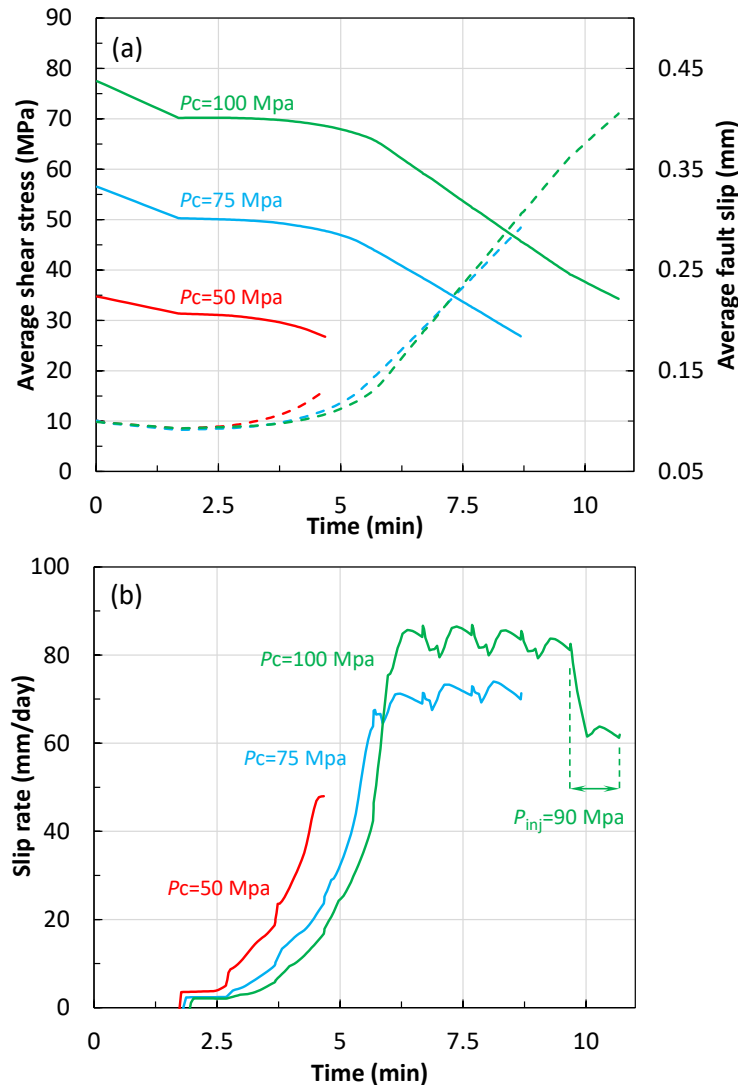


Figure 4.7: (a) Average shear stress and fault slip numerical evolution with time under the confining pressure  $P_c = 100, 75$  and  $50$  MPa. Solid lines are shear stress and dashed lines are fault slips. The injected pore fluid was at a constant pressure rate of  $10$  MPa/min, targeting  $90, 70$  and  $40$  MPa when  $P_c = 100, 75$  and  $50$  MPa. (b) Fault average slip rate.

After the numerical tests of initial stress, we are now presenting the results of simulations with different confining pressures. The experimental scale sample with

pre-existing fault under the confining pressure of 100, 75, and 50 MPa was modeled. Fig. 4.7 (a) shows the average shear stress and fault slip evolution with time. Here solid lines are average shear stress, and the solid is fault slip. Apart from two confining pressure  $P_c = 100$ MPa and 50 MPa, where fluid injection pressure targeted up to 90 MPa and 40 MPa as in the experiment (Passelègue *et al.*, 2018), we operated a test under confining pressure  $P_c = 75$  MPa with pore pressure up to 70 MPa. In this  $P_c = 75$  MPa test, we continued the fluid injection after it reached the limitation of 70 MPa, and the injection termination was pore pressure  $P_{pore} = 90$  MPa. Fig. 4.7 (b) demonstrates the corresponding average slip rate (mm/day) under different confining pressures. This group of numerical tests is designed to explore how confining pressure influences fluid-injection-induced fault slip behavior.

With different confining stress at 100, 75 and 50 MPa, the critical axial pressure at the onset of fault slip is respectively 278, 205 and 130 MPa, resulting in the critical shear stress  $\tau_p = 77.47, 56.52$  and 34.74 MPa in these tests (shear stress at Time = 0 min in Fig. 4.7 (a)). After the shear stress decreased to 90% $\tau_p$  (Time = 1.6 min), pore pressure started to increase. The numerical results show that the average fault slip and shear stress drop are higher after fluid injection under high confining pressure. While under lower confining pressure, the fault has a higher sliding value at the initial stage (1.6 - 7.2 min in Fig 4.7 (a)) of water injection. Combined with the slip rate results in Fig. 4.7 (b), we find that lower confining pressure stimulates higher initial sliding velocity. The sliding speed under high confining pressure can reach a higher value with the increased fluid pressure. The reactivation of fault slip is the same, independent of the confining pressure. After the injection pressure at the borehole reached 90 MPa, the fluid pressure was kept constant at 90 MPa for 1 min. The slip rate figure shows that the fault continued to slide, but the slip rate dropped (9.6 - 10.6 min in Fig. 4.7 (b)).

## 4.5 Effect of frictional parameters

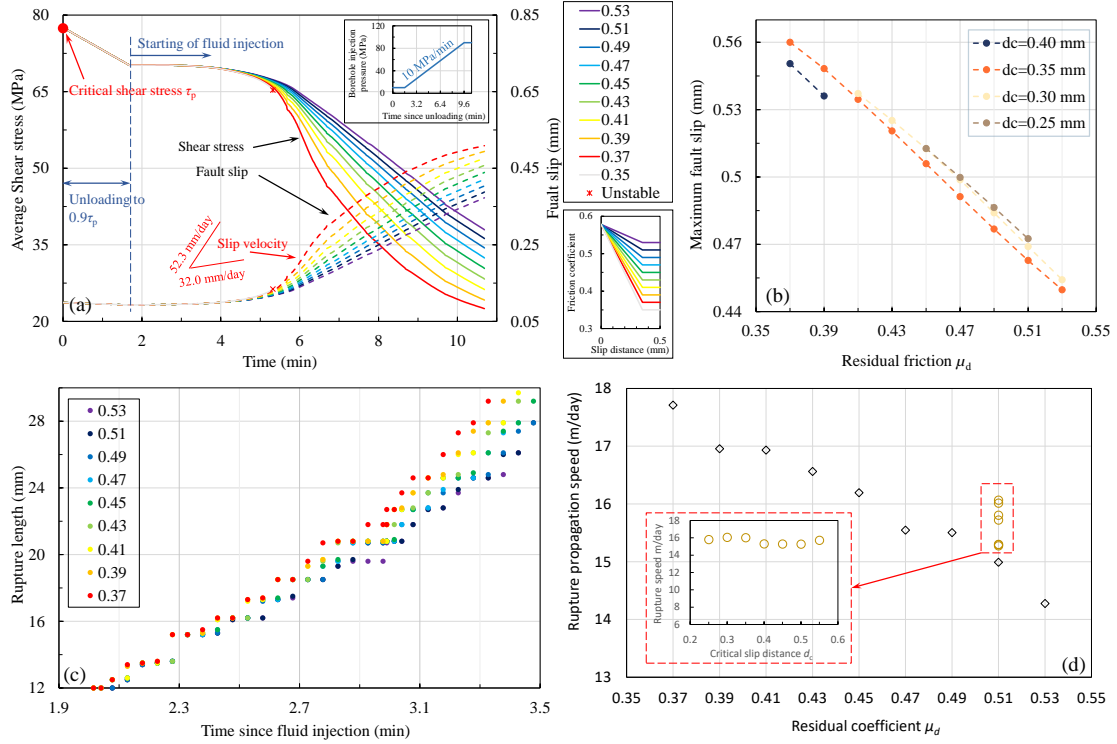


Figure 4.8: **a** Average shear stress and fault slip evolution with time under residual friction coefficient  $\mu_d$  from 0.35 to 0.53. Static friction coefficient  $\mu_s = 0.578$ , critical slip distance  $d_c = 0.35$  mm. The injection rate is 10 MPa/min. The weakening friction coefficient dependent on slip distance is shown in right down. **b** Maximum fault slip versus the residual friction coefficient  $\mu_d$  for different values of critical slip  $d_c$ .  $\mu_d$  ranges between 0.35 and 0.55, and the static friction coefficient  $\mu_s$  here is 0.578. The critical sliding distance  $d_c = 0.25, 0.30, 0.35,$  and  $0.40$  mm. **c** Rupture length evolution with time under different  $\mu_d$ . The time is after the fluid injection begins.  $d_c = 0.35$  mm. **d** Rupture propagation speed  $V_r$  versus the residual friction coefficient  $\mu_d$ .  $\mu_d$  ranges between 0.35 and 0.55, and the static friction coefficient  $\mu_s$  here is 0.578. The critical sliding distance  $d_c = 0.35$  mm.

Finally, we will examine the slip-weakening friction law used in our finite element model, which is consistent with the earthquake nucleation theory to ensure fault

stability and aseismicity (Scholz, 2019). Our focus is on investigating the influence of frictional parameters, such as the critical slip distance  $d_c$  and residual friction  $\mu_d$  (dynamic friction coefficient), on the slip behavior of the fault induced by fluid injection.

The average shear stress and slip evolution resulting from the parametric study of the residual friction  $\mu_d$  are presented in Fig. 4.8a. In this group of numerical tests, the critical sliding distance  $d_c$  was constant at 0.35 mm.  $\mu_d$  increased from 0.35 to 0.55. The injection rate is 10 MPa/min. The maximum slip dependence on  $\mu_d$  and  $d_c$  is shown in Fig. 4.8b. Results show that the average fault slip at the termination of fluid injection increase with the decrease of  $\mu_d$ . At a lower dynamic friction coefficient, the slip rate of the fault at the initial stage of reactivation is higher. When  $\mu_d = 0.35$ , the dynamic friction coefficient is too low to stabilize the fault. The model becomes unstable with an accelerating slip rate at the onset of fault reactivation.

Fig. 4.8b shows numerical results of the maximum fault slip versus the residual friction coefficient  $\mu_d$  changing from 0.35 to 0.55. The static friction coefficient was kept constant at 0.578, estimated from the experiment (Passelègue *et al.*, 2018). The tests were conducted in four groups, with the critical sliding distance  $d_c$  ranging between 0.25 mm and 0.4 mm. The results show that the maximum fault slip decreases with the increase of  $\mu_d$ . With the same residual friction coefficient, fault slip is higher under a lower critical sliding distance  $d_c$ . However, compared with  $\mu_d$ ,  $d_c$  has less influence on the fault sliding behavior induced by fluid injection. Fault slip  $\xi$  and shear stress drop  $\Delta\tau$  roughly scale as:  $\xi = GL\Delta\tau$ . The shear stress drop is given by

$$\Delta\tau = \mu_s(\sigma - P_r) - \mu_d(\sigma - P_f) \quad (4.7)$$

where  $P_r$  is fluid pressure at the reactivation of fault slip and  $P_f$  is fluid pressure at the termination of injection. Equation (4.7) explains that the shear stress drop and fault slip decrease with the increase of residual friction  $\mu_d$  as shown in Fig. 4.8b.

Fig. 4.8c shows the rupture length evolution with time since the fluid injection began. Under different dynamic friction coefficients, in all tests, the rupture started propagating at 48.695 - 48.75 min since fluid injection began. The nucleation time is the same whatever  $\mu_d$  because the fluid pressure required for fault reactivation is independent of the kinetic friction coefficient. The results of rupture propagation speed  $V_r$  changing with residual friction coefficient  $\mu_d$  are shown in Fig. 4.8c and 4.8d. The critical sliding distance  $d_c = 0.35$  mm, and the injection rate is 10 MPa/min.

When  $\mu_d$  increases from 0.37 to 0.53,  $V_r$  decreases from 17.71 m/day to 14.27 m/day. In general, rupture propagation speed decreases with an increasing residual friction coefficient  $\mu_d$  but shows no dependence with critical distance  $d_c$  (Fig. 4.8d). We find that the residual friction coefficient influences the slope of rupture length versus time (rupture speed  $V_r$ ). However, the change of  $\mu_d$  has no effect on the reactivation time of rupture propagation. In the earthquake nucleation theory, the theoretical derivation of rupture length also found its dependence on the weakening residual friction (Garagash and Germanovich, 2012; Scholz, 2019; Uenishi and Rice, 2003; Viesca and Rice, 2012). We will discuss the dependence in the following section of this work.

## 4.6 Discussion

In this study, we modeled laboratory-scale injection tests on a saw-cut fault in a Westerly granite sample under triaxial loading conditions. To accurately reproduce the laboratory experiment results, we developed a three-dimensional finite element model that considers the interplay of hydro-mechanical and frictional processes. The results of our numerical simulations highlight the impact of various hydraulic, stress, and friction parameters on the injection test outcomes. In this chapter, we present a comprehensive analysis of our findings.

First, we investigated the effect of hydraulic parameters on the fault reactivation and slip evolution. It was observed that a higher injection rate induced a lower average fault slip and lower stress drop, while lower injection rates induced greater average fault slip. Our results also showed that the pore pressure concentration around the injection hole under a high injection rate causes the shear stress concentration and a smaller fault slip. In terms of hydraulic diffusivity, the results showed that high hydraulic diffusivity leads to a larger maximum slip of the fault, but this effect decreases as fluid injection rate decreases. The average shear stress drop and fault slip were found to increase with hydraulic diffusivity. Maps of slip displacement and shear stress showed that higher hydraulic diffusivity causes the fault to reactivate earlier, with a more uniform distribution of stress and slip along the fault. Shear stress and slip profiles along the long axis of the fault ellipse showed that hydraulic diffusivity influences the propagation and diffusion of fluid pressure, which in turn affects the stress and slip behavior. Lower hydraulic diffusivity leads to slower fluid pressure propagation and higher concentration around the injection borehole, while higher hydraulic diffusivity leads to more uniform pressure and

stress-slip results.

Next, we analyzed the impact of stress state on the fault behavior. The initial shear stress and confining pressure are controlled to investigate their effect on fluid injection-induced fault reactivation behavior. Results show that higher initial stress leads to a more violent fault reactivation behavior, with an earlier activation time and a larger maximum fault slip. Decreasing the confining pressure leads to a decrease in the average shear stress and fault slip during fluid injection. The maximum fault slip and the initiation of the rupture propagation both decrease with decreasing confining pressure. These results indicate that the stress state plays a crucial role in fault reactivation behavior during fluid injection.

Finally, we explored the role of frictional parameters, specifically the residual friction coefficient  $\mu_d$  and critical sliding distance  $d_c$ , on the fault behavior. Results showed that the maximum fault slip decreases with an increase in the residual friction coefficient, while a lower critical sliding distance increases fault slip. The average fault slip at the end of fluid injection increases with a decrease in the residual friction coefficient.

The results of fault slip with the impact of fluid injection, stress state, and friction parameters were discussed in the previous part. In the following discussion, the focus will be on the effect of the above parameters on rupture propagation speed and the relationship between seismic moment and fluid injection volume. The study provides valuable insights into fault reactivation and the role of various physical parameters in controlling fault behavior. These findings can be used to better understand the mechanisms of induced earthquakes and to design more effective risk management strategies for fluid injection activities.

### 4.6.1 Rupture propagation speed

Our numerical simulations estimated the rupture propagation speed based on the migration of shear stress along the fault ellipse. The shear stress peak was assumed as the aseismic slip front, and the rupture propagation speed was estimated by the shear stress peak migration speed. The results of our numerical simulations (Fig. 4.9) suggest that the rupture propagation speed,  $V_r$ , is dependent on several factors, including the injection rate, hydraulic diffusivity, initial stress state, and residual friction coefficient. Our findings indicate that higher values of  $V_r$  are observed for higher injection rates and diffusivities (Fig. 4.9a), and that the initial stress state has

a significant impact on the aseismic propagation of the rupture front, with higher initial stress ratio leading to earlier initiation of the rupture and higher rupture front propagation velocity (Fig. 4.9c), which is consistent with the experimental observation estimating fault rupture front from strain gauge array (Passelègue *et al.*, 2020) and theoretical predictions (Garagash and Germanovich, 2012; Gischig, 2015). Additionally, we found that the residual friction coefficient has a negative impact on  $V_r$ , with speed decreasing as  $\mu_d$  increases (Fig. 4.9d). While the critical slip distance  $d_c$  has no influence on  $V_r$  (Fig. 4.9b).

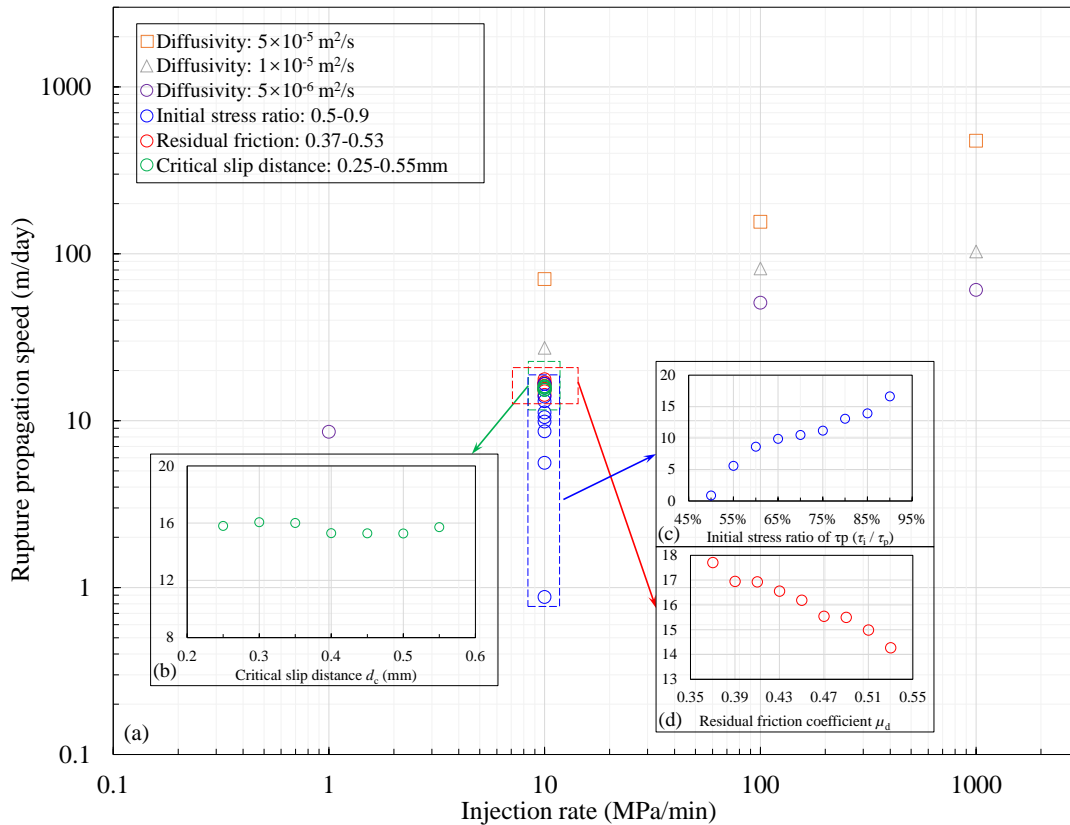


Figure 4.9: Rupture propagation speed (m/day) with different parameters. **a** Injection rate varies between 1 and 1000 MPa/min. Hydraulic diffusivity  $D = 5 \cdot 10^{-5} \text{ m}^2/\text{s}$ ,  $1 \cdot 10^{-5} \text{ m}^2/\text{s}$ , and  $5 \cdot 10^{-6} \text{ m}^2/\text{s}$ . **b** Critical slip distance  $d_c$  range from 0.25 to 0.55 mm. **c** Rupture propagation speed change with initial stress ratio  $\tau_i/\tau_p$  changing from 50% to 90%. **d** Residual friction  $\mu_d$  (dynamic friction coefficient) increases from 0.37 to 0.53.

The rupture front migration speed estimated in our model was found to vary

between the order of m/d to km/d, with the injection rate varying from 1 MPa/min to 1000 MPa/min (Fig. 4.9a). These values are in agreement with observations of aseismic slip propagation on real faults (De Barros *et al.*, 2020; Eyre *et al.*, 2019; Lohman and McGuire, 2007). And more generally, the fluid-induced aseismic slip has been proposed as a plausible mechanism for elucidating the migration dynamics of certain earthquake swarms, as demonstrated in recent research Danré *et al.*, 2022. This finding lends credence to the notion that natural and anthropogenic swarms may share a common driving process. Note that the rupture velocities observed in this study are lower compared to the rupture speeds measured in laboratory experiments during dynamic (stick-and-slip) events, as reported by Passelègue *et al.*, 2020.

Subsequently, we derive an approximate scaling for the rupture propagation speed. According to the linear elastic fracture mechanics (LEFM), the critical fracture energy required to propagate the crack tip under slip weakening friction is  $G_c$  (Freund, 1998; Garagash and Germanovich, 2012; Jaeger *et al.*, 2009; Passelègue *et al.*, 2020; Svetlizky and Fineberg, 2014):

$$G_c = (\mu_s - \mu_d) \frac{\sigma_n d_c}{2} \quad (4.8)$$

To the first order, once the slip patch has reached the fault limits in the  $Y$  direction, the slip event is close to a 2D mode II shear crack (Fig. 4.3a). The elastic energy release rate  $G_r$  on a mode II fracture can be written as:

$$G_r = \frac{K^2}{G} = \frac{\Delta\tau^2 C}{G} \quad (4.9)$$

where  $K \approx \Delta\tau\sqrt{C}$  is the stress intensity factor (SIF) in mode II fracture,  $G$  is the shear modulus of the crack,  $C$  is the crack length and  $\Delta\tau = \tau_i - \tau_r$  is the shear stress drop between initial shear stress  $\tau_i$  and residual shear stress  $\tau_r$  (also see equation (4.7)).

The rupture length  $C$  can be derived from the crack propagation criterion that  $K = K_c$ , where the fracture toughness  $K_c = \sqrt{G_c G} = \sqrt{1/2G(\mu_s - \mu_d)d_c\sigma_n}$  on a model II fracture. The SIF,  $K$ , is a sum of stress intensity and perturbation  $\Delta K$  due to fluid pressurization (Galis *et al.*, 2017; Garagash and Germanovich, 2012):

$$K = \Delta\tau\sqrt{\pi C} + \mu_d \sqrt{\frac{C}{\pi}} \int_{-C}^C \frac{\Delta P}{\sqrt{C^2 - x^2}} dx \quad (4.10)$$

where  $\Delta\tau = (\tau_i/\tau_p)\mu_s(\sigma - P_0) - \mu_d(\sigma - P_0)$  is the shear stress drop between the initial stress state and residual stress state, here  $\sigma$  and  $P_0$  are normal stress and initial fluid pressure on the fault. According to the geometry and injection conditions of the model in this study, we simplify the pressure change integral as follows. The pressure change  $\Delta P$  can be approximately expressed as the following expression:

$$\Delta P = \begin{cases} \beta t(1 - \frac{C}{L_D}) & C > 0 \\ \beta t & -d < C < 0 \\ 0 & C < -d \end{cases} \quad (4.11)$$

where  $\beta$  is the injection rate,  $t$  is the time since fluid injection,  $d = 4.5$  mm is the distance from the center of the injection borehole to the edge of the fault and  $L_D$  is the fluid pressure front length. Then, equation (4.10) can be written as:

$$K = \Delta\tau\sqrt{\pi C} + \mu_d\sqrt{\frac{C}{\pi}}\beta t \left[ \arctan\left(\frac{L_D}{\sqrt{C^2 - L_D^2}}\right) + \arctan\frac{d}{\sqrt{C^2 - d^2}} + \frac{\sqrt{C^2 - L_D^2} - C}{L_D} \right] \quad (4.12)$$

The stability criterion of crack propagation  $K = K_c$  gives a solution of rupture length  $C$ . Fig. 4.10 shows the solution of crack length and rupture propagation speed with this theoretical derivation. In comparison with the numerical simulation presented in Fig. 4.6d and 4.6f, the theoretical solution exhibits a superior level of agreement. Specifically, as the initial stress decreases, the time required for fault reactivation is prolonged and the velocity of crack propagation decreases. It should be acknowledged that some reasonable deviations between the full numerical model and the theoretical solution here arise. However, the results demonstrate consistency in the first-order features between the full numerical solution and the  $K = K_c$  approach.

In conclusion, the numerical simulations suggested that the rupture propagation speed is dependent on several factors, including injection rate, hydraulic diffusivity, initial stress state, and residual friction coefficient, which is consistent with LFM theory. The findings indicate that higher values of rupture propagation speed are observed for higher injection rates and diffusivities. Additionally, the initial stress

state has a significant impact on the aseismic propagation of the rupture front, with a higher initial stress ratio leading to earlier initiation of the rupture and higher rupture front propagation velocity.

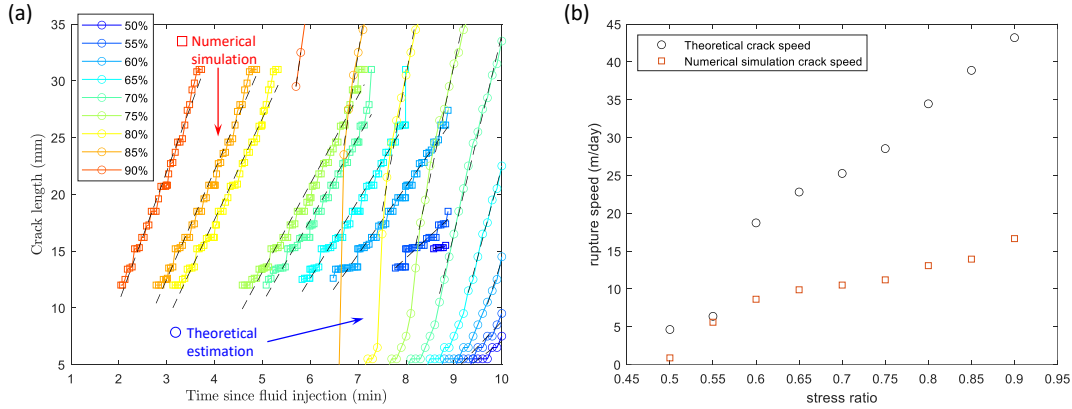


Figure 4.10: Theoretical solution to rupture length and rupture speed as a function of initial stress ratio. **a** Rupture length revolution with time since fluid injection. The initial stress ratio range from 50% to 90%. The injection rate is 10 MPa/min, static friction  $\mu_s = 0.578$ , residual friction  $\mu_d = 0.5$ , critical slip distance  $d_c = 0.35$  mm, hydraulic diffusivity  $D = 5 \cdot 10^{-6}$  m<sup>2</sup>/s. The circular markers represent the theoretical calculation of crack length variation, while the square markers denote the numerical simulation results. **b** Rupture propagation speed as a function of initial stress ratio.

#### 4.6.2 Maximum slip vs. Injection volume

Both induced seismic (Grandin *et al.*, 2017; Grigoli *et al.*, 2018; Keranen *et al.*, 2013; McGarr and Barbour, 2017; Westaway and Burnside, 2019; Yeck *et al.*, 2016, 2017) and aseismic (Sáez *et al.*, 2022) sequences show a dependence of maximum magnitudes and total injection volume. In this study, we investigated the relationship between maximum slip and aseismic moment with injection volume.

Here we describe how the fluid injection volume  $\Delta V$  is obtained from the pore distribution. From a microscopic perspective, the bulk volume of the fault rupture zone  $V_b$  is composed of the volume of the pores  $V_p$  and the volume of the solid  $V_s$ . The total injection volume is the fluid injected into the porous area of the fault rupture zone. Following Jaeger *et al.*, 2009, we define the mass per unit bulk volume

of injected fluid in the fault porous region as  $M$ , which is given by

$$M = \frac{m_f}{V_b} = \frac{m_f}{V_p} \frac{V_p}{V_b} = \rho_f \frac{V_p}{V_b} = \rho_f \phi \quad (4.13)$$

where  $m_f$  is the mass of fluid in the porous area,  $\rho_f$  is fluid density,  $\phi = V_p/V_b$  is the porosity of the fault fractured zone. The change of  $M$  before and after fluid injection can be determined by

$$\Delta M = \frac{\Delta m_f}{V_b} = \frac{\Delta V}{V_b} \rho_f \quad (4.14)$$

where  $\Delta M$  is the change in fluid mass per unit bulk volume, and  $\Delta V$  is the injected volume. Taking the total derivative of the right-hand side of equation (4.13) yields

$$\Delta M = \rho_f \Delta \phi + \phi \Delta \rho_f \quad (4.15)$$

where  $\Delta \phi$  and  $\Delta \rho_f$  are the differential forms of  $\phi$  and  $\rho_f$ . Equation (4.15) shows that the total injection volume is related to  $\Delta \phi$  and  $\Delta \rho_f$ . According to poroelasticity (Jaeger *et al.*, 2009; Zimmerman, 1986), the fluid compressibility  $C_f$  and pore volume compressibility  $C_p$  are expressed by:

$$C_f = \frac{1}{V_f} \frac{dV_f}{dP}, \quad C_p = \frac{1}{V_p} \frac{dV_p}{dP} \quad (4.16)$$

where  $dP$  is the pressure change during fluid injection. By assuming that  $V_b$  is approximately constant and substituting  $V_f = m_f/\rho_f$  and  $V_p = \phi V_b$  into equation (4.16), we obtain:

$$\begin{aligned} \Delta \rho_f &= \rho_f C_f \Delta P \\ \Delta \phi &= \phi C_p \Delta P \end{aligned} \quad (4.17)$$

Equation (4.17) relates the change in fluid density and porosity to the change in pressure. Combining equations (4.17) with equation (4.15), we arrive at:

$$\frac{\Delta V}{V_b} \rho_f = \Delta M = \rho_f \phi (C_f + C_p) \Delta P \quad (4.18)$$

This equation provides a relationship between the change in injected fluid density and the pressure change, which depends also on the fluid and rock properties represented by  $C_f$  and  $C_p$ , respectively, and the porosity  $\phi$ . Through equation (4.14) and (4.18), we obtain the total injection volume as:

$$\Delta V = V_b \phi (C_f + C_p) \Delta P \quad (4.19)$$

Equation (4.19) establishes the relationship between the change in injection volume and the pressure change during fluid injection.  $V_b = \pi abt_{frac}$  is the bulk volume of the fault fractured zone, where  $a = 40$  mm and  $b = 20$  mm are the long and short axis of the fault ellipse and  $t_{frac} = 50$   $\mu$ m is the thickness of the fault fractured zone (personal communication from F. X. Passelègue). The term  $C_f + C_p$  represents the total compressibility of the system, which is the sum of the fluid compressibility  $C_f$  and the pore volume compressibility  $C_p$ . The injected fluid has a compressibility of  $C_f = 4.6 \cdot 10^{-10}$  Pa<sup>-1</sup> (Jaeger *et al.*, 2009). Micromechanics theory (Jaeger *et al.*, 2009) suggests that pore compressibility  $C_p \approx \frac{1}{G_m} [1 - 0.25e^{-(\alpha-1)/3}]$  is dependent on the pore shape, where  $G_m$  is the material shear modulus and the aspect ratio  $\alpha$  is the proportion of the short axis to the long axis of the pore. As  $\alpha = 1$  the pore is a sphere and  $C_p = 3/(4G_m)$ . When  $\alpha \rightarrow \infty$ , the prolate spheroid is a needle-like cylinder and  $C_p = 1/(G_m)$ . Some analytical model and experimental measurements on the rock properties (Baker *et al.*, 2015; Hall, 1953; Lyons, 2009; Zhu *et al.*, 2018) show that the pore volume compressibility  $C_p$  for granite vary depending on porosity, pressure and temperature, whose value ranges from  $\sim 1 \cdot 10^{-9}$  to  $\sim 1 \cdot 10^{-11}$  Pa<sup>-1</sup> (Ojala and Grande, 2022; Walsh, 1965; Wong *et al.*, 1989). Due to the fracturing and deformation within the fault zones, the porosity is larger than the surrounding rock. Its value was tested ranging between 0.5% and 7.5% (Fredrich *et al.*, 1990; Sun and Goldberg, 1997; Zhu *et al.*, 2018).  $\Delta P$  is the average pressure change on the fault plane whose value is equal to:

$$\Delta P = \frac{1}{S} \iint [P(x, y, t) - P_0] dx dy \quad (4.20)$$

where  $S$  is the surface of the pressurized area and  $P(x, y, t) - P_0$  is obtained by the fluid diffusion equation solver at the time of fluid injection termination with respect to the fault plane. The uncertainty in the values of compressibility  $C_p$  and porosity  $\phi$  results in the uncertainty in the calculated total injection volume. The results of maximum fault slip vs. total injection volume are shown in Fig. 4.11. The maximum moment  $M_0^{max}$  is a measurement of energy released by slip on the fault (Kanamori, 1977) given by:

$$M_0^{max} = GS\xi_{max} \quad (4.21)$$

where  $G$  is shear modulus of the fault,  $S$  is the surface of rupture and  $\xi_{max}$  is the maximum fault slip. Fig. 4.12 shows the maximum aseismic moment and max magnitude vs. total injection volume. Here the max magnitude  $M_w^{max}$  is calculated by (Hanks and Kanamori, 1979; Kanamori, 1977):

$$M_w = \frac{2}{3} \log_{10}(M_0^{max}) - 6.06 \quad (4.22)$$

The figure presented in Fig. 4.11 illustrates the relationship between injection volume and fault slip behavior. The results show that the total injection volume falls within the range of  $5.95061 \cdot 10^{-13} \text{ m}^3$  to  $1.10078 \cdot 10^{-9} \text{ m}^3$ . We observe a scaling of the form  $\Delta V \sim \xi^\alpha$  with  $\alpha \approx 0.44$  ( $\alpha \approx 0.5$ ).

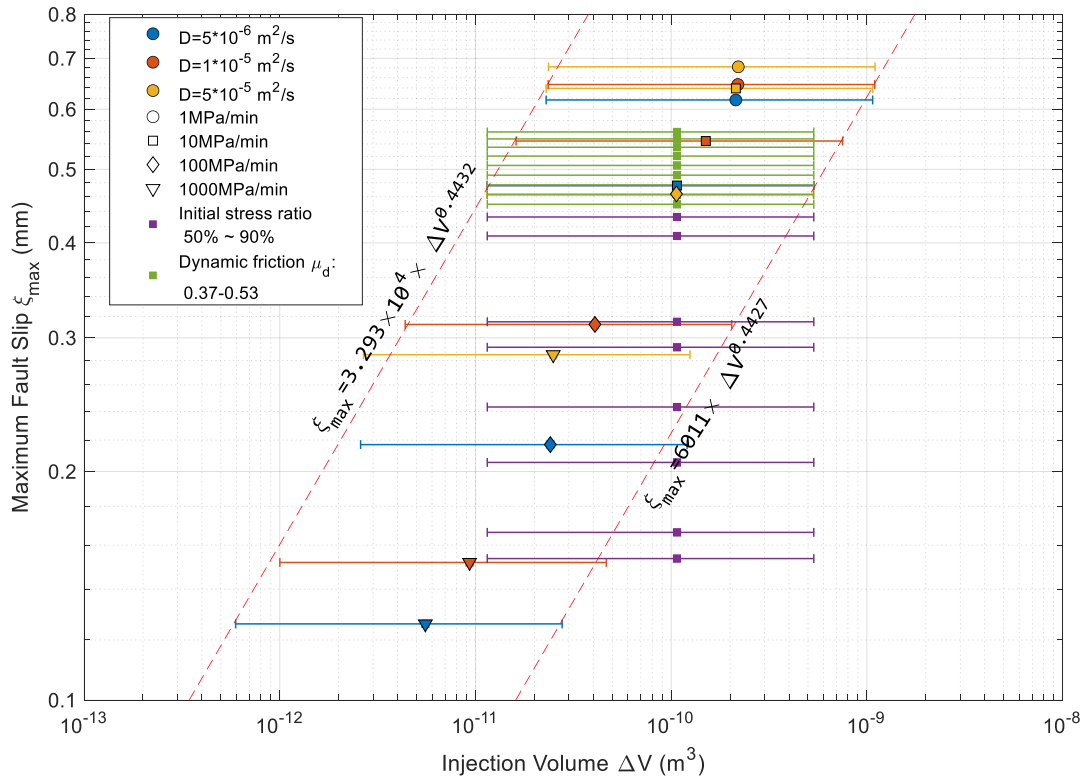


Figure 4.11: Maximum fault slip  $\xi_{max}$  with respect of total injection volume  $\Delta V$ . The fluid compressibility  $C_f = 4.6 \cdot 10^{-10} \text{ Pa}^{-1}$ , pore volume compressibility ranges between  $\sim 1 \cdot 10^{-9} \text{ Pa}^{-1}$  and  $\sim 1 \cdot 10^{-11} \text{ Pa}^{-1}$ , porosity  $\phi$  is within 0.5% and 7.5%. The injection rate was from 1 to 1000 MPa/min. Hydraulic diffusivity  $D = 5 \cdot 10^{-6} \text{ m}^2/\text{s}$  (blue marker),  $1 \cdot 10^{-5} \text{ m}^2/\text{s}$  (red marker) and  $5 \cdot 10^{-5} \text{ m}^2/\text{s}$  (yellow marker). The dynamic friction coefficient  $\mu_d = 0.5$  and the critical slip distance  $d_c = 0.3 \text{ mm}$ . Purple marker: initial stress ratio from 0.5 to 0.9 (injection rate 10 MPa/min,  $D = 5 \cdot 10^{-6} \text{ m}^2/\text{s}$ ). Green marker: dynamic friction coefficient from 0.37 to 0.53 (injection rate 10 MPa/min,  $D = 5 \cdot 10^{-6} \text{ m}^2/\text{s}$ ).

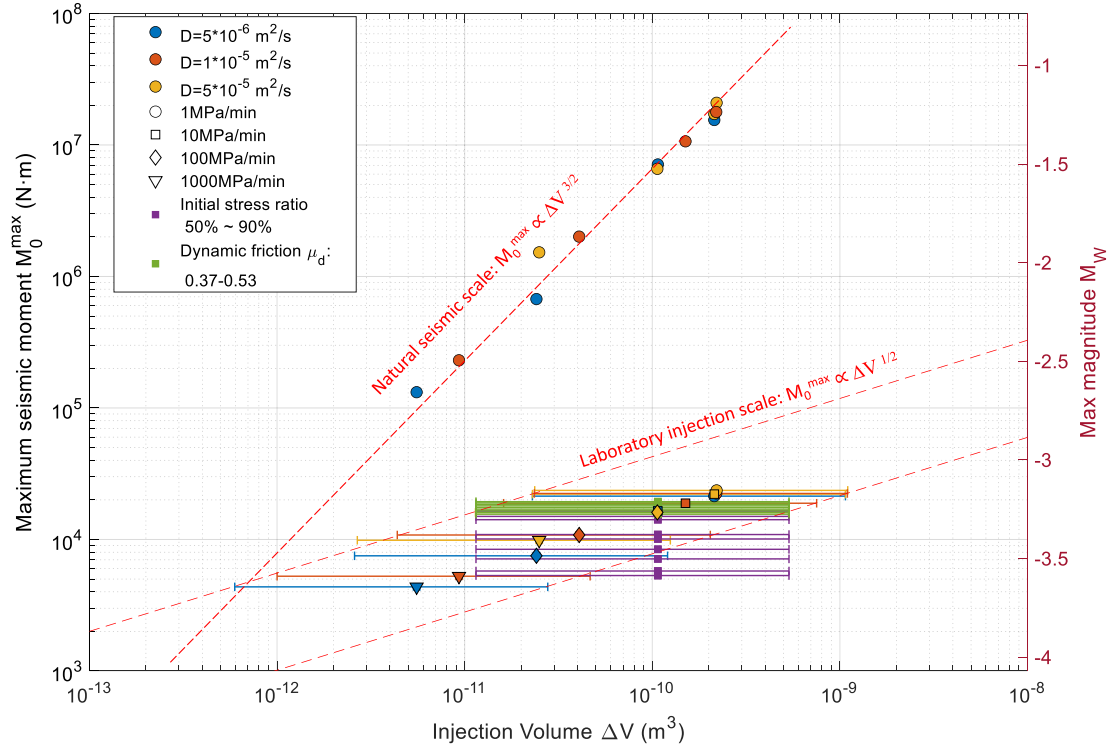


Figure 4.12: Maximum moment  $M_0^{max}$  and max magnitude  $M_w$  with respect of total injection volume  $\Delta V$  in both natural and laboratory scale. The rupture area in the laboratory scale is the elliptical area of the fault at the laboratory model scale. For the natural scale, the moment is calculated assuming constant stress drop  $\Delta\tau$ . The fluid compressibility  $C_f = 4.6 \cdot 10^{-10} \text{ Pa}^{-1}$ , pore volume compressibility ranges between  $\sim 1 \cdot 10^{-9} \text{ Pa}^{-1}$  and  $\sim 1 \cdot 10^{-11} \text{ Pa}^{-1}$ , porosity  $\phi$  is within 0.5% and 7.5%. The injection rate was from 1 to 1000 MPa/min. Hydraulic diffusivity  $D = 5 \cdot 10^{-6} \text{ m}^2/\text{s}$  (blue marker),  $1 \cdot 10^{-5} \text{ m}^2/\text{s}$  (red marker) and  $5 \cdot 10^{-5} \text{ m}^2/\text{s}$  (yellow marker). The dynamic friction coefficient  $\mu_d = 0.5$  and the critical slip distance  $d_c = 0.3 \text{ mm}$ . Purple marker: initial stress ratio from 0.5 to 0.9 (injection rate 10 MPa/min,  $D = 5 \cdot 10^{-6} \text{ m}^2/\text{s}$ ). Green marker: dynamic friction coefficient from 0.37 to 0.53 (injection rate 10 MPa/min,  $D = 5 \cdot 10^{-6} \text{ m}^2/\text{s}$ ).

In Fig. 4.12, the relationship of maximum aseismic moment  $M_0^{max}$  and max magnitude  $M_w$  is illustrated. Note that the rupture surface considered for the laboratory scale is based on the elliptical area of the fault at the laboratory model

scale. Natural faults exhibit slip that is not limited by the size of the fault sample, which means that the rupture surface  $S$  in equation (4.21) does not necessarily represent the size of the experimental fault,  $L$ . Instead, we can estimate another length scale,  $L_0$ , assuming a constant stress drop  $\Delta\tau = 40$  MPa (see Fig. 4.5a and b). We have

$$\Delta\tau = G \frac{\xi_{max}}{L_0} \implies L = G \frac{\xi_{max}}{\Delta\tau} \quad S = L_0^2 = \frac{G^2 \xi_{max}^2}{\Delta\tau^2} \implies M_0^{max} = \frac{G^3 \xi_{max}^3}{\Delta\tau^2} \quad (4.23)$$

We present the second (natural) estimate of the maximum aseismic moment,  $M_0^{max}$  in Fig. 4.12, as a function of the injected volume,  $\Delta V$ . Rescaling that  $\xi_{max} \sim \Delta V^{1/2}$ , we can establish from equation (4.24) that the maximum aseismic moment at the natural scale of aseismic slip is proportional to the injection volume raised to the power of 3/2:

$$M_0^{max} \propto \Delta V^{3/2} \quad (4.24)$$

Another theoretical model based on dynamic rupture mechanics developed by (Galis *et al.*, 2017) showed the same scaling relation between the largest magnitude and injected volume as in equation (4.24). However, this model was specifically designed to explain dynamically triggered slips during earthquakes. Our numerical findings on the aseismic slip are in agreement with this scaling (Fig. 4.12).

In Fig. 4.13, we compare our numerical results of the maximum aseismic moment and max magnitude as a function of total injection volume in both laboratory and natural scales along with other estimates from the laboratory (Goodfellow *et al.*, 2015), the field (Atkinson *et al.*, 2016; De Barros *et al.*, 2016; Duboeuf *et al.*, 2017; Maxwell, 2013; McGarr, 2014) and numerical models (Buijze *et al.*, 2015) (data provided by Galis *et al.*, 2017). Due to the estimation of fluid volume limited in the fault crack zone (Ji *et al.*, 2022), the range of fluid volume in our model is about  $10^5$  times lower than experimental observations. Additionally, the finite element model accounts for stress transfer on the contact surface, resulting in only a small degree of penetration on the surface. Therefore, no excess fluid is injected as a result of the fracture opening. We consider modifying our results with the fluid volume stored in the injection tube and borehole which is about  $6.17 \cdot 10^{-6} \text{ m}^3$ . With the modified injection volume, our simulation results align with other experimental observations better. From Fig. 4.13 we also observed that  $M_0^{max}$  is also sensitive to the initial stress, which is also found in theoretical models based on rupture mechanics (Galis *et al.*, 2017; Garagash and Germanovich, 2012). Furthermore, we find that the seismic energy released is also dependent on the frictional parameters.

As the residual friction (dynamic friction coefficient  $\mu_d$ ) and critical slip distance  $d_c$  increase, the maximum aseismic moment will decrease. The findings provide an insight into the relationship between seismic energy released with hydraulic, mechanical and frictional parameters, which have implications for understanding and predicting the induced seismicity.

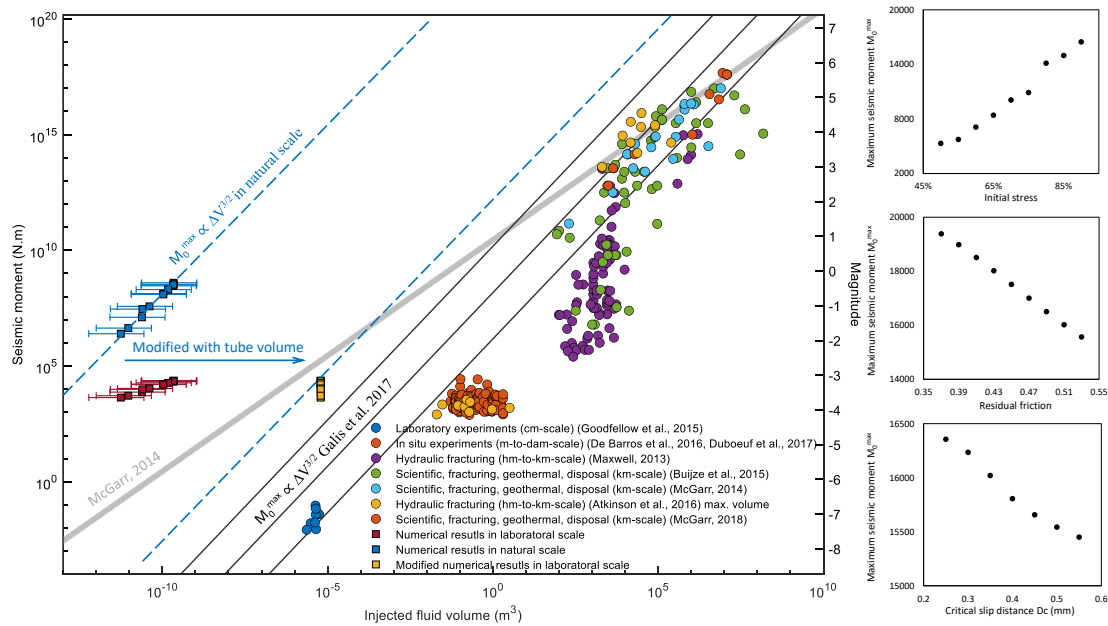


Figure 4.13: Left: Comparison of our numerical simulation results of the maximum aseismic moment and max magnitude vs. injection volume with other injection-induced seismicities. The numerical results are presented both in the laboratory and in natural scales, with modified injection volume in the experiment (yellow square sequences) (From Galis *et al.*, 2017). Right: Relationship between maximum aseismic moment with initial stress, dynamic friction coefficient and critical slip distance.

## 4.7 Conclusion

We conducted numerical simulations of an injection experiment performed in a saw-cut rack sample, loaded in a triaxial set-up. A three-dimensional finite element model that considers the interplay of hydro-mechanical and frictional processes was developed and accurately reproduced the laboratory results.

Considering typical parameter ranges, stress and injection rate have a dominant effect on slip propagation, while frictional properties and fault's hydraulic diffusivity play a secondary role. Initial stress close to failure and high injection rates both increase slip front speed and reduce the reactivation time of aseismic slip events.

We also discussed the rupture propagation reactivated by fluid injection. The migration of shear stress along the fault ellipse was used to estimate the rupture propagation speed, which was found to mainly depend on injection rate and initial stress state while secondarily influenced by hydraulic diffusivity and frictional properties. We explain this observation using an equation based on the Linear Elastic Fracture Mechanics Theory (LEFM) and the critical fracture energy required to propagate the crack tip.

Finally, in our simulations, we investigated the relationship between the maximum slip and aseismic moment with injection volume. The relationship between the change in injection volume and the pressure change during fluid injection was established to obtain fluid injection volume from the coupled finite element model. We observed a linear relationship between maximum aseismic slip and injected volume, resulting in an aseismic moment scaling as the injected volume to the power  $3/2$ , in agreement with recent mechanical and theoretical studies on the aseismic slip.

# Chapter 5

## Conclusions and perspectives

Résumé . . . . .	120
Summary . . . . .	120
5.1 General conclusions . . . . .	120
5.2 Perspectives . . . . .	123
5.2.1 Impact of evolving hydraulic diffusivity . . . . .	123
5.2.2 Advancing Understanding of Induced Seismicity . . . . .	123

## Résumé

Ce chapitre résume que les projets industriels d'injection de fluides induisent la sismicité, avec une magnitude sismique étroitement liée au volume de fluide injecté. La poro-élasticité et le glissement a-sismique jouent des rôles cruciaux, nécessitant des recherches supplémentaires pour une meilleure compréhension et des meilleures pratiques. Le chapitre 2 décrit la configuration expérimentale et le modèle numérique pour simuler la réactivation des failles. Le chapitre 3 utilise des modèles calibrés de méthode des éléments finis pour étudier la réactivation des failles, en mettant l'accent sur les propriétés des matériaux, l'hydraulique, le stress et le frottement. Le chapitre 4 étudie l'impact des paramètres d'injection sur le glissement a-sismique, mettant en évidence l'influence dominante du stress et du débit d'injection. Les perspectives suggèrent d'étudier l'évolution de la diffusivité et d'avancer dans la compréhension de la sismicité induite pour améliorer les pratiques industrielles.

## Summary

This chapter summarizes that industrial fluid injection projects induce seismicity, with earthquake magnitude closely related to injected fluid volume. Poro-elasticity and aseismic slip play crucial roles, necessitating further research for better understanding and best practices. Chapter 2 describes the experimental setup and numerical model for simulating fault reactivation. Chapter 3 utilizes calibrated finite element method models to study fault reactivation, emphasizing material properties, hydraulics, stress, and friction. Chapter 4 investigates the impact of injection parameters on aseismic slip, highlighting the dominant influence of stress and injection rate. Perspectives suggest studying evolving hydraulic diffusivity and advancing understanding of induced seismicity for improved industry practices.

### 5.1 General conclusions

Industrial fluid injection projects have been shown to induce seismicity (Ellsworth, 2013), with the magnitude of induced earthquakes being closely related to the total volume of injected fluid (Galis *et al.*, 2017; McGarr, 2014). However, the exact relationship between these two factors is not yet fully understood. Poro-elasticity, fluid change and aseismic slip, which involves the coupling between fluid pressure, rock deformation and the frictional relationship of the fault interface, also play a

crucial role in fluid-induced fault slip. As such, further research is needed to fully comprehend the mechanisms behind induced seismicity and develop best practices for such projects. This Ph.D. thesis addresses the importance of studying induced seismicity in relation to industrial fluid injection projects by presenting a numerical modeling study of fluid-induced fault slip reactivation.

In this thesis, Chapter 2 provides a detailed description of the experimental setup and numerical model used to simulate injection-induced fault reactivation under increasing fluid pressure. The hydro-mechanical coupling between elasticity, friction mechanics of rock, and fluid diffusion is discussed in detail, along with the governing equations for stress, strain, pore pressure, and fault slip. The model configuration including geometry, element mesh, material properties, loading progress, boundary conditions and contact type are also described. This information provides a solid foundation for understanding the subsequent results and analysis presented in later chapters.

In Chapter 3, we presented a comprehensive approach to investigating the behavior of pre-existing fault reactivation induced by fluid injection. We configured 2D and 3D finite element method (FEM) numerical models and calibrated them using laboratory experiments. By coupling the models with a solver of fluid diffusivity and slip-weakening friction criterion, we were able to reproduce experimental results and investigate how hydraulic, stress state, and frictional parameters affect the mechanical response of fault slip induced by fluid injection. Our study provides valuable insights into the factors that control fault stability and the potential for induced seismicity in subsurface engineering activities. The results highlight the importance of considering material properties, hydraulic parameters, stress state, and frictional parameters in risk assessment and management of induced seismicity. Overall, our approach can be used to improve the accuracy of numerical models and provide guidance for safe and sustainable subsurface operations.

Chapter 4 presented the simulation and results of the impact of injection rate, hydraulic diffusivity, stress state and frictional properties on the propagation speed and the maximum magnitude of aseismic slip events generated in our model. Considering typical parameter ranges, stress and injection rate have a dominant effect on slip propagation, while frictional properties and fault's hydraulic diffusivity play a secondary role. Initial stress close to failure and high injection rates both increase slip front speed and reduce the reactivation time of aseismic slip events.

We also discussed the rupture propagation reactivated by fluid injection. The migration of shear stress along the fault ellipse was used to estimate the rupture propagation speed, which was found to mainly depend on injection rate and initial stress state while secondarily influenced by hydraulic diffusivity and frictional properties. We explain this observation using an equation based on the Linear Elastic Fracture Mechanics Theory (LEFM) and the critical fracture energy required to propagate the crack tip.

Finally, in our simulations, we investigated the relationship between the maximum slip and aseismic moment with injection volume. The relationship between the change in injection volume and the pressure change during fluid injection was established to obtain fluid injection volume from the coupled finite element model. We observed a linear relationship between maximum aseismic slip and injected volume, resulting in an aseismic moment scaling as the injected volume to the power  $3/2$ , in agreement with recent mechanical and theoretical studies on the aseismic slip.

Overall, our study provides insights into the complex behavior of pre-existing fault reactivation induced by fluid injection and quantifies the importance of hydro-mechanical properties and injection scenarios on the dynamics of aseismic slip, suspected to trigger induced earthquakes. The findings of this study can thus inform on the development of strategies to mitigate the risk of induced earthquakes in geothermal energy production and fluid injection practices.

## 5.2 Perspectives

### 5.2.1 Impact of evolving hydraulic diffusivity

One possible angle to explore in the study of fault slip reactivation induced by fluids is the impact of evolving hydraulic diffusivity. While our research has already considered various values of hydraulic diffusivity within the range of approximately  $1 \cdot 10^{-6} \text{ m}^2/\text{s}$  to  $1 \cdot 10^{-5} \text{ m}^2/\text{s}$ , it is important to acknowledge that in real-world settings, hydraulic diffusivity may not remain constant over time and space due to a variety of factors such as temperature, stress changes, slip and related damage accumulation. Thus, it is crucial to investigate how changes in hydraulic diffusivity could affect the likelihood and magnitude of fault slip reactivation.

Expanding on this idea, a potential avenue for future research could be to develop new numerical models that incorporate evolving hydraulic diffusivity into the calculations. This would allow for more accurate predictions of the behavior of fault systems under varying conditions of fluid injection or extraction. Such models could incorporate known relationships between hydraulic diffusivity, stress and slip and could be used to simulate the effects of different fluid injection scenarios on fault systems.

New injection experiments have recently been conducted, to better constrain what controls the evolution of hydraulic diffusivity with aseismic slip. These experiments are done both at the laboratory scale (Almakari *et al.*, 2020) and at the decametric scale (Cappa *et al.*, 2018; Cappa *et al.*, 2022a,b).

The insights gained from this research could have important implications for the management of fluid injection and extraction in geothermal energy systems and other applications where fault slip reactivation is a concern. By better understanding the role of evolving hydraulic diffusivity in fault behavior, engineers and operators could develop more effective strategies for managing fluid injection and extraction, and ultimately reduce the risk of induced seismicity.

### 5.2.2 Advancing Understanding of Induced Seismicity

Understanding the physical and mechanical behavior behind induced earthquakes is critical to mitigating their impact and preventing them from happening in the future. Our numerical model has the potential to make significant contributions in

this field by providing a more comprehensive view of the underlying mechanisms involved.

One of the strengths of our model is its ability to simulate a wide range of laboratory experiments beyond what Almakari *et al.* (2020)'s research covered. For example, we can use our model to explore the stress and strain evolution, induced seismic slip, crack propagation and other variables on the occurrence of induced earthquakes. This information can be used to inform best practices and policies for industries such as geothermal energy, hydraulic fracturing, and wastewater injection.

Moreover, our model can also help us to better understand the evolution of induced seismicity over time. By simulating the behavior of faults and fractures under different conditions, we can observe how they change and evolve over time, and how these changes can impact the occurrence of induced earthquakes. This knowledge can then be used to develop more accurate and effective early warning systems and risk management strategies.

Overall, our numerical model offers exciting possibilities for advancing our understanding of induced seismicity and its underlying mechanisms. As we continue to refine and improve the model, we hope to contribute to a safer and more sustainable future for all.

# Bibliography

- Abaqus, F. *et al.* (2019), Dassault systemes simulia corporation, in *Providence, Rhode Island, USA*.
- Aki, K. *et al.* (1982), Interpretation of seismic data from hydraulic fracturing experiments at the Fenton Hill, New Mexico, hot dry rock geothermal site, in *Journal of Geophysical Research: Solid Earth* **87**.B2, 936–944.
- Almakari, M *et al.* (2020), Fault’s hydraulic diffusivity enhancement during injection induced fault reactivation: application of pore pressure diffusion inversions to laboratory injection experiments, in *Geophysical Journal International* **223**.3, 2117–2132.
- Almakari, M. (2019a), Réactivation Hydro-Mécanique d’une Faille Rate & State Glissement, Sismicité et Évolution de Perméabilité, PhD thesis, Paris Sciences et Lettres (ComUE).
- (2019b), Réactivation Hydro-Mécanique d’une Faille Rate & State Glissement, Sismicité et Évolution de Perméabilité, Thèse de doctorat dirigée par Chauris, Hervé et Dublanchet, Pierre Géosciences et géoingénierie Paris Sciences et Lettres (ComUE) 2019, PhD thesis.
- Almakari, M. *et al.* (2019), Effect of the injection scenario on the rate and magnitude content of injection-induced seismicity: Case of a heterogeneous fault, in *Journal of Geophysical Research: Solid Earth* **124**.8, 8426–8448.
- Aminu, M. D. *et al.* (2017), A review of developments in carbon dioxide storage, in *Applied Energy* **208**, 1389–1419.
- Atkinson, G. M. *et al.* (2016), Hydraulic fracturing and seismicity in the Western Canada Sedimentary Basin, in *Seismological research letters* **87**.3, 631–647.

- Baghbanan, A. and L. Jing (2008), Stress effects on permeability in a fractured rock mass with correlated fracture length and aperture, in *International journal of rock mechanics and mining sciences* **45.8**, 1320–1334.
- Baig, A. and T. Urbancic (2010), Microseismic moment tensors: A path to understanding frac growth, in *The Leading Edge* **29.3**, 320–324.
- Baker, R. O. *et al.* (2015), *Practical reservoir engineering and characterization*, Gulf Professional Publishing.
- Bao, X. and D. W. Eaton (2016), Fault activation by hydraulic fracturing in western Canada, in *Science* **354.6318**, 1406–1409.
- Barati, R. and J.-T. Liang (2014), A review of fracturing fluid systems used for hydraulic fracturing of oil and gas wells, in *Journal of Applied Polymer Science* **131.16**.
- Barton, C. A. *et al.* (1995), Fluid flow along potentially active faults in crystalline rock, in *Geology* **23.8**, 683–686.
- Barton, N. (1976), The shear strength of rock and rock joints, in *International Journal of rock mechanics and mining sciences & Geomechanics abstracts*, vol. 13, 9, Elsevier, 255–279.
- Bauer, R. A. *et al.* (2016), Overview of microseismic response to CO<sub>2</sub> injection into the Mt. Simon saline reservoir at the Illinois Basin-Decatur Project, in *International Journal of Greenhouse Gas Control* **54**, 378–388.
- Benioff, H. (1964), Earthquake Source Mechanisms: Although progress has been made in the understanding of earthquakes, many problems remain., in *Science* **143.3613**, 1399–1406.
- Bernabe, Y (1986), The effective pressure law for permeability in Chelmsford granite and Barre granite, in *International Journal of Rock Mechanics and Mining Sciences & Geomechanics Abstracts*, vol. 23, 3, Elsevier, 267–275.
- Bhattacharya, P. and R. C. Viesca (2019), Fluid-induced aseismic fault slip outpaces pore-fluid migration, in *Science* **364.6439**, 464–468.
- Blöcher, G. *et al.* (2018), Evaluating micro-seismic events triggered by reservoir operations at the geothermal site of Groß Schönebeck (Germany), in *Rock Mechanics and Rock Engineering* **51.10**, 3265–3279.
- Bormann, P. (2002), *New manual of seismological observatory practice*, in.

- Bourouis, S. and P. Bernard (2007), Evidence for coupled seismic and aseismic fault slip during water injection in the geothermal site of Soultz (France), and implications for seismogenic transients, in *Geophysical Journal International* **169.2**, 723–732.
- Brace, W. and J. Byerlee (1966), Stick-slip as a mechanism for earthquakes, in *science* **153.3739**, 990–992.
- Brace, W. *et al.* (1968), Permeability of granite under high pressure, in *Journal of Geophysical research* **73.6**, 2225–2236.
- Brinckerhoff, P. *et al.* (2011), Accelerating the uptake of CCS: industrial use of captured carbon dioxide, in *Global CCS Institute* **260**.
- Brune, J. N. and C. R. Allen (1967), A low-stress-drop, low-magnitude earthquake with surface faulting: The Imperial, California, earthquake of March 4, 1966, in *Bulletin of the Seismological Society of America* **57.3**, 501–514.
- Buijze, L *et al.* (2015), Moment partitioning for injection-induced seismicity: Case studies & insights from numerical modeling, in *Moment* **19**, 25.
- Byerlee, J. D. (1968), Brittle-ductile transition in rocks, in *Journal of Geophysical Research* **73.14**, 4741–4750.
- Byerlee, J. (1978), Friction of rocks, in *Rock friction and earthquake prediction*, Springer, 615–626.
- Calò, M *et al.* (2011), Large-scale aseismic motion identified through 4-DP-wave tomography, in *Geophysical Journal International* **186.3**, 1295–1314.
- Cappa, F *et al.* (2006), Hydromechanical modelling of pulse tests that measure fluid pressure and fracture normal displacement at the Coaraze Laboratory site, France, in *International Journal of Rock Mechanics and Mining Sciences* **43.7**, 1062–1082.
- Cappa, F *et al.* (2018), On the relationship between fault permeability increases, induced stress perturbation, and the growth of aseismic slip during fluid injection, in *Geophysical Research Letters* **45.20**, 11–012.
- Cappa, F *et al.* (2019), Stabilization of fault slip by fluid injection in the laboratory and in situ, in *Science advances* **5.3**, eaau4065.
- Cappa, F. *et al.* (2022a), Fluid migration in low-permeability faults driven by decoupling of fault slip and opening, in *Nature Geoscience* **15.9**, 747–751.

- Cappa, F. *et al.* (2022b), Transient evolution of permeability and friction in a slowly slipping fault activated by fluid pressurization, in *Nature communications* **13.1**, 3039.
- Chen, X *et al.* (2012), Spatial migration of earthquakes within seismic clusters in Southern California: Evidence for fluid diffusion, in *Journal of Geophysical Research: Solid Earth* **117**.B4.
- Chen, Z *et al.* (2000), An experimental investigation of hydraulic behaviour of fractures and joints in granitic rock, in *International Journal of Rock Mechanics and Mining Sciences* **37.7**, 1061–1071.
- Childs, P. R. (2010), *Rotating flow*, Elsevier.
- Clarke, H. *et al.* (2014), Felt seismicity associated with shale gas hydraulic fracturing: The first documented example in Europe, in *Geophysical Research Letters* **41.23**, 8308–8314.
- Clough, R. W. (1990), Original formulation of the finite element method, in *Finite elements in analysis and design* **7.2**, 89–101.
- Collettini, C. *et al.* (2014), A novel and versatile apparatus for brittle rock deformation, in *International journal of rock mechanics and mining sciences* **66**, 114–123.
- Constantin, P. and C. Foias (2020), *Navier-stokes equations*, University of Chicago Press.
- Cornet, F. *et al.* (1997), Seismic and aseismic slips induced by large-scale fluid injections, in *Seismicity associated with mines, reservoirs and fluid injections*, Springer, 563–583.
- Cornet, F. H. (2016), Seismic and aseismic motions generated by fluid injections, in *Geomechanics for Energy and the Environment* **5**, 42–54.
- Coulomb, C. A. (1773), *Application of the rules of maxima and minima to some problems of statics related to architecture*, Paris : De l'Imprimerie Royale.
- DECC, C. (2012), Roadmap: Supporting deployment of carbon capture and storage in the UK, in *UK Department of Energy and Climate Change*.
- Danré, P. *et al.* (2022), Prevalence of aseismic slip linking fluid injection to natural and anthropogenic seismic swarms, in *Journal of Geophysical Research: Solid Earth*, e2022JB025571.

- De Barros, L. *et al.* (2016), Fault structure, stress, or pressure control of the seismicity in shale? Insights from a controlled experiment of fluid-induced fault reactivation, in *Journal of Geophysical Research: Solid Earth* **121.6**, 4506–4522.
- De Barros, L. *et al.* (2018), Seismicity and fault aseismic deformation caused by fluid injection in decametric in-situ experiments, in *Comptes Rendus Geoscience* **350.8**, 464–475.
- De Barros, L. *et al.* (2020), Imbricated aseismic slip and fluid diffusion drive a seismic swarm in the Corinth Gulf, Greece, in *Geophysical Research Letters* **47.9**, e2020GL087142.
- Deichmann, N. and D. Giardini (2009), Earthquakes Induced by the Stimulation of an Enhanced Geothermal System below Basel (Switzerland), in *Seismological Research Letters* **80.5**, 784–798.
- Deichmann, N. *et al.* (2014), Identification of faults activated during the stimulation of the Basel geothermal project from cluster analysis and focal mechanisms of the larger magnitude events, in *Geothermics* **52**, 84–97.
- Derode, B. *et al.* (2013), Coupled seismo-hydromechanical monitoring of inelastic effects on injection-induced fracture permeability, in *International Journal of Rock Mechanics and Mining Sciences* **61**, 266–274.
- Diehl, T. *et al.* (2017), The induced earthquake sequence related to the St. Gallen deep geothermal project (Switzerland): Fault reactivation and fluid interactions imaged by microseismicity, in *Journal of Geophysical Research: Solid Earth* **122.9**, 7272–7290.
- Dieterich, J. H. (1979), Modeling of rock friction: 1. Experimental results and constitutive equations, in *Journal of Geophysical Research: Solid Earth* **84.B5**, 2161–2168.
- Doan, M.-L. *et al.* (2006), In situ measurement of the hydraulic diffusivity of the active Chelungpu Fault, Taiwan, in *Geophysical Research Letters* **33.16**.
- Dorbath, L. *et al.* (2009), Seismic response of the fractured and faulted granite of Soultz-sous-Forêts (France) to 5 km deep massive water injections, in *Geophysical Journal International* **177.2**, 653–675.
- Dowson, D. (1978), *History of tribology*, Addison-Wesley Longman Limited.

- Dublanchet, P. (2019), Fluid driven shear cracks on a strengthening rate-and-state frictional fault, in *Journal of the Mechanics and Physics of Solids* **132**, 103672.
- Dublanchet, P. and L. De Barros (2021), Dual seismic migration velocities in seismic swarms, in *Geophysical Research Letters* **48.1**, e2020GL090025.
- Duboeuf, L. *et al.* (2017), Aseismic motions drive a sparse seismicity during fluid injections into a fractured zone in a carbonate reservoir, in *Journal of Geophysical Research: Solid Earth* **122.10**, 8285–8304.
- Eaton, D. W. (2018), *Passive seismic monitoring of induced seismicity: Fundamental principles and application to energy technologies*, Cambridge University Press.
- Eaton, D. W. *et al.* (2014), Scaling relations and spectral characteristics of tensile microseisms: Evidence for opening/closing cracks during hydraulic fracturing, in *Geophysical Journal International* **196.3**, 1844–1857.
- Eccles, D *et al.* (2005), Laboratory studies of electrical potential during rock failure, in *International Journal of Rock Mechanics and Mining Sciences* **42.7-8**, 933–949.
- Eisner, L. *et al.* (2010), Beyond the dots in the box: Microseismicity-constrained fracture models for reservoir simulation, in *The Leading Edge* **29.3**, 326–333.
- Ellsworth, W. L. (2013), Injection-induced earthquakes, in *science* **341.6142**, 1225942.
- Elst, N. J. Van der *et al.* (2013), Enhanced remote earthquake triggering at fluid-injection sites in the midwestern United States, in *Science* **341.6142**, 164–167.
- Estrada, J. M. and R. Bhamidimarri (2016), A review of the issues and treatment options for wastewater from shale gas extraction by hydraulic fracturing, in *Fuel* **182**, 292–303.
- Eyre, T. S. *et al.* (2019), The role of aseismic slip in hydraulic fracturing–induced seismicity, in *Science advances* **5.8**, eaav7172.
- Fälth, B. *et al.* (2015), Simulating earthquake rupture and off-fault fracture response: Application to the safety assessment of the Swedish nuclear waste repository, in *Bulletin of the Seismological Society of America* **105.1**, 134–151.
- Fick, A. (1855), Ueber diffusion, in *Annalen der Physik* **170.1**, 59–86.
- Frederikse, T. *et al.* (2020), The causes of sea-level rise since 1900, in *Nature* **584.7821**, 393–397.

- Fredrich, J. T. *et al.* (1990), Effect of grain size on brittle and semibrittle strength: Implications for micromechanical modelling of failure in compression, in *Journal of Geophysical Research: Solid Earth* **95**.B7, 10907–10920.
- Freund, L. B. (1998), *Dynamic fracture mechanics*, Cambridge university press.
- Galis, M. *et al.* (2017), Induced seismicity provides insight into why earthquake ruptures stop, in *Science advances* **3**.12, eaap7528.
- Garagash, D. I. and L. N. Germanovich (2012), Nucleation and arrest of dynamic slip on a pressurized fault, in *Journal of Geophysical Research: Solid Earth* **117**.B10.
- Genter, A. *et al.* (2010), Contribution of the exploration of deep crystalline fractured reservoir of Soultz to the knowledge of enhanced geothermal systems (EGS), in *Comptes Rendus Geoscience* **342**.7-8, 502–516.
- Ghabezloo, S. *et al.* (2009), Effective stress law for the permeability of a limestone, in *International Journal of Rock Mechanics and Mining Sciences* **46**.2, 297–306.
- Gibowicz, S. J. (2009), Seismicity induced by mining: Recent research, in *Advances in geophysics* **51**, 1–53.
- Gischig, V. S. (2015), Rupture propagation behavior and the largest possible earthquake induced by fluid injection into deep reservoirs, in *Geophysical Research Letters* **42**.18, 7420–7428.
- Goertz-Allmann, B. *et al.* (2017), Characterization of induced seismicity patterns derived from internal structure in event clusters, in *Journal of Geophysical Research: Solid Earth* **122**.5, 3875–3894.
- GoertzAllmann, B. P. *et al.* (2011), Stress drop variations of induced earthquakes at the Basel geothermal site, in *Geophysical Research Letters* **38**.9.
- Goodfellow, S. *et al.* (2015), Hydraulic fracture energy budget: Insights from the laboratory, in *Geophysical Research Letters* **42**.9, 3179–3187.
- Grandin, R. *et al.* (2017), Rupture process of the M W 5.8 Pawnee, Oklahoma, earthquake from Sentinel-1 InSAR and seismological data, in *Seismological Research Letters* **88**.4, 994–1004.
- Grigoli, F. *et al.* (2017), Current challenges in monitoring, discrimination, and management of induced seismicity related to underground industrial activities: A European perspective, in *Reviews of Geophysics* **55**.2, 310–340.

- Grigoli, F. *et al.* (2018), The November 2017 Mw 5.5 Pohang earthquake: A possible case of induced seismicity in South Korea, in *Science* **360**.6392, 1003–1006.
- Group, I. C. (2016), 3DEC, 3-Dimensional Distinct Element Code., in *Itasca Consulting Group*.
- Guglielmi, Y. *et al.* (2008), High-definition analysis of fluid-induced seismicity related to the mesoscale hydromechanical properties of a fault zone, in *Geophysical Research Letters* **35**.6.
- Guglielmi, Y. *et al.* (2015a), In situ observations on the coupling between hydraulic diffusivity and displacements during fault reactivation in shales, in *Journal of Geophysical Research: Solid Earth* **120**.11, 7729–7748.
- Guglielmi, Y. *et al.* (2015b), Seismicity triggered by fluid injection–induced aseismic slip, in *Science* **348**.6240, 1224–1226.
- Gutierrez, M *et al.* (2000), Stress-dependent permeability of a de-mineralised fracture in shale, in *Marine and Petroleum Geology* **17**.8, 895–907.
- Hall, H. N. (1953), Compressibility of reservoir rocks, in *Journal of Petroleum Technology* **5**.01, 17–19.
- Hanks, T. C. and H. Kanamori (1979), A moment magnitude scale, in *Journal of Geophysical Research: Solid Earth* **84**.B5, 2348–2350.
- Häring, M. O. *et al.* (2008), Characterisation of the Basel 1 enhanced geothermal system, in *Geothermics* **37**.5, 469–495.
- Hill, D. *et al.* (1990), The 1989 earthquake swarm beneath Mammoth Mountain, California: An initial look at the 4 May through 30 September activity, in *Bulletin of the Seismological Society of America* **80**.2, 325–339.
- Hooke Robert, -. *et al.* (2004), *Lectures de potentia restitutiva, or, Of spring explaining the power of springing bodies : to which are added some collections viz. a description of Dr. Pappins wind-fountain and force-pump, Mr. Young's observation concerning natural fountains, some other considerations concerning that subject, Captain Sturmy's remarks of a subterraneous cave and cistern, Mr. G.T. observations made on the Pike of Teneriff, 1674, some reflections and conjectures occasioned thereupon, a relation of a late eruption in the Isle of Palma / by Robert Hooke ...* Oxford Text Archive.
- Hooke, R. (1678), *Lectures de Potentia Restitutiva, Or of Spring Explaining the Power of Springing Bodies*, [Cutlerian lecture, John Martyn.

- Horton, S. (2012), Disposal of hydrofracking waste fluid by injection into subsurface aquifers triggers earthquake swarm in central Arkansas with potential for damaging earthquake, in *Seismological Research Letters* **83.2**, 250–260.
- Hough, S. *et al.* (2000), The 1998 earthquake sequence south of Long Valley Caldera, California: hints of magmatic involvement, in *Bulletin of the Seismological Society of America* **90.3**, 752–763.
- Ida, Y. (1972), Cohesive force across the tip of a longitudinal-shear crack and Griffith's specific surface energy, in *Journal of Geophysical Research* **77.20**, 3796–3805.
- Jaeger, J. C. *et al.* (2009), *Fundamentals of rock mechanics*, John Wiley & Sons.
- Ji, Y. *et al.* (2022), Effects of external temperature and dead volume on laboratory measurements of pore pressure and injected volume in a rock fracture, in *Journal of Rock Mechanics and Geotechnical Engineering* **14.5**, 1461–1469.
- Johnson, C. E. and D. M. Hadley (1976), Tectonic implications of the Brawley earthquake swarm, Imperial valley, California, January 1975, in *Bulletin of the Seismological Society of America* **66.4**, 1133–1144.
- Jones, F. O. and W. Owens (1980), A laboratory study of low-permeability gas sands, in *Journal of petroleum Technology* **32.09**, 1631–1640.
- Kagel, A. *et al.* (2005), A guide to geothermal energy and the environment, in.
- Kanamori, H. (1977), The energy release in great earthquakes, in *Journal of geophysical research* **82.20**, 2981–2987.
- Kao, H *et al.* (2016), Technical meeting on the traffic light protocols (TLP) for induced seismicity: Summary and recommendations, in *Geological Survey of Canada, Open File* **8075.20**, 15.
- Kao, H. *et al.* (2018), Performance assessment of the induced seismicity traffic light protocol for northeastern British Columbia and western Alberta, in *The Leading Edge* **37.2**, 117–126.
- Kato, A. and K. Obara (2014), Step-like migration of early aftershocks following the 2007 Mw 6.7 Noto-Hanto earthquake, Japan, in *Geophysical Research Letters* **41.11**, 3864–3869.
- Kato, A. *et al.* (2016), Foreshock migration preceding the 2016 Mw 7.0 Kumamoto earthquake, Japan, in *Geophysical Research Letters* **43.17**, 8945–8953.

- Kaven, J. O. *et al.* (2015), Surface monitoring of microseismicity at the Decatur, Illinois, CO<sub>2</sub> sequestration demonstration site, in *Seismological Research Letters* **86.4**, 1096–1101.
- Keranen, K. M. *et al.* (2013), Potentially induced earthquakes in Oklahoma, USA: Links between wastewater injection and the 2011 Mw 5.7 earthquake sequence, in *Geology* **41.6**, 699–702.
- Keranen, K. M. *et al.* (2014), Sharp increase in central Oklahoma seismicity since 2008 induced by massive wastewater injection, in *Science* **345.6195**, 448–451.
- Kilmer, N. *et al.* (1987), Pressure sensitivity of low permeability sandstones, in *Journal of Petroleum Science and Engineering* **1.1**, 65–81.
- Kim, K.-H. *et al.* (2018), Assessing whether the 2017 M w 5.4 Pohang earthquake in South Korea was an induced event, in *Science* **360.6392**, 1007–1009.
- Kim, W.-Y. (2013), Induced seismicity associated with fluid injection into a deep well in Youngstown, Ohio, in *Journal of Geophysical Research: Solid Earth* **118.7**, 3506–3518.
- Kranzz, R. *et al.* (1979), The permeability of whole and jointed Barre granite, in *International Journal of Rock Mechanics and Mining Sciences & Geomechanics Abstracts*, vol. 16, 4, Elsevier, 225–234.
- Kwiatek, G. *et al.* (2019), Controlling fluid-induced seismicity during a 6.1-km-deep geothermal stimulation in Finland, in *Science Advances* **5.5**, eaav7224.
- Lay, T. and T. C. Wallace (1995), *Modern global seismology*, Elsevier.
- Lee, T. J. *et al.* (2011), The first enhanced geothermal system project in Korea, in *Proceedings of the 9th Asian Geothermal Symposium*, 4.
- Lengliné, O. *et al.* (2017), Seismicity related to the hydraulic stimulation of GRT1, Rittershoffen, France, in *Geophysical Journal International* **208.3**, 1704–1715.
- Li, K. *et al.* (2015), Comparison of geothermal with solar and wind power generation systems, in *Renewable and Sustainable Energy Reviews* **42**, 1464–1474.
- Li, L. *et al.* (2019), A review of the current status of induced seismicity monitoring for hydraulic fracturing in unconventional tight oil and gas reservoirs, in *Fuel* **242**, 195–210.

- Li, Z. *et al.* (2021), Constraining maximum event magnitude during injection-triggered seismicity, in *Nature communications* **12.1**, 1–9.
- Llanos, E. M. *et al.* (2015), Numerical model of the Habanero geothermal reservoir, Australia, in *Geothermics* **53**, 308–319.
- Lohman, R. and J. McGuire (2007), Earthquake swarms driven by aseismic creep in the Salton Trough, California, in *Journal of Geophysical Research: Solid Earth* **112.B4**.
- Louis, C *et al.* (1977), Interaction between water flow phenomena and the mechanical behavior of soil or rock masses., in *Finite elements in geomechanics*, Gudehus G, New York: Wiley, 479–511.
- Love, A. E. H. (2013), *A treatise on the mathematical theory of elasticity*, Cambridge university press.
- Lund, J. W. and A. N. Toth (2021), Direct utilization of geothermal energy 2020 worldwide review, in *Geothermics* **90**, 101915.
- Lyons, W. (2009), *Working guide to reservoir engineering*, Gulf professional publishing.
- MacDowell, N. *et al.* (2010), An overview of CO<sub>2</sub> capture technologies, in *Energy & Environmental Science* **3.11**, 1645–1669.
- Majer, E. L. and J. E. Peterson (2007), The impact of injection on seismicity at The Geysers, California Geothermal Field, in *International Journal of Rock Mechanics and Mining Sciences* **44.8**, 1079–1090.
- Marone, C. J. *et al.* (1991), On the mechanics of earthquake afterslip, in *Journal of Geophysical Research: Solid Earth* **96.B5**, 8441–8452.
- Marone, C. (1998), Laboratory-derived friction laws and their application to seismic faulting, in *Annual Review of Earth and Planetary Sciences* **26.1**, 643–696.
- Maxwell, S. (2013), Unintentional seismicity induced by hydraulic fracturing, in *CSEG Rec* **38.8**, 40–49.
- (2014), *Microseismic imaging of hydraulic fracturing: Improved engineering of unconventional shale reservoirs*, Society of Exploration Geophysicists.
- McClure, M. W. and R. N. Horne (2011), Investigation of injection-induced seismicity using a coupled fluid flow and rate/state friction model, in *Geophysics* **76.6**, WC181–WC198.

- McGarr, A (1976), Seismic moments and volume changes, in *Journal of geophysical research* **81.8**, 1487–1494.
- McGarr, A. (2014), Maximum magnitude earthquakes induced by fluid injection: Limits on fluid injection earthquakes, in *J. Geophys. Res. Solid Earth* **119.2**, 1008–1019.
- McGarr, A and A. J. Barbour (2017), Wastewater disposal and the earthquake sequences during 2016 near Fairview, Pawnee, and Cushing, Oklahoma, in *Geophysical Research Letters* **44.18**, 9330–9336.
- Mukuhira, Y. *et al.* (2017), Pore pressure behavior at the shut-in phase and causality of large induced seismicity at Basel, Switzerland, in *J. Geophys. Res. Solid Earth* **122.1**, 411–435.
- Mukuhira, Y. *et al.* (2008), Characterization of microseismic events with larger magnitude collected at Basel, Switzerland in 2006, in *Geothermal Resources Council Annual Meeting 2008: "Geothermal-Gaining Steam"*, 74–80.
- Muskhelishvili, N. I. *et al.* (1953), *Some basic problems of the mathematical theory of elasticity*, vol. 15, Noordhoff Groningen.
- Myer, L. R. and T. M. Daley (2011), Elements of a best practices approach to induced seismicity in geologic storage, in *Energy Procedia* **4**, 3707–3713.
- Neuzil, C. E. (1986), Groundwater flow in low-permeability environments, in *water resources research* **22.8**, 1163–1195.
- Nicholson, C. *et al.* (1988), The northeastern Ohio earthquake of 31 January 1986: Was it induced?, in *Bulletin of the Seismological Society of America* **78.1**, 188–217.
- Ojala, I and L Grande (2022), Pore Volume Compressibility in an Unconventional Reservoir Rock, in *83rd EAGE Annual Conference & Exhibition*, vol. 2022, 1, EAGE Publications BV, 1–5.
- Palmer, A. C. and J. R. Rice (1973), The growth of slip surfaces in the progressive failure of over-consolidated clay, in *Proceedings of the Royal Society of London. A. Mathematical and Physical Sciences* **332.1591**, 527–548.
- Pan, S.-Y. *et al.* (2019), Establishment of enhanced geothermal energy utilization plans: Barriers and strategies, in *Renewable energy* **132**, 19–32.
- Passelègue, F. X. *et al.* (2018), Fault reactivation by fluid injection: controls from stress state and injection rate, in *Geophysical Research Letters* **45.23**, 12–837.

- Passelègue, F. X. *et al.* (2020), Initial effective stress controls the nature of earthquakes, in *Nature communications* **11.1**, 1–8.
- Pearson, C. (1981), The relationship between microseismicity and high pore pressures during hydraulic stimulation experiments in low permeability granitic rocks, in *Journal of Geophysical Research: Solid Earth* **86.B9**, 7855–7864.
- Peng, Z. and P. Zhao (2009), Migration of early aftershocks following the 2004 Parkfield earthquake, in *Nature Geoscience* **2.12**, 877–881.
- Prejean, S. *et al.* (2003), High precision earthquake locations reveal seismogenic structure beneath Mammoth Mountain, California, in *Geophysical Research Letters* **30.24**.
- Rao, S. S. (2017), *The finite element method in engineering*, Butterworth-heinemann.
- Reid, H. F. (1910), The mechanics of the earthquake, in *The California Earthquake of April 18, 1906, Report of the State Earthquake Investigation Commission*.
- Rice, J. R. (1992), Fault stress states, pore pressure distributions, and the weakness of the San Andreas fault, in *International geophysics*, vol. 51, Elsevier, 475–503.
- Rice, J. R. *et al.* (1968), Mathematical analysis in the mechanics of fracture, in *Fracture: an advanced treatise* **2**, 191–311.
- Riffault, J. *et al.* (2018), Microseismicity cloud can be substantially larger than the associated stimulated fracture volume: the case of the Paralana Enhanced Geothermal System, in *Journal of Geophysical Research: Solid Earth* **123.8**, 6845–6870.
- Rinaldi, A. P. *et al.* (2014), Geomechanical effects on CO<sub>2</sub> leakage through fault zones during large-scale underground injection, in *International Journal of Greenhouse Gas Control* **20**, 117–131.
- Rohde, R. A. and Z. Hausfather (2020), The Berkeley Earth land/ocean temperature record, in *Earth System Science Data* **12.4**, 3469–3479.
- Roland, E. and J. J. McGuire (2009), Earthquake swarms on transform faults, in *Geophysical Journal International* **178.3**, 1677–1690.
- Ruina, A. (1983), Slip instability and state variable friction laws, in *Journal of Geophysical Research: Solid Earth* **88.B12**, 10359–10370.
- Rutledge, J. *et al.* (2013), Extension-shear microseismic mechanisms during hydraulic fracturing, in *2013 SEG Annual Meeting*, OnePetro.

- Rutledge, J. T. *et al.* (2004), Faulting induced by forced fluid injection and fluid flow forced by faulting: An interpretation of hydraulic-fracture microseismicity, Carthage Cotton Valley gas field, Texas, in *Bulletin of the Seismological Society of America* **94.5**, 1817–1830.
- Rutqvist, J. and O. Stephansson (2003), The role of hydromechanical coupling in fractured rock engineering, in *Hydrogeology Journal* **11.1**, 7–40.
- Rutter, E. H. and J. Mecklenburgh (2018), Influence of normal and shear stress on the hydraulic transmissivity of thin cracks in a tight quartz sandstone, a granite, and a shale, in *Journal of Geophysical Research: Solid Earth* **123.2**, 1262–1285.
- Sáez, A. *et al.* (2022), Three-dimensional fluid-driven stable frictional ruptures, in *Journal of the Mechanics and Physics of Solids* **160**, 104754.
- Schellschmidt, R. *et al.* (2010), Geothermal energy use in Germany, in *Proceedings World geothermal congress*, vol. 152, 19.
- Schmittbuhl, J. *et al.* (2021), Induced and triggered seismicity below the city of Strasbourg, France from November 2019 to January 2021, in *Comptes Rendus. Géoscience* **353.S1**, 561–584.
- Scholz, C. (1988), The critical slip distance for seismic faulting, in *Nature* **336.6201**, 761–763.
- Scholz, C. H. (2019), *The mechanics of earthquakes and faulting*, Cambridge university press.
- Schultz, R. *et al.* (2017), A seismological overview of the induced earthquakes in the Duvernay play near Fox Creek, Alberta, in *Journal of Geophysical Research: Solid Earth* **122.1**, 492–505.
- Scuderi, M. and C. Collettini (2016), The role of fluid pressure in induced vs. triggered seismicity: Insights from rock deformation experiments on carbonates, in *Scientific reports* **6.1**, 1–9.
- Scuderi, M. *et al.* (2017), Frictional stability and earthquake triggering during fluid pressure stimulation of an experimental fault, in *Earth and Planetary Science Letters* **477**, 84–96.
- Seeber, L. *et al.* (2004), A fluid-injection-triggered earthquake sequence in Ashtabula, Ohio: Implications for seismogenesis in stable continental regions, in *Bulletin of the Seismological Society of America* **94.1**, 76–87.

- Segall, P. (1989), Earthquakes triggered by fluid extraction, in *Geology* **17**.10, 942–946.
- Shapiro, S. and C. Dinske (2009), Scaling of seismicity induced by nonlinear fluid-rock interaction, in *Journal of Geophysical Research: Solid Earth* **114**.B9.
- Shapiro, S. A. (2008), *Microseismicity—a tool for reservoir characterization*, European Association of Geoscientists & Engineers (EAGE).
- (2015), *Fluid-induced seismicity*, Cambridge University Press.
- Shapiro, S. A. *et al.* (2006a), Fluid induced seismicity guided by a continental fault: Injection experiment of 2004/2005 at the German Deep Drilling Site (KTB), in *Geophysical Research Letters* **33**.1.
- Shapiro, S. A. *et al.* (2006b), Hydraulic-fracturing controlled dynamics of microseismic clouds, in *Geophysical Research Letters* **33**.14.
- Shapiro, S. A. *et al.* (1997), Estimating the crust permeability from fluid-injection-induced seismic emission at the KTB site, in *Geophysical Journal International* **131**.2, F15–F18.
- Souley, M *et al.* (2001), Damage-induced permeability changes in granite: a case example at the URL in Canada, in *International Journal of Rock Mechanics and Mining Sciences* **38**.2, 297–310.
- Stabile, T. *et al.* (2014), Fluid injection induced seismicity reveals a NE dipping fault in the southeastern sector of the High Agri Valley (southern Italy), in *Geophysical Research Letters* **41**.16, 5847–5854.
- Staněk, F. and L. Eisner (2017), Seismicity induced by hydraulic fracturing in shales: A bedding plane slip model, in *Journal of Geophysical Research: Solid Earth* **122**.10, 7912–7926.
- Stork, A. L. *et al.* (2015), The microseismic response at the In Salah Carbon Capture and Storage (CCS) site, in *International Journal of Greenhouse Gas Control* **32**, 159–171.
- Sun, Y. and D Goldberg (1997), Estimation of aspect-ratio changes with pressure from seismic velocities, in *Geological Society, London, Special Publications* **122**.1, 131–139.
- Svetlizky, I. and J. Fineberg (2014), Classical shear cracks drive the onset of dry frictional motion, in *Nature* **509**.7499, 205–208.

- Tadokoro, K. *et al.* (2000), Induced earthquakes accompanying the water injection experiment at the Nojima fault zone, Japan: seismicity and its migration, in *Journal of Geophysical Research: Solid Earth* **105**.B3, 6089–6104.
- Tang, C.-C. *et al.* (2014), Spatial-temporal evolution of early aftershocks following the 2010 ML 6.4 Jiashian earthquake in southern Taiwan, in *Geophysical Journal International* **199**.3, 1772–1783.
- Uenishi, K. and J. R. Rice (2003), Universal nucleation length for slip-weakening rupture instability under nonuniform fault loading, in *Journal of Geophysical Research: Solid Earth* **108**.B1.
- Valoroso, L. *et al.* (2009), Active faults and induced seismicity in the Val d'Agri area (Southern Apennines, Italy), in *Geophysical Journal International* **178**.1, 488–502.
- Verdon, J. P. *et al.* (2015), Simulation of seismic events induced by CO<sub>2</sub> injection at In Salah, Algeria, in *Earth and Planetary Science Letters* **426**, 118–129.
- Vidale, J. E. and P. M. Shearer (2006), A survey of 71 earthquake bursts across southern California: Exploring the role of pore fluid pressure fluctuations and aseismic slip as drivers, in *Journal of Geophysical Research: Solid Earth* **111**.B5.
- Viesca, R. C. (2015), Elastic stress transfer as a diffusive process due to aseismic fault slip in response to fluid injection, in *AGU Fall Meeting Abstracts*, vol. 2015, MR41E–02.
- (2021), Self-similar fault slip in response to fluid injection, in *Journal of Fluid Mechanics* **928**.
- Viesca, R. C. and D. I. Garagash (2018), Numerical methods for coupled fracture problems, in *Journal of the Mechanics and Physics of Solids* **113**, 13–34.
- Viesca, R. C. and J. R. Rice (2012), Nucleation of slip-weakening rupture instability in landslides by localized increase of pore pressure, in *Journal of Geophysical Research: Solid Earth* **117**.B3.
- Vilarrasa, V. and J. Carrera (2015), Geologic carbon storage is unlikely to trigger large earthquakes and reactivate faults through which CO<sub>2</sub> could leak, in *Proceedings of the National Academy of Sciences* **112**.19, 5938–5943.
- Vilarrasa, V. *et al.* (2019a), Field and laboratory studies of geomechanical response to the injection of CO<sub>2</sub>, in *Science of carbon storage in deep saline formations*, Elsevier, 209–236.

- Vilarrasa, V. *et al.* (2019b), Induced seismicity in geologic carbon storage, in *Solid Earth* **10.3**, 871–892.
- Wallroth, T. *et al.* (1999), Hot dry rock research experiments at Fjällbacka, Sweden, in *Geothermics* **28.4-5**, 617–625.
- Walsh, J. B. (1965), The effect of cracks on the compressibility of rock, in *Journal of geophysical research* **70.2**, 381–389.
- Wang, J.-A. and H. Park (2002), Fluid permeability of sedimentary rocks in a complete stress–strain process, in *Engineering geology* **63.3-4**, 291–300.
- Wawersik, W. and W. Brace (1971), Post-failure behavior of a granite and diabase, in *Rock mechanics* **3.2**, 61–85.
- Wawersik, W. and C. Fairhurst (1970), A study of brittle rock fracture in laboratory compression experiments, in *International Journal of Rock Mechanics and Mining Sciences & Geomechanics Abstracts*, vol. 7, 5, Elsevier, 561–575.
- Wei, S. *et al.* (2015), The 2012 Brawley swarm triggered by injection-induced aseismic slip, in *Earth and Planetary Science Letters* **422**, 115–125.
- Weingarten, M. *et al.* (2015), High-rate injection is associated with the increase in US mid-continent seismicity, in *Science* **348.6241**, 1336–1340.
- Westaway, R. and N. M. Burnside (2019), Fault “corrosion” by fluid Injection: A potential cause of the November 2017 5.5 Korean Earthquake, in *Geofluids* **2019**.
- White, J. A. and W. Foxall (2016), Assessing induced seismicity risk at CO<sub>2</sub> storage projects: Recent progress and remaining challenges, in *International Journal of Greenhouse Gas Control* **49**, 413–424.
- Wong, T.-F. *et al.* (1989), Crack aperture statistics and pore space fractal geometry of Westerly granite and Rutland quartzite: Implications for an elastic contact model of rock compressibility, in *Journal of Geophysical Research: Solid Earth* **94.B8**, 10267–10278.
- Wong, T.-f. (1982), Shear fracture energy of Westerly granite from post-failure behavior, in *Journal of Geophysical Research: Solid Earth* **87.B2**, 990–1000.
- Wynants-Morel, N. *et al.* (2020), Stress perturbation from aseismic slip drives the seismic front during fluid injection in a permeable fault, in *Journal of Geophysical Research: Solid Earth* **125.7**, e2019JB019179.

- Wyss, R. and L. Rybach (2010), Developing deep geothermal resources in Switzerland, in *Proceedings World Geothermal Congress, Bali, Indonesia*, 4.
- Xie, L. *et al.* (2020), Applications for Deep Geothermal Engineering, in *Modelling Rock Fracturing Processes*, Springer, 317–346.
- Yamasaki, A. (2003), An overview of CO<sub>2</sub> mitigation options for global warming—emphasizing CO<sub>2</sub> sequestration options, in *Journal of chemical engineering of Japan* **36.4**, 361–375.
- Yamashita, T. (1997), Mechanical effect of fluid migration on the complexity of seismicity, in *Journal of Geophysical Research: Solid Earth* **102.B8**, 17797–17806.
- Yeck, W. L. *et al.* (2016), Far-field pressurization likely caused one of the largest injection induced earthquakes by reactivating a large preexisting basement fault structure, in *Geophysical Research Letters* **43.19**, 10–198.
- Yeck, W. L. *et al.* (2017), Oklahoma experiences largest earthquake during ongoing regional wastewater injection hazard mitigation efforts, in *Geophysical Research Letters* **44.2**, 711–717.
- Yukutake, Y. *et al.* (2011), Fluid-induced swarm earthquake sequence revealed by precisely determined hypocenters and focal mechanisms in the 2009 activity at Hakone volcano, Japan, in *Journal of Geophysical Research: Solid Earth* **116.B4**.
- Zhang, S. and T. E. Tullis (1998), The effect of fault slip on permeability and permeability anisotropy in quartz gouge, in *Tectonophysics* **295.1-2**, 41–52.
- Zhu, S. *et al.* (2018), An analytical model for pore volume compressibility of reservoir rock, in *Fuel* **232**, 543–549.
- Zimmerman, R. W. (Sept. 1986), Compressibility of Two-Dimensional Cavities of Various Shapes, in *Journal of Applied Mechanics* **53.3**, 500–504.
- Zoback, M. D. (2010), *Reservoir geomechanics*, Cambridge university press.
- Zoback, M. D. and J. Byerlee (1975), Permeability and effective stress, in *AAPG Bulletin* **59.1**, 154–158.

## RÉSUMÉ

---

Les injections de fluides liées à l'exploitation de réservoirs géothermiques entraînent bien souvent la réactivation de failles, sous la forme d'un glissement lent ou asismique, déclenchant à son tour des séismes dits induits. Cette thèse est consacrée à une étude numérique du glissement asismique déclenché par injection de fluide. Un modèle FEM y est développé afin de simuler des expériences d'injection effectuées en presse triaxiale. Les simulations présentées dans ce travail permettent de quantifier l'effet du scénario d'injection, de la diffusivité de la faille, des propriétés de frottement et de l'état de contrainte initial sur la dynamique d'expansion du glissement asismique, fournissant un nouveau regard sur les lois d'échelles caractérisant la vitesse de rupture et le moment maximum libéré. L'approche présentée permet de fournir des pistes de réflexion pour améliorer l'évaluation de l'aléa lié à l'exploitation géothermique. Le modèle numérique développé est également validé sur un jeu de données expérimentales, ce qui ouvre des perspectives importantes pour approfondir l'interprétation mécanique des expériences d'injection menées en laboratoire.

## MOTS CLÉS

---

Injection de fluide, Glissement asismique, Vitesse de rupture, Moment asismique, Volume injecté, Presse tri-axiale, Frottement, État de contrainte

## ABSTRACT

---

Fluid injections performed in the framework of geothermal exploitation can reactivate slip on preexisting crustal faults, leading to aseismic slip transients in turn triggering so called triggered earthquakes. This PhD thesis is a numerical study dedicated to the physical control on fluid induced aseismic slip. A hydromechanical FEM is developed to simulate injection experiments performed in a tri-axial cell in the laboratory. The simulations presented allow to quantify the effect of the injection scenario, the hydraulic diffusivity, the fault friction and pre-stress on the dynamics of induced aseismic slip, providing new insights in the scaling laws commonly used to characterize this phenomenon, in particular the rupture speed and the maximum moment released. The approach presented here is thus of importance in the perspective of improving hazard mitigation in the context of geothermal exploitation. The model predictions are also validated on a real experimental dataset, which opens a new avenue to improve the mechanical interpretation of injection experiments in the laboratory.

## KEYWORDS

---

Fluid injection, Aseismic slip, Rupture Speed, Aseismic moment, Injected Volume, Tri-axial Cell, Friction, Stress